ABSTRACT

Title of dissertation: ASSIMILATION OF PASSIVE MICROWAVE BRIGHTNESS TEMPERATURES FOR SNOW WATER EQUIVALENT ESTIMATION USING THE NASA CATCHMENT LAND SURFACE MODEL AND MACHINE LEARNING ALGORITHMS IN NORTH AMERICA

Yuan Xue, Doctor of Philosophy, 2017

Dissertation directed by: Assistant Professor Barton A. Forman
Department of Civil and Environmental Engineering

Snow is a critical component in the global energy and hydrologic cycle. It is important to know the mass of snow because it serves as the dominant source of drinking water for more than one billion people worldwide. To accurately estimate the depth of snow and mass of water within a snow pack across regional or continental scales is a challenge, especially in the presence of dense vegetations since direct quantification of SWE is complicated by spatial and temporal variability. To overcome some of the limitations encountered by traditional SWE retrieval algorithms or radiative transfer-based snow emission models, this study explores the use of a well-trained support vector machine to merge an advanced land surface model within a variant of radiance emission (i.e., brightness temperature) assimilation experiments. In general, modest improvements in snow depth, and SWE predictability were witnessed as a result of the assimilation procedure over snow-covered terrain in North

America when compared against available snow products as well as ground-based observations. These preliminary findings are encouraging and suggest the potential for global-scale snow estimation via the proposed assimilation procedure.

ASSIMILATION OF PASSIVE MICROWAVE BRIGHTNESS TEMPERATURES FOR SNOW WATER EQUIVALENT ESTIMATION USING THE NASA CATCHMENT LAND SURFACE MODEL AND MACHINE LEARNING ALGORITHMS IN NORTH AMERICA

by

Yuan Xue

Dissertation submitted to the Faculty of the Graduate School of the
University of Maryland, College Park in partial fulfillment
of the requirements for the degree of
Doctor of Philosophy
2017

Advisory Committee:
Assistant Professor Barton A. Forman, Chair/Advisor
Professor Matthew C. Hansen, Dean's Representative
Dr. Rolf H. Reichle
Professor Richard H. McCuen
Associate Professor Kaye L. Brubaker

Foreword

Materials presented in Chapter 2, and Chapter 4 of this study have been published as peer-reviewed journal articles. Materials presented in Chapter 3, and Chapter 5 of this study are expected to be published as peer-reviewed articles in the next few months. The dissertation presented here was carried out in its entirety by Yuan Xue. Please see the list of publications below.

Xue, Y., and B. A. Forman (2015), Comparison of passive microwave brightness temperature prediction sensitivities over snow-covered land in North America using machine learning algorithms and the Advanced Microwave Scanning Radiometer, *Remote Sensing of Environment*, *170*, 153–165, doi:10.1016/j.rse.2015.09.009.

Xue, Y., and B. A. Forman (2016), Atmospheric and forest decoupling of passive microwave brightness temperature observations over snow-covered terrain in North America, *IEEE Journal of Selected Topics in Applied Earth Observations and Remote Sensing*, doi:10.1109/JSTARS.2016.2614158.

Xue, Y., and B. A. Forman (accepted, 2017), Integration of satellite-based decoupled passive microwave brightness temperatures and an ensemble-based land data assimilation framework in order to improve snow estimation in forested regions, *2017 IEEE International Geoscience and Remote Sensing Symposium.*

Xue, Y., B. A. Forman, and R. H. Reichle (in preparation, 2017), Assimilation of passive microwave brightness temperature observations into a land surface model with support vector machines for snow characterization in Alaska, *Water Resources Research.*

Acknowledgments

Before coming to the United States, I did not imagine that I would have the opportunity to earn a Ph.D. degree. Many of my friends were against my goal of going abroad to study since I had been offered several generous offers to continue studies in China. I even had self-doubt whether I could "survive" in the States. Presently, I asked myself if I were to given another chance to make the decision again by the end of my undergraduate study, would I switch to another route? My answer is: absolutely not. Therefore, I know I owe my gratitude to all of the people who have helped me and because of whom my graduate experience has been one that I will cherish forever.

First and foremost, I would like to thank my advisor, Dr. Forman, for giving me an invaluable opportunity to come to United States and work on interesting projects. He greatly values students interests and ideas and he has always encouraged me to be an independent researcher. I learned a lot from Dr. Forman, including American language (e.g., idioms, slang, and local phrases), American culture, research skills, social skills, teaching skills, coding skills, presenting skills, as well as his dedication in educating next-generation engineers and scientists. As one of Dr. Forman's advisees, I have always been motivated and passionate towards my research.

Further, I would like to express my deep gratitudes to Dr. McCuen, Dr. Brubaker, Dr. Reichle, and Dr. Hansen for agreeing to serve on my dissertation committee and for giving their valuable time to review the manuscript. Their in-

sightful comments and suggestions on the dissertation proposal has greatly motivated me to think more broadly about the project. They taught me how to think critically and how to explain ideas clearly.

Moreover, I would like to thank Dr. Yilu Feng for giving me valuable job-hunting suggestions. I would like to thank Saad B. Tarik for helping me adapt to the new life in the United States. I would like to thank Dr. Jing Tao for sharing her research experiences with me. I would like to thank Jing Wang, Lu Liu, Elizabeth Megan Ryan, Gaohong Yin, Jawairia Ahmad, Jongmin Park, and Dr. Yonghwan Kwon for reviewing my written materials and giving me suggestions on each presentation day. I would also like to thank all of my friends in the 0147 office for cheerful discussions during their spare time.

Last but not least, I owe my thanks to my family - my mother and father who have always stood by me and cared for me even when we are thousands of miles from each other. I owe my thanks to my husband, Dr. Feng Shi, for supporting all of the decisions that I made and tolerating my bad personality quirks.

Earning a doctoral degree is not (and should never be) the end of my dream-pursing journey; instead, it is more like a bonus trophy. The education of life is like a marathon, and I recognize that completing my Ph.D. is a relatively small part of my career. In order to achieve my ultimate career goal, I believe that I will need to build on the learning experiences of my education.

More to learn and more to follow soon ...

Table of Contents

List of Tables

List of Figures

List of Abbreviations

AMSR-E	Advanced Microwave Scanning Radiometer - Earth Observing System
ANN	Artificial Neural Network
BNU	Beijing Normal University
Catchment	NASA Catchment land surface model
DA	Data assimilation
EASE-Grid	Equal Area Scalable Earth Grid
EC	Environment Canada
EnKF	Ensemble Kalman filter
ESA	European Space Agency
GEOS-5	The Goddard Earth Observing System Model, Version 5
GES DISC	Goddard Earth Sciences Data and Information Services Center
GRACE	Gravity recovery and climate experiment
GSOD	Global Summary of the Day
IPY	International Polar Year
LAI	Leaf area index
MERRA	Modern-Era Retrospective analysis for Research and Applications
ML	Machine learning
MODIS	Moderate Resolution Imaging Spectroradiometer
MSE	Mean squared error
NASA	The National Aeronautics and Space Administration
NIC	Normalized information contribution
NRCS	Natural Resources Conservation Service
NSE	Nash-Sutcliffe model efficiency coefficient
NSC	Normalized Sensitivity Coefficient
NOAA	National Oceanic and Atmospheric Administration
OL	Open loop
PMW	Passive mcirowave
RMSE	root mean squared error
RTM	Radiative transfer model
SCA	Snow-covered area
SCF	Snow-covered fraction
SLWC	Snow liquid water content
SMMR	Scanning Sensor Microwave Radiometer
SNOTEL	SNOwpack TELemetry
SSMI	Special Sensor Microwave Imager
SV	Stem volume
SVM	Support Vector Machine
SWE	Snow water equivalent
Tb	Brightness temperature
TGI	Temperature gradient index
TPW	Total precipitable water
TWS	Terrestrial water storage
ubRMSE	unbiased root mean squared error

Chapter 1: Introduction

1.1 Importance and challenge of snowpack characterization

Snow is a critical component in the global energy and hydrologic cycle due to its control of mass and energy exchanges at the land surface [1–3]. For example, melt water released from snow (and ice) contributes more than 70% of the total annual freshwater supply in the western U.S [4]. On a global scale, freshwater from snow and ice serves as the dominant drinking water resource for more than one billion people [5]. Therefore, quantifying the amount of water within the snowpack across regional scales is important in order to better manage and regulate this source of freshwater.

The mass of snow, also known as the snow water equivalent (SWE), represents the depth of water that would theoretically result in the instance a snowpack melted. Direct quantification (i.e., in-situ measurements) of SWE is significantly complicated by spatial and temporal variability in snow processes. Compared with point-scale SWE (or snow depth) measurements that are often sparse in space or time, SWE estimates derived from land surface models are more preferred due to their complete coverage in space and time. However, model output are inherently uncertain due to model structure errors, model parameterization errors, model forcing errors,

and initial condition errors [6–8]. As an alternative, space-borne instrumentations provide an alternative capability to help fill observational gaps between ground-based sensors to better estimate SWE at the global scale based on the relationship between the measured electromagnetic response and the physical characteristics of SWE. Unfortunately, the highly nonlinear nature of the relationship is non-trivial to establish and numerous limitations exist that restrict the extensive application of space-borne products.

1.2 Methodology review of snowpack characterization

There are typically four ways to estimate SWE from space-borne sensors. One method is to merge relatively coarse, space-borne observations with in-situ measurements of finer resolution via spatial interpolation [9]. However, this method is adversely impacted by sparse spatial coverage of in-situ observations, particularly in regions near the Arctic Circle [10], coupled with strong sub-grid scale snow variability in complex terrain [11]. The second technique — space-borne PMW SWE retrieval – transforms (or retrieves) model states variables from the measured brightness temperature (Tb, defined as the physical temperature of an object times its emissivity) at specific frequencies by calibrating regression coefficients within the algorithm [12–16]. These satellite-based SWE products are often affected by errors arising from meteorological fields (e.g., data aggregation, disaggregation, extrapolation and interpolation [17]) used to force land surface models. They are also affected by significant uncertainties associated with snow stratigraphy [18], snow

grain size [19], depth hoar layer [20–23], ice crusts [24], lake fraction effects [25], and snow morphology [14], especially in densely-vegetated regions [18,26] with relatively deep snow [27]. The third method is to employ a machine learning (ML) technique to estimate SWE, which has been conducted in a few studies [9,28–30]. These studies focused on directly training an artificial neural network (ANN) using in-situ SWE observations. However, reasonable performance was restricted to in-situ observation locations with less applicability to regions between these locations [30].

In an effort to overcome many of the limitations highlighted above, the fourth alternative involves merging measurements of remote sensing observations with estimates from physically-based models using data assimilation (DA). The goal of DA (with particular relevance to SWE discussed here) is to yield a merged estimate that is superior to either the observations or the model alone [31,32]. In order to obtain an improved state of SWE or snow depth estimation capability, there is a variety of observations and retrieval products could be assimilated. Two most widely-used observations for use in the DA framework based on previous studies are (1) SWE or snow depth, and (2) snow-covered area (SCA) or snow cover fraction (SCF). It is worth noting that only real data assimilation related studies were summarized below (i.e., synthetic studies were not included), and the "direct-insertion" approach is not included as a typical DA method in the context since it does not take observation uncertainty into account.

Previous studies explored the possibility of assimilating point-scale, in-situ SWE measurements in the DA [33–35], which have shown to achieve encouraging improvements in SWE estimation. Point-scale SWE assimilation typically requires

an optimal interpolation framework prior to conducting DA in order to achieve a spatially continuous observation background. As a result, relatively good results are achieved in regions with a sufficiently-dense network of stations such as in Colorado. In places with sparse ground-based observation networks [36], this point-scale assimilation approach remains questionable since it is relatively difficult to accurately interpolate the sparse observation across large regions of space.

In order to overcome the spatial sparsity in ground-based observations, satellite-based SWE or snow depth retrieval products derived from PMW Tb observations provide an alternative route towards merging a model with spatially-distributed observations. Relatively good snow depth estimates were achieved from bias-adjusted Advanced Microwave Scanning Radiometer - Earth Observing System (AMSR-E) based snow depth observation assimilation in Alaska [37] and Colorado [38]. In addition, Kumar et al. 2015 [39] found the SCA-constrained, AMSR-E based snow depth observation assimilation is more effective (relative to the non-SCA constrained approach [40]) at capturing snow depth variations, and subsequently translating snow depth estimation improvements into streamflow forecasting. However, only marginal improvements (sometimes degraded results) for regional SWE estimates were achieved when assimilating satellite-based SWE observations obtained from either Scanning Multichannel Microwave Radiometer (SMMR) [6] or AMSR-E [41,42]. In general, the relatively unsatisfactory performance of the DA system along with the satellite-derived products might be attributed to the negative bias in the retrieval product [42].

Besides SWE retrieval products, satellite-based SCF or SCA products derived

from measured spectral reflectance of the snow cover were often used in the snow assimilation study. A snow depletion curve is often used in this approach to relate SCF/SCA with SWE or relate SCF/SCA with snow depth. For example, Andreadis et al. 2006 [41] achieved slight improvements in DA-derived SWE estimation during snow melt season over snow-covered regions with lower to middle elevations. Followed by that, Su et al. 2008 [43] used a snow density based depletion curve and found reasonably good results achieved after assimilating SCF over the North America domain when compared against AMSR-E derived SWE measurements. Using a different snow-depletion curve with a semi-empirical, and time-invariant SWE threshold parameter, De Lannoy et al. 2012 [42] showed that SCF assimilation improves the timing of the onset of the snow season but without a significant improvement of SWE amounts. The marginal improvement in SWE via SCF assimilation is most likely due to the fact that the assimilation of the SCF observations could not add more information into the model when SCF = 1 (i.e., full snow cover). Furthermore, Durand et al. 2008 and Girotto et al. 2014 [44,45] achieved encouraging improvements by assimilating typical and hybrid satellite-based SCA products based on an innovative SWE reconstruction approach applied over mountainous terrain during the snow ablation season. Margulis et al. 2016 [46] recently developed a continuous SWE reanalysis product from 1985 to 2015 by assimilating remotely sensed SCA products in Sierra Nevada, which has shown to achieve significant improvements in peak SWE estimation when compared against ground-based SWE measurements. In terms of snow depth estimation, studies conducted by [47, 48] showed that the assimilation of satellite-based SCF product is relatively effective

for snow depth estimation during snow accumulation season. In general, the assimilation of satellite-based SCF/SCA products is often affected by cloudy conditions and the uncertainty associated with the estimation of SWE or snow depth via the snow depletion curve given the fractional snow cover or the binary snow map [42].

Apart from the aforementioned two observation types (i.e., SWE and SCF) that have been widely used in the DA towards SWE estimation, there were other attempts of assimilating either different types of observations or multiple sets of observations simultaneously. For example, Magnusson et al. 2014 [36] investigated the employment of the flux (i.e., snowfall and melt rates) assimilation, and Forman et al. 2012 [49] investigated the employment of assimilating the terrestrial water storage (TWS) information obtained from gravity recovery and climate experiment (GRACE) via inter-satellite range-rate measurements. DA-derived SWE estimates reported from these two studies showed modest improvements when compared against the state-of-the-art reanalysis products. In addition, De Lannoy et al. 2012 [42] investigated the use of joint assimilation of MODIS-based SCF and AMSR-E based SWE observations, which has shown some promise to estimate snow water storage within a relatively shallow snow pack. Zhang et al. 2016 [50] investigated the use of joint assimilation of SCF and GRACE-derived TWS information, however, no significant improvements were achieved via the joint assimilation approach relative to the SCF-only assimilation scenario.

It is widely acknowledged that satellite-based PMW Tb observations contain snow mass information and operates during all-weather and nighttime conditions, few studies showed promise in improving snow mass estimated via PMW Tb assim-

ilation (a.k.a., radiance assimilation). In an assimilation context, the goal of direct Tb observations (rather than SWE retrievals) assimilation is preferable in this study as it avoids inconsistencies in the use of ancillary data (e.g., soil, vegetation) between the assimilation system and the pre-processed geographical retrievals [51]. Pulliainen et al. 2006 [52] first assimilated AMSR-E and Special Sensor Microwave/Imager [SSM/I] observed spectral difference (ΔTb). The ΔTb is expressed as:

$$\begin{aligned} \Delta Tb_{18-36} &= Tb_{18V} - Tb_{36V} \text{ for AMSR-E} \\ \Delta Tb_{19-37} &= Tb_{19V} - Tb_{37V} \text{ for SSM/I} \end{aligned} \tag{1.1}$$

where Tb_{18V} is the AMSR-E based Tb observations of 18.7 GHz at vertical polarization, Tb_{36V} is the AMSR-E based Tb observations of 36.5 GHz at vertical polarization, Tb_{19V} is the SSM/I based Tb observations of 19.0 GHz at vertical polarization, and Tb_{37V} is the SSM/I based Tb observations of 37.0 GHz at vertical polarization. The study showed that assimilation of either AMSR-E based or SSM/I-based Tb observations could improve snow depth and SWE estimates for northern Eurasia and Finland. Similarly encouraging results were reported in Durand et al. 2009 [53] based on the assimilation of ground-based Tb observations at 18.7 GHz and 36.5 GHz at vertical polarization over a relatively small snow-covered domain. In terms of continental-scale estimates, Kwon et al. 2016 [54] assimilated AMSR-E Tb observations at 18.7 GHz and 36.5 GHz at vertical polarization in North America from December 2002 to February 2003 and found modest improvements in snow depth in areas with tundra-snow cover and bare soil cover during comparison against available snow reanalysis products.

1.3 Motivations, goals and objectives

In all three aforementioned radiance assimilation studies, physically-based snow emission models were used as the model operator to invert PMW Tb measurements into modeled SWE space. The application of a snow emission model is often complicated by accurately characterizing snow grain size, depth hoar layer development, and internal ice locations and thicknesses [52, 53, 55–57]. More importantly, most global land surface models lack the fidelity at regional and continental scales to meet the needs of a snow emission model [58]. As an alternative to traditional snow emission models, previous studies [59–62] investigated the use of a machine learning algorithm (either ANN or a support vector machine (SVM)) as the observation operator for use within a radiance assimilation framework in order to overcome many of the deficiencies with snow emission models. It was shown that a machine learning algorithm performed well throughout the entire snow season and was able to capture much of the temporal and spatial variability in the modeled Tb, and hence, such an algorithm was recommended for eventual use as a observation operator within a proposed DA framework. The research presented here is a first-ever attempt to merge PMW Tb satellite observations with an advanced land surface model using trained machine learning algorithms within a DA framework. This exercise will help address the overarching science question: How can the predictability of SWE and snow depth at regional and continental scales be improved through the systematic integration of real PMW measurements collected by satellite-based instrumentation and a machine-learning based algorithm into a

land surface model?

1.4 Organization of the thesis

In Chapter 2, sensitivity analyses were conducted to evaluate the performance of two different ML algorithms. In Chapter 3, a radiance assimilation framework was analyzed for use in SWE and snow depth estimation, along with a well-trained ML-algorithm-based measurement model operator selected from Chapter 2. In Chapter 4, a relatively simple two-step atmospheric-and-forest decoupling procedure was developed for use in removing non-snow related signals from the observations prior to ML training procedure. In Chapter 5, the assimilation of multi-frequency, multi-polarization, satellite-based, decoupled radiance emissions derived from Chapter 4 was evaluated for use in SWE and snow depth estimation over forested regions. Chapter 6 provides a summary of the major findings, and future directions for research.

1.5 Implications

It is quoted from the 2015 Snow Experiment (SnowEx) White Paper that "The key gap in past National Aeronautics and Space Administration (NASA) and European Space Agency (ESA) snow mission proposals has been the retrieval of SWE in densely forested regions". The nature of the close-to-random spatial distribution of tree branches and the dynamics of forest cover evolution is one significant limitation in the accuracy of SWE estimation relying on satellite-based microwave

observations.

It is anticipated that regional SWE estimation could be improved within the proposed radiance assimilation module such that water resources managers can make better decisions with reliable SWE information in their water management practice and water supply forecasting activity, such as reservoir regulation, downstream flooding prediction, and agricultural water management. In addition, it is anticipated that a more accurate characterization of the SWE information could be used as an indicator of climate variability and change in order to help policy makers better understand and protect freshwater resources.

Chapter 2: Comparison of passive microwave brightness temperature prediction sensitivities over snow-covered land using machine learning algorithms

2.1 Motivation and Objective

Previous studies showed that machine learning (ML) algorithms (e.g., artificial neural network (ANN) and support vector machine (SVM)) reasonably reproduce passive microwave brightness temperature observations over snow-covered land as measured by the Advanced Microwave Scanning Radiometer (AMSR-E) and the Special Sensor Microwave Imager (SSMI) [59, 60, 62]. It was concluded that both the ANN and SVM could eventually be used as measurement operators to estimate brightness temperatures (Tb) within a data assimilation (DA) framework for the purpose of SWE estimation at regional and continental scales. However, there is still a number of fundamental questions needed to be addressed prior to integrating with DA. For example, do the ANN and SVM reproduce Tb for the right (i.e., physically-based) reasons? Further, what are the most significant input variables to the ML models? Are the accurate Tb estimates over snow-covered land associated with the snow-related variables (e.g., SWE)? If so, under which conditions (e.g.,

with or without overlying vegetation) will the ML models be sensitive to SWE? Or is the sensitivity of the ML model output due to non-snow-related state variables (e.g., soil temperature and air temperature)? Is it necessary to reduce the model input complexity by removing insensitive ones? Therefore, the goal of this chapter is to explore the ANN- and SVM-derived Tb (trained on AMSR-E Tb observations) sensitivities using a unified framework in an effort to answer the questions formulated above. Section 2.2 through Section 2.4.2 have been published in Remote Sensing of Environment, and Section 2.4.3 will be published in IEEE Xplore.

2.2 Machine learning and model formulation

Arthur Samuel (1959; [63]) first defined ML as a field of study that gives computers the ability to learn without being explicitly programmed. An alternative definition is the process of identifying a set of categories (sub-populations) where a new observation belongs on the basis of a training set of data containing observations whose category membership is known [64]. Based on properly constructed systems with proper parameterizations, ML algorithms are capable of learning about the regularities present in the training data such that constructing and generalizing rules can be extended to the unknown data during the training phase.

A plethora of ML algorithms are available to choose from depending on what type of question needs to be addressed. An ANN and a SVM framework are selected in this study (with particular relevance to SWE) because (1) they are data-driven models [65] used in cases where the underlying physical relationships between the

electromagnetic response and SWE characteristics are not fully understood and (2) they can be used to reproduce nonlinear processes via iterations without prior knowledge about the relationship between the parameters (e.g., snow grain size and SWE) [66].

Some differences between these two types of ML techniques are also evident. For example, the existence of local minima [67] could prevent an ANN from finding the unique global minimum solution to a constrained optimization problem, which is not the case for a SVM, which possesses a more simple geometric interpretation [68] characterized by convex optimization problems and thereby a unique global optima will always be found. Additionally, if the size of the training examples is not large enough, the SVM is expected to perform well based on a properly-selected mechanism of model parameters since the number of support vectors in the decision (feature) space is far less than the number of training points [69] whereas an ANN is always in need of a relatively large number of training points.

Both ANN- and SVM-based techniques in this study utilize the same model inputs derived from the National Aeronautics and Space Administration (NASA) Catchment land surface model (Catchment; [70]) and output Tbs at three different frequencies (10.65 GHz, 18.7 GHz, and 36.5 GHz) at both horizontal and vertical polarization (see Table 2.1). Uncertainty and errors in Catchment-derived model output, including SWE, were discussed in detail in [7]. SWE estimates from the Catchment model in the MERRA-Land data product were found to be unbiased in the global mean [7]. In addition, the brightness temperatures produced from the ML algorithms are also unbiased [59,60]. Therefore, it is hypothesized that the first

statistical moment related to the mode of estimated SWE in the Catchment model is reasonably characterized.

Table 2.1: Model (ANN and SVM) inputs and outputs (reproduced from [59])

Inputs	Symbol	Unit
Top layer snow density	ρ_{sn1}	kg/m^3
Middle layer snow density	ρ_{sn2}	kg/m^3
Bottom layer snow density	ρ_{sn3}	kg/m^3
Snow liquid water content	$SLWC$	kg/m^2
Snow water equivalent	SWE	m
Near-surface air temperature	T_{air}	K
Near-surface soil temperature	T_{p1}	K
Skin temperature	T_{skin}	K
Top layer snow temperature	T_{sn1}	K
Bottom layer snow temperature	T_{sn3}	K
Temperature gradient index	TGI	-
Outputs	**Symbol**	**Unit**
Brightness temperature at 10.65 GHz, H-polarization	10H	K
Brightness temperature at 10.65 GHz, V-polarization	10V	K
Brightness temperature at 18.7 GHz, H-polarization	18H	K
Brightness temperature at 18.7 GHz, V-polarization	18V	K
Brightness temperature at 36.5 GHz, H-polarization	36H	K
Brightness temperature at 36.5 GHz, V-polarization	36V	K

Each ML technique is trained with the same nine-year (2002-2011) training dataset of Tb observations from AMSR-E where forest and atmospheric effects were not removed prior to ANN or SVM training in this study. All Catchment-based inputs (i.e., the 11 model inputs listed in Table 2.1), AMSR-E training data, ANN-based output, and SVM-based output (e.g., six different Tbs listed in Table 2.1) are generated on the 25km $\times$ 25km Equal Area Scalable Earth (EASE) grid. A jack-knifing training procedure was adopted such that an independent validation of either ANN- or SVM-based model output was conducted. The results presented here

employ previously trained ANN and SVM models based on the work discussed in [59,60]. For brevity, only essential details related to both ANN and SVM frameworks are outlined in the Appendix A for reference.

2.3 Sensitivity analysis formulation

Sensitivity analysis is an important tool for assessing the relative importance of causative factors in a model. This study conducts a sensitivity analysis to investigate the response of either an ANN- or a SVM-based Tb estimate with respect to small perturbations in model inputs and whether or not such small perturbations result in a physically-consistent response. Since the ANN and SVM have the same model inputs and model outputs, the study conducted here is able to compare and contrast the sensitivity of predicted Tb between the two different ML techniques. In order to quantify the relative importance of each model input variable, the Normalized Sensitivity Coefficients (NSCs; [71]) are computed as:

$$\begin{aligned} NSC_{i,j} &= (\frac{\partial M_j}{\partial p_i}) \cdot (\frac{p_i^0}{M_j^0}) \\ &\approx (\frac{M_i^i - M_j^0}{\Delta p_i}) \cdot (\frac{p_i^0}{M_j^0}) \end{aligned} \tag{2.1}$$

where p_i^0 is the nominal input value; M_j^0 is the nominal output value; M_j^i is the perturbed output value; Δp_i is the amount of perturbation; $i = 1, 2, \cdots, n$; $j = 1, 2, \cdots, m$; n is the number of inputs; and m is the number of outputs.

The study perturbs one input at a time in order to calculate the NSC for each model input. It is worth noting that the perturbation cannot be too small, otherwise model noise will be amplified, which leads to an improper estimate of the NSC. In

addition, the perturbation cannot be too large, otherwise, the model will fall into a nonlinear region where the marginal function evaluated at the given point is no longer an accurate representation of the rate of change in the model output with respect to the change in the input as expressed in Equation 2.1.

A generally-applied perturbation size of +/-5% is used in this study. A range of perturbation sizes were tested ranging from -20% to +20% and a +/-5% perturbation size was ultimately selected because model noise amplification was minimized and the model response was, in general, linear with respect to the range of input perturbations. The model outputs for both ANN- and SVM-based models are the Tb estimates at both horizontal and vertical polarization at 10.65 GHz, 18.7 GHz and 36.5 GHz (see Table 2.1). Only 7 of the 11 model inputs are discussed below. The other 4 input variables were shown to be relatively insensitive based on numerous NSC calculations from 2002 to 2011 using the ANN- and SVM-based models, and therefore are excluded from the remainder of the sensitivity analysis. The remaining seven model inputs explored are: (1) top-layer snow density, (2) SWE, (3) near-surface air temperature, (4) near-surface soil temperature, (5) top layer snow temperature, (6) temperature gradient index (TGI), which is a snow grain size metamorphism proxy generally for cold snow pack conditions [72], and (7) skin temperature (a.k.a. radiative skin temperature of the terrestrial environment).

Vegetation is one of the biggest challenges in the accurate estimation of SWE-related Tb [18, 73]. Four different scenarios (see Table 2.2) are categorized for both ANN- and SVM-based models with various amounts of forest cover and SWE for a given day of interest in order to succinctly bound the competing effects of SWE

and forest canopy on passive microwave (PMW) Tb estimates. The snow class category for each location is obtained via the seasonal snow cover classification system derived by [74]. The forest cover (%) and forest density (g/cm^3) values are obtained from the Moderate Resolution Imaging Spectroradiometer (MODIS) [75]. The original tree cover product has a resolution of 500m $\times$ 500m. For purposes of this study, the original product was re-mapped as forest cover fraction and forest density onto the 25km EASE-Grid. Without considering the effects of changes in biotic disturbances and other climatic aspects, this study assumes that the forest cover fraction is relatively constant across the time period of investigation.

Table 2.2: Canopy cover (%) and SWE (m) for the selected locations under different scenarios of various amounts of SWE (11 Jan 2004) and forest.

Scenario	Latitude (degree)	Longitude (degree)	Forest cover (%)	Forest density (g/cm^3)	SWE (m)	Snow class
Low Veg + Low SWE	50.49	-100.39	5.04	0.059	0.03	Taiga
Low Veg + High SWE	58.35	-73.66	0	0	0.12	Tundra
High Veg + Low SWE	55.09	-112.36	81.61	0.504	0.01	Alpine
High Veg + High SWE	64.28	-146.17	95.44	0.517	0.13	Tundra

In this study, locations in the study domain with percentages of forest cover (i.e., trees with heights of at least 2 meters) greater than 50% are defined arbitrarily as "high forest" areas, and those with forest cover less than 10% are defined arbitrarily as "low forest" areas (see Figure 2.1). In addition, a SWE threshold of

0.01 m is used as the lower limit in the investigation at which the location is considered snow-covered, which is a similar threshold applied in most SWE retrieval algorithms. For the specified day of interest, locations with SWE magnitudes greater than 0.10 m (∼0.35 m snow depth) but less than 0.28 m (∼0.98 m snow depth) are categorized into the "high SWE" class since snow depths greater than 1 m usually exceeds the upper limit of PMW capabilities (Josberger and Mognard, 2002). On the other hand, locations with SWE values greater than the SWE threshold of 0.01 m (∼0.035 m snow depth) and less than 0.04 m (∼0.14 m snow depth) are defined as "low SWE" areas (see Figure 2.2). The selection of threshold values for "low" versus "high" SWE and "low" versus "high" forest cover are somewhat arbitrary. However, the goal of the exercise is to simply explore values at the extreme ends of the spectrum is order to bound the analysis.

2.4 Sensitivity analysis results

The sensitivity results of both ANN- and SVM-based Tb estimates with respect to spatiotemporal variability in forested and non-forested regions are presented in the following section.

2.4.1 Spatial variability of NSCs at single frequency

In general, representative locations selected (see Table 2.2) for this study were chosen because: (1) there is no sea ice, and (2) there is no significant lake fraction within the region (25 km × 25 km). Additionally, year 2004 is selected for display

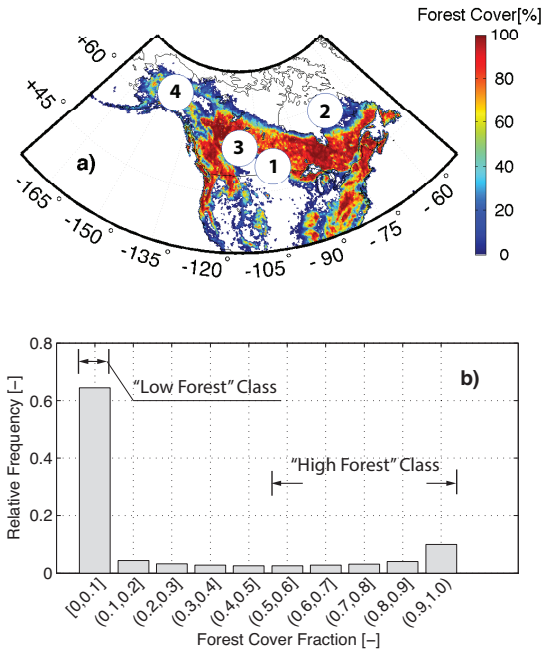

Figure 2.1: Remapped forest cover distribution from [75] is shown in a) with the relative frequency distribution of forest cover shown in b). "High forest" class is defined as greater than 50% forest fraction, whereas "low forest" class is defined as less than 10%. Marker 1 is labeled as a selected location containing low SWE and low vegetation coverage; Marker 2 is labeled as a selected location containing low SWE and high vegetation coverage; Marker 3 is labeled as a selected location containing high SWE and low vegetation coverage; and Marker 4 is labeled as a selected location containing high SWE and high vegetation coverage.

since the 2004-2005 snow season is fairly representative of conditions during the 9-year study period. Sensitivity results of vertically-polarized Tb estimates at 18.7 GHz and 36.5 GHz under four different scenarios are presented from Sections 2.4.1.1 to 2.4.1.4 in order to highlight the differences between the ANN-based and the SVM-based estimates. Further, 18V and 36V are the focus of the discussions since these channels are commonly used in SWE retrieval algorithms [14–16].

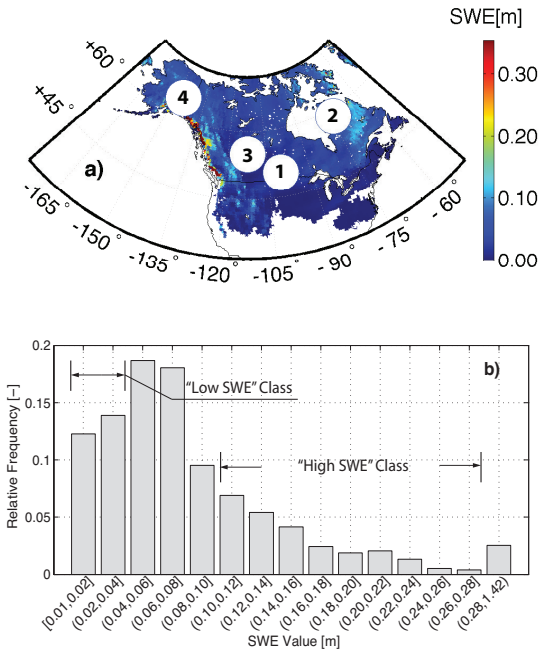

Figure 2.2: An example of a) SWE distribution obtained from the NASA Catchment model on 11 Jan 2004 and b) relative frequency of SWE distribution. "High SWE" class is defined as SWE values greater than 0.1m but less than 0.28m, whereas "low SWE" class is defined as less than 0.04m but greater than 0.01m. Marker 1 is labeled as a selected location containing low SWE and low vegetation coverage; Marker 2 is labeled as a selected location containing low SWE and high vegetation coverage; Marker 3 is labeled as a selected location containing high SWE and low vegetation coverage; and Marker 4 is labeled as a selected location containing high SWE and high vegetation coverage.

2.4.1.1 NSCs in the regions with low forest cover and low SWE

The first test location (latitude 50.49° and longitude -100.39°) for the low SWE and low forest class is in the southwest corner of Manitoba, Canada (see location in Figures 2.1a and 2.2a marked 1). Figure 2.3 displays the NSCs for seven different model inputs computed for 11 Jan 2004. Some similarities in model performance are evident in Figures 2.3a and 2.3b. For example, NSC values with respect to

soil temperature for both ML methods are negative at the displayed polarizations and frequencies, and the magnitude of the NSC with respect to soil temperature at 36V computed from the ANN-based model is roughly 5 times greater than that at 18V. This phenomenon is somewhat counterintuitive in the sense that given a slight increase in the top-layer soil temperature, it is possible that recorded Tb (at certain microwave frequencies) would also increase, which would result in a positive value of the NSC. In addition, soil emission depth decreases as the microwave frequency increases (assuming constant soil conditions) during the snow accumulation phase. That is, the microwave signal at 36.5 GHz (with an emission depth of $\sim$0.8 cm) is more strongly attenuated than that at 18.7 GHz (with an emission depth of $\sim$1.4 cm) especially in the presence of 5% vegetation cover coupled with $\sim$9.0 cm of overlying snow pack [76]. It is interesting to note that the ANN-based NSC of top-layer soil temperature at 36V is a large and negative number (see Figure 2.3b), which dominates the sensitivity of the six remaining input variables and mostly dictates the model behavior. It could be partly explained that given a slight increase in top-layer soil temperature during the sensitivity analysis, the emissivity of frozen soil decreases [77], which may lead to a sharp decrease in the Tb observations. This behavior might be more evident near the snow-soil transitional surface, rather than deep soil zones given the relatively short soil emission depth.

The ANN-based model is less sensitive to several snow-related states, such as SWE, top layer snow density, TGI, and top layer snow temperature in the presence of a shallow snow pack. However, the Tb estimates at both 18V and 36V based on the SVM model are more sensitive (relative to the ANN) to perturbations in the

snow states. Alternatively, the variation in the ANN-based Tb estimates is more affected by perturbations in the air temperature and soil temperature compared to the SVM-based model. In such a case, the SVM-based model likely possesses more potential at capturing and reproducing snow-related features of PMW emission over snow-covered land.

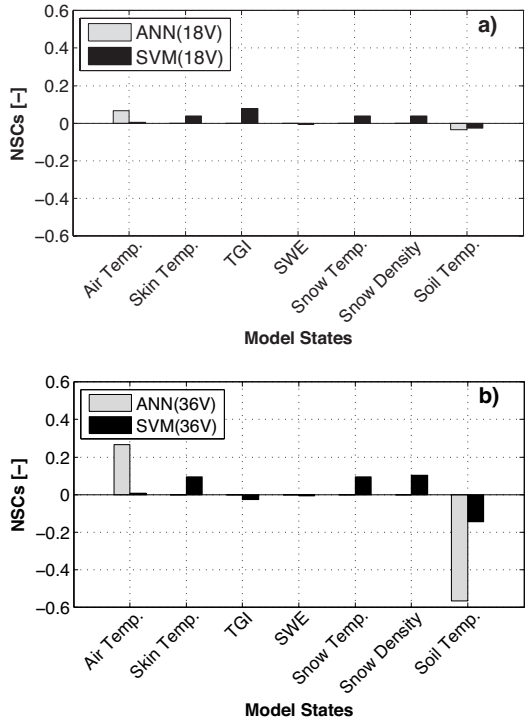

Figure 2.3: ANN and SVM-based NSCs for seven model states at a location with low forest cover and low SWE on 11 Jan 2004 for vertically polarized Tb estimates at a) 18.7 GHz and b) 36.5 GHz.

2.4.1.2 NSCs in the regions with low forest cover and high SWE

The representative location (latitude 58.35° and longitude -73.66°) of the high SWE and low forest class is in the northern part of Quebec, Canada (see location in

Figures 2.1a and 2.2a, marked 2). Since this area is not covered by forest, both ANN- and SVM-based NSCs are similar in their respective sensitivity to skin temperature and top layer snow temperature as witnessed in Figure 2.4. This can be explained by the fact that skin temperature is a parameter to quantify the temperature of the terrestrial surface closest to the satellite-based sensor (i.e., AMSR-E). In this area with little forest cover, the skin temperature approximately equals the top-layer snow temperature, and hence, the model responses of Tb with respect to changes in skin temperature (or snow temperature) are effectively identical.

Some differences in model performance were also evident. The ANN-based model is only sensitive to the top-layer soil temperature and exhibits limited sensitivity to several snow-related states, such as SWE, top layer snow density, snow temperature and TGI. Conversely, SWE, TGI, snow density and snow temperature are relatively sensitive parameters in the SVM-based Tb estimates. The magnitude of NSC for SWE at 36V (shorter wavelength) is larger than that at 18V (longer wavelength). One possible explanation for this behavior is 36.5 GHz (relative to 18.7 GHz) is more sensitive to snow pack scattering, which is indirectly associated with volumetric storage of snow water (i.e., SWE or snow depth) while the 18.7 GHz data is less affected by snow scattering processes [78, 79]. The negative signs of the NSC of SWE based on the SVM model at both 18V and 36V further reproduce the theory that increasing SWE introduces an increased possibility of snow pack scattering, and hence, a reduction in Tb.

It is interesting to note that the scenario with low forest cover and high SWE possesses the highest NSC in terms of magnitude for SWE (of all four locations

examined here) when using the SVM at both 18V and 36V, respectively (see Figures 2.4a and 2.4b). This is notable because this scenario most closely agrees with the fundamental scattering theory that underpins most SWE retrieval algorithms. In addition, forest effects in this example are relatively insignificant (or nonexistent) as the emitted radiation from the underlying snow pack will not be strongly attenuated by the relatively sparse overlying forest cover nor does the forest canopy significantly add to the Tb as measured by the radiometer. It is also worth noting that SWE is computed as the product of snow depth and snow density. Given a slight increase in snow density (while holding snow depth constant during the sensitivity analysis), SWE is expected to increase, which will trigger a decrease in Tb as discussed above. Hence, this could possibly be used to explain the physical rationale behind the negative sign of the NSC of snow density based on the SVM model at both 18V and 36V. In summary, compared with the ANN-based model at this study location, the SVM-based Tb estimate has the potential to capture more SWE information (as well as other snow-related variables) at both 18V and 36V based on the computed NSCs.

It is further discovered that SVM sensitivity to SWE could be enhanced via model reductions such that relatively insensitive input variables (e.g., air temperature) are selectively removed from the SVM formulation. That is, as more and more variables, other than SWE, are eliminated, the SVM-based Tb estimates become increasingly reliant on (or sensitive to) SWE information (see Section 2.4.3).

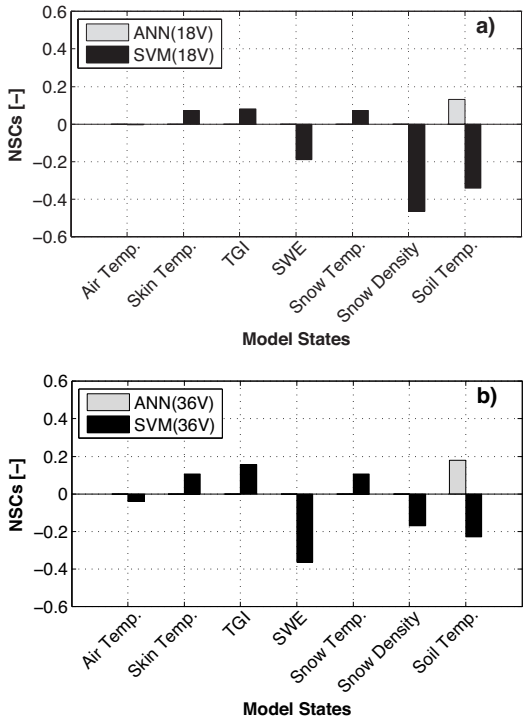

Figure 2.4: ANN and SVM-based NSCs for seven model states at a location with low forest cover and high SWE on 11 Jan 2004 for vertically polarized Tb estimates at a) 18.7 GHz and b) 36.5 GHz.

2.4.1.3 NSCs in the regions with high forest cover and low SWE

This study location (latitude 55.09° and longitude -112.36°) of the low SWE and high forest class is in the middle of Alberta, Canada (see location in Figures 2.1a and 2.2a, marked 3). The forest cover fraction is 82% and the model-derived SWE is 0.01 m on 11 Jan 2004 (see Table 2.2). The ANN-based Tb estimates are relatively insensitive to snow-related states (see Figures 2.5a and 2.5b) except for the top-layer snow temperature, which yields an NSC value of 0.13 at 18V and 0.08 at 36V. It is more likely that the accurate Tb estimates derived from the ANN-based model at

this location (and others) does not depend on the model input of SWE. That is, the ANN-based estimation of Tb derives more information associated with the near-surface soil temperature (Figures 2.3, 2.4, 2.5 and 2.6), air temperature (Figures 2.3 and 2.5), and skin temperature (Figure 2.5 and 2.6) rather than from the snow pack information. On the other hand, even during conditions with high forest cover and limited snow depth, the SVM-based model remains sensitive to snow-related variables. That is, TGI, SWE, snow temperature, and snow density are consistently the four most sensitive input variables during the SVM-based sensitivity analysis at both 18V and 36V. The SVM-derived NSC with respect to SWE is negative at 36V, which agrees well with the scattering theory discussed previously. Conversely, the SVM-derived NSC with respect to SWE is positive at 18V. This sign-change behavior in the NSC for SWE between different microwave frequencies might be explained by the fact that shallow snow (0.01 m of SWE in this particular location) is effectively transparent to microwave radiation [80] especially at 18V that possesses a higher emission depth. On the other hand, since the area is covered with 82% of forests, the recorded microwave emission is likely to contain a measurable amount of signal from dense forest contributions, which could explain the positive NSC with respect to SWE as witnessed at 18V in Figure 2.5.

It is difficult to discern exactly why the near-surface air temperature, skin temperature and the top-layer snow temperature have equal sensitivity in predicting vertically-polarized Tb at both 18.7 GHz and 36.5 GHz in the ANN-based model. In the absence of vegetation, the skin temperature is expected to possess the same sensitivity as the top-layer snow temperature because in the snow-covered land without

vegetation, the skin temperature and the upper-layer snow temperature are essentially identical. However, this particular location is largely covered by forest, hence, the skin temperature and snow temperature often differ significantly from one another. The disagreement with the fundamental physics may come from: (1) model forcing error (e.g., precipitation rate), (2) measurement error associated with the MODIS forest cover product, or (3) learning inability of the ANN in regions with high forest cover and relatively little snow in the sense that it predicts the right answer for the wrong reasons. This learning inability may arise from the ANNs learning algorithm in terms of converging to the local minima [67] instead of the global minimum value of its objective function of mean squared errors.

2.4.1.4 NSCs in the regions with high forest cover and high SWE

The representative location (latitude 64.28° and longitude -146.17°) of the high SWE and high forest class is in the middle of Alaska, U.S. (see location in Figures 2.1a and 2.2a, marked 4). Since this area is covered by thick forest, ANN- and SVM-based NSCs are different in terms of the sensitivity to skin temperature and top layer snow temperature as witnessed in Figure 2.6. The results shown in Figures 2.6a and 2.6b also demonstrate that SWE is a relatively sensitive model parameter in the SVM-based Tb estimates at 36V, which may suggest some potential in future work for enhancing SWE estimation in densely-forested regions via Tb assimilation. Conversely, snow-related variables (e.g., TGI, SWE and snow density) are relatively insensitive parameters in the ANN-based Tb estimates at both 18V and 36V.

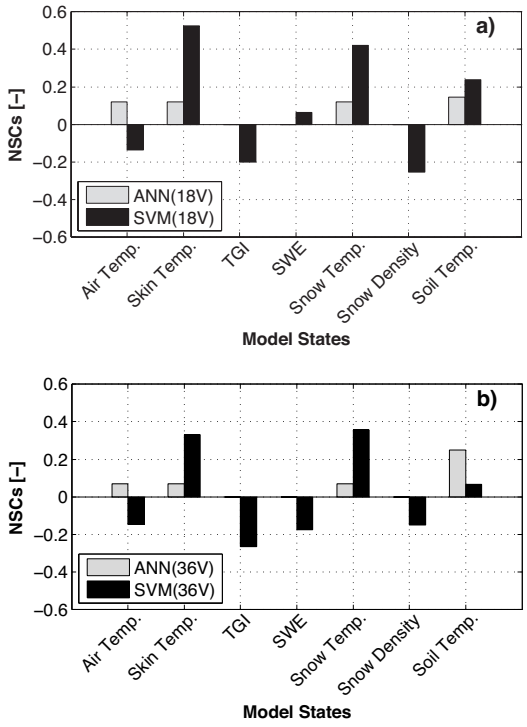

Figure 2.5: ANN and SVM-based NSCs for seven model states at a location with high forest cover and low SWE on 11 Jan 2004 for vertically polarized Tb estimates at a) 18.7 GHz and b) 36.5 GHz.

It is interesting to note that the NSCs of air temperature computed in Sections 2.4.1.3 and 2.4.1.4 during the SVM-based sensitivity analysis are both negative, which is somewhat counterintuitive to basic theory. It may be due to the presence of atmospheric water vapor, or surface wind effects, both of which could lead to a decrease in measured Tb. Additionally, the sign-change behavior of the NSC with respect to air temperature might also be explained by the fact that an increase in the air temperature would possibly introduce ice crusts formation (or snow consolidation), which may lead to a lower Tb at both 18V and 36V [24, 79].

Since SWE is the primary motivation for this study, NSC relative frequency

plots of SWE for a single day help further demonstrate the sensitivity differences to SWE between the ANN- and the SVM-based Tb estimates. The results in Figure 2.7 highlight the differences between the two methods by comparing the relative frequency of NSC values on 11 Jan 2004 across the entire North America (NA) domain. The relative frequency is computed as the ratio of the number of binned occurrences to the total number of computed NSCs. The overall pattern of the histogram suggests that compared with SVM-based NSC of SWE values, Tb estimates derived from the ANN model are much less sensitive to the input of SWE with more than 80% of the NSC values close to zero. The SVM, on the other hand, suggests greater sensitivity to SWE across much more of the NA domain during most of the snow season (similar results were found on other examined dates).

2.4.1.5 Sensitivity to spectral difference

All of the discussions above regard the relative change in the estimation of a single vertically (or horizontally) polarized Tb frequency, either at 10.65 GHz, 18.7 GHz or at 36.5 GHz, with respect to the relative change in SWE (or other model states). Recall that in most snow retrieval products, SWE (or snow depth) is proportional to the spectral difference between particular PMW frequencies depending on sensor characteristics. For example, Chang et al. (1987) [12] presented the first snow depth-Tb relationship for a uniform snowfield with a fixed snow density of 300 kg/m^3 and a mean radius of 0.3 mm, which was expressed as a function of the spectral difference of Tb between 18H and 37H. After that, Chang et al. (1996) [15]

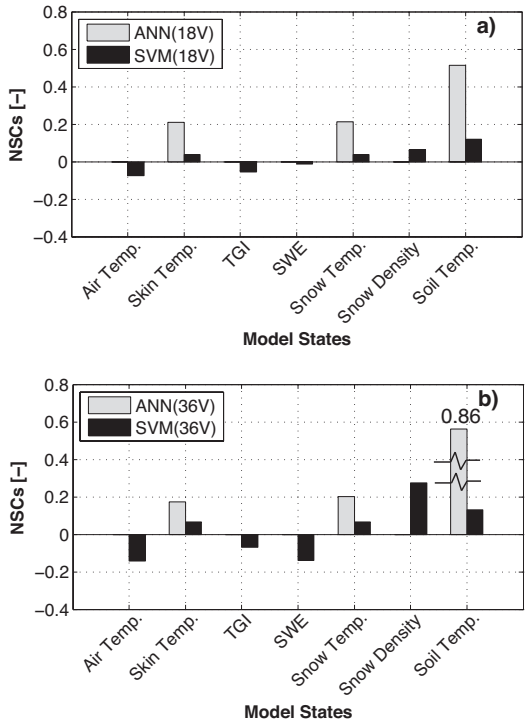

Figure 2.6: ANN and SVM-based NSCs for seven model states at a location with high forest cover and high SWE on 11 Jan 2004 for vertically polarized Tb estimates at a) 18.7 GHz and b) 36.5 GHz. The ANN-derived NSC for top-layer soil temperature at 36V is equal to 0.86 and was truncated in order to enhance visual clarity.

improved SWE estimation in forested regions with a revised form of the algorithm using the spectral difference of Tb between 19V and 37V. The general theory postulates that an increase in SWE causes an increase in scattering and more so at shorter wavelengths. Therefore, the spectral difference (e.g., ΔTb = Tb_{18V}- Tb_{36V}) should increase as SWE increases due to the enhanced scattering effects on the emitted microwave radiation. In order to examine the predictive skill of spectral differences via different ML algorithms, the NSC of SWE to the spectral difference of Tb was

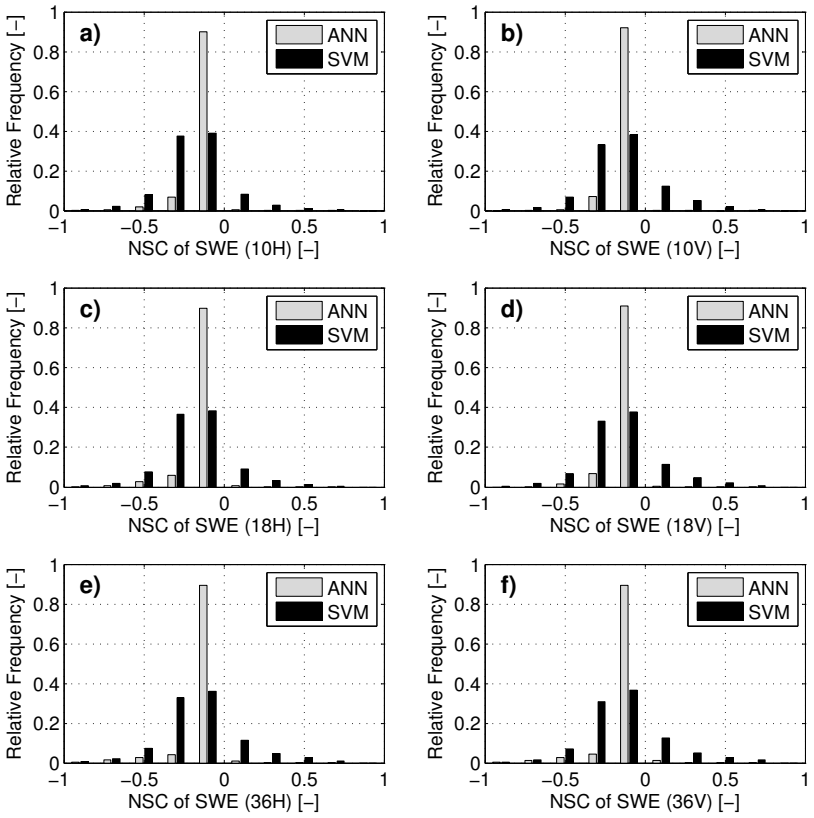

Figure 2.7: Relative frequency of NSCs for SWE derived from both ANN- and SVM-based Tb estimates. Subplots show a) 10H, b) 10V, c) 18H, d) 18V, e) 36H, and f) 36V.

investigated as:

$$NSC_{(SWE,\Delta Tb)} = \{\frac{\Delta\Delta(Tb_{f1} - Tb_{f2})}{\Delta SWE}\} \cdot \{\frac{SWE^0}{\Delta(Tb^0_{f1} - Tb^0_{f2})}\} \tag{2.2}$$

where $NSC_{(SWE,\Delta Tb)}$ (dimensionless) is the normalized rate of change in the spectral difference of Tb (ΔTb) with respect to changes in SWE; $\Delta\Delta(Tb_{f1} - Tb_{f2})$ (K) is the difference of the spectral difference of ML-derived Tb estimates model inputs between PMW frequencies of f1 and f2 (f1 $<$ f2); ΔSWE (m) is the change in SWE magnitude; SWE^0 (m) is the nominal value of SWE before introducing a perturbation; and $\Delta(Tb^0_{f1} - Tb^0_{f2})$ (K) is the spectral difference of the nominal value

(before perturbation) of ML-derived Tb estimates between PMW frequencies of f1 and f2.

A perturbation size of +/-5% is used here, during which the model response of spectral difference of Tb, in general, falls into the linear region for the model inputs across NA. For brevity, only the results of the NSC distributions for SWE of spectral difference between Tb at 18V and 36V are shown in Figure 2.8. Both ANN- and SVM-based models are sensitive to SWE to some extent at some locations on 11 Jan 2004 during the snow accumulation phase. However, as discussed from Sections 2.4.1.1 to 2.4.1.4, SWE plays a more dominant role in most of the regions in the NA domain for the SVM-based Tb estimate (relative to the ANN-based Tb estimate). Therefore, the strong response between the model input of SWE and the ML-derived spectral difference of Tb estimate suggests that the SVM may be more appropriate for use as a model operator within a DA framework in order to enhance SWE estimation at regional or continental scales.

The positive sign of the SVM-based NSC of SWE at a spectral difference between 18V and 36V agrees well with most snow retrieval algorithms. However, more than 40% of the spectral difference NSCs of SWE across the entire NA domain have negative values, which occurred more frequently in regions north of the boreal forest compared with other areas in the domain. These negative NSC values may be largely due to the highly non-linear response [81, 82] of the snow pack contrary to the (quasi-) linear spectral difference reflected in many SWE retrieval algorithms (e.g., [12, 14]). In addition, most of the current SWE retrieval algorithms are based on specific assumptions that the snow pack contains a fixed density or a fixed snow

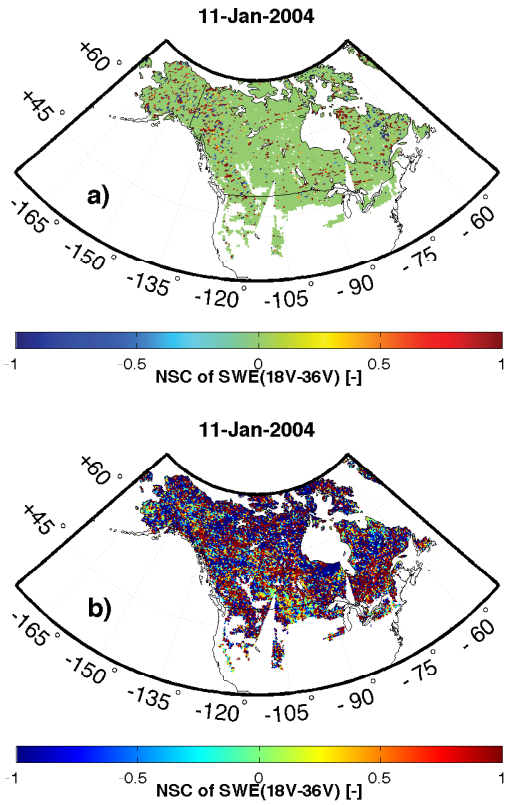

Figure 2.8: An example of NSC maps on 11 Jan 2004 with respect to SWE for a) ANN-based and b) SVM-based estimates of spectral difference between Tb at 18V and 36V.

grain size, which is often not the case [74]. Another possible explanation for the sign-change in the spectral difference NSCs may be due to the formation of wind-slab coupled with the existence of internal ice crusts and depth-hoar layers. In addition, sensitivity analysis were performed for the SVM model with four input states (see Section 2.4.3), similar NSCs distribution pattern were witnessed with 35% of the spectral difference NSCs of SWE across the entire NA domain have negative values. Suffice it to say that the exact reasons for the sign-change in the spectral difference NSCs in portions of the study domain are not entirely understood. However, it is

clear that the SVM-based spectral difference estimates are much more sensitive to SWE than are the ANN-based estimates and that the SVM-based estimates suggest a non-linear relationship to SWE that is routinely found in PMW-based snow remote sensing studies [26].

2.4.2 Temporal behavior of NSCs

In order to better examine the model behavior, additional locations (beyond what was examined previously) of low forest and high forest cases in the year 2004 were selected for investigation of temporal variability in the NSCs. It is worth noting that SWE is selected here for investigation since SWE estimation is the main motivation for this study.

A representative location of the low forest class (latitude 54.65° and longitude -61.77°) in Newfoundland and Labrador, Canada, was selected because there is no lake or sea ice cover in the region. The area is covered with 6.62% of forest and a maximum SWE value of 0.29 m. During the snow accumulation phase from late October to late April, less than 20 days out of 180 days (four months) have non-zero NSCs with respect to SWE based on the ANN. Further, SWE sensitivity in the ANN is small with respect to the soil temperature sensitivity. Meanwhile, the SVM-based model Tb estimates are much more sensitive to SWE. It is also worth noting that when the daily SWE values change abruptly (indicated by the slope of the green lines in Figure 2.9 that results from a recent snowstorm, the NSC for the SVM model has a strong response (i.e., abrupt jump or drop in the NSCs) with

respect to the daily-change in SWE. However, when there is no change in SWE, such as the time period from 06 Feb 2004 to 16 Feb 2004, the NSC for both the ANN and SVM at all frequencies and polarizations remains close to zero. This suggests the ML algorithms are most sensitive under dynamic snow pack conditions during the snow accumulation phase.

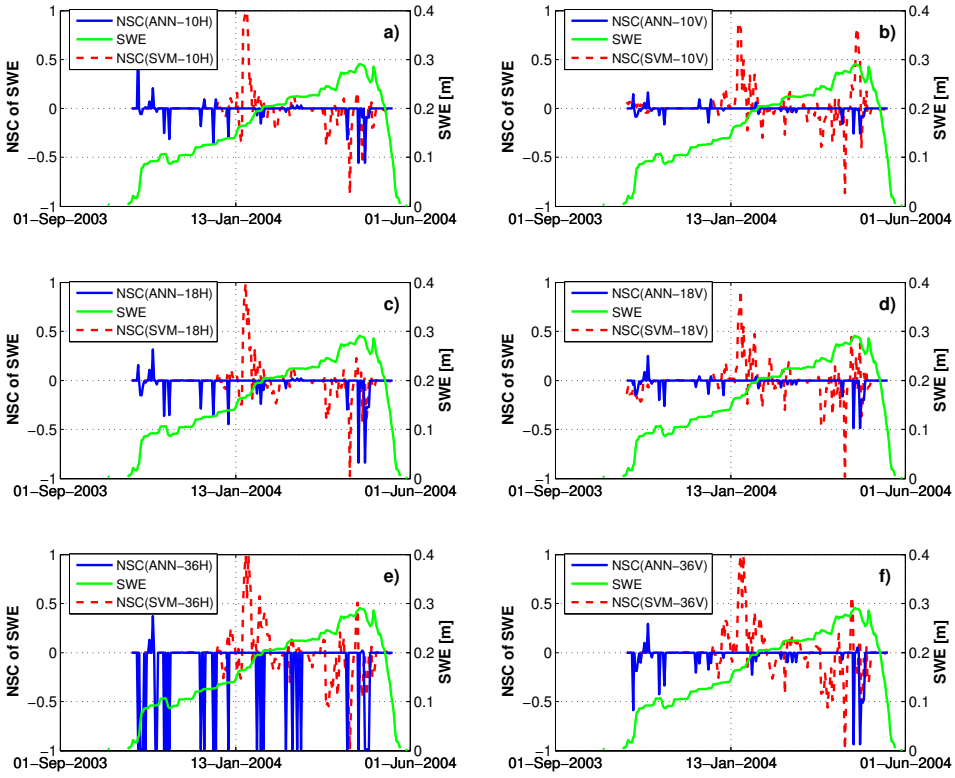

Figure 2.9: Time series investigation of NSCs with respect to SWE for 01 September 2003 to 01 June 2004 for a single location in Newfoundland, Canada where the forest cover is 6.62%. Subplots show a) 10H, b) 10V, c) 18H, d) 18V, e) 36H, and f) 36V.

During the snow ablation phase from the end of April to May, the SVM-based Tb estimates at all frequency and polarization combinations are relatively sensitive to changes in SWE. However, for the ANN-based Tb estimates, there is

little variability with respect to SWE that can be seen in Figure 2.9 when the snow pack is wet. Similar insensitivity is witnessed by the ANN with respect to other snow-related variables. For example, on the day of 05 May 2004, when the modeled snow liquid water content (SLWC) is at its maximum, NSCs with respect to SLWC for the ANN-based Tb estimate at 18V and 36V are both zero.

Another representative location of the high forest class (latitude 64.28° and longitude -146.17°) in the middle of Alaska, U.S., was selected because there is no lake ice cover in the region. The area is covered with 95.44% of forest and the maximum SWE is 0.19 m (see Figure 2.10). It is notable that the ANN-based SWE sensitivity is much smaller relative to the soil temperature. Alternatively, in this example, the SVM-based Tb estimates at all frequencies are sensitive to SWE during both snow accumulation and ablation phases. The ANN-based model, on the other hand, is much less sensitive to SWE during the snow accumulation phase. Less than 20 days out of 155 days examined here have non-zero NSCs for SWE using the ANN. Further, the magnitudes of NSCs are smaller compared with those in the low forest case. This is because the overlying forest tends to attenuate the snow-related signal from the underlying snow pack.

Similar behavior seen in the low forest case can also be seen in the high forest case shown in Figure 2.10. The NSCs with respect to SWE are generally higher and changing more rapidly during the snow ablation phase than those during the accumulation phase for both ML techniques. This is likely attributed to the effects of wet snow at this location where the presence of moisture within the snow pack causes the snow pack to behave as a strong emitter rather than a scatterer [83], and hence,

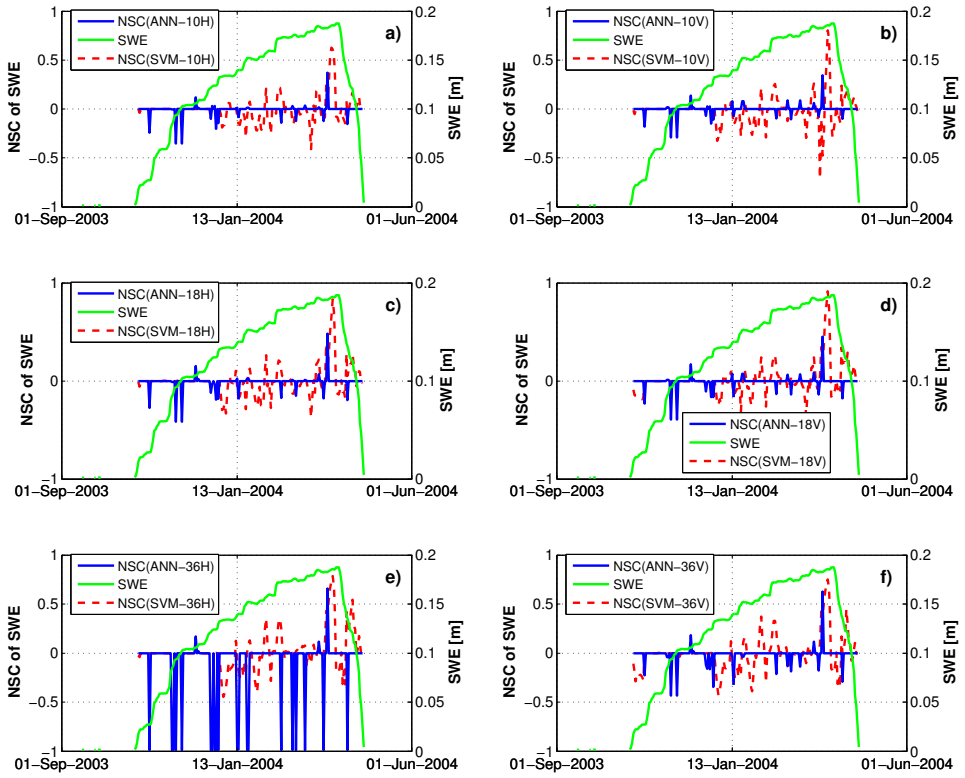

Figure 2.10: Time series investigation of NSCs with respect to SWE for 01 September 2003 to 01 June 2004 for a single location in central Alaska where the forest cover is 95.44%. Subplots show a) 10H, b) 10V, c) 18H, d) 18V, e) 36H, and f) 36V.

large changes in the AMSR-E Tb observations are commonly seen. Additionally, shorter wavelengths (i.e., 36V) are more responsive to snow-related variables than longer wavelengths (i.e., 18V) [78, 79] as revealed by higher computed NSC values, which suggest greater sensitivity due to increased scattering at shorter wavelengths. The effect on different PMW frequencies, however, does not fully reflect on the model sensitivity of SLWC during the snow ablation phase since SLWC is not computed as a function of snow pack layers, but rather as a column-integrated quantity.

2.4.3 Trade-off between Tb prediction accuracy and SWE sensitivity

An overparameterized (or underparameterized) SVM is likely to yield a sub-optimal measurement model, and hence, negatively impact the assimilation results. Therefore, a suite of SVM model input vectors were tested based on both SWE sensitivity (see [92] for details) and Tb prediction accuracy (see [60] for details). An example depiction of the relationship between SVM-based Tb predictions at 36.5 GHz with horizontal polarization across the entire Quebec and Newfoundland, Canada from 01 Jan 2004 to 14 Jan 2004 is shown in Figure 2.11. Similar performance is witnessed across other locations, frequency combinations, polarizations, and instances in time (results not shown). The "Goldilocks" region is defined as where the SVM has a relatively high prediction accuracy without sacrificing model sensitivity to SWE.

A total of 10 different Catchment-derived state variables, including SWE, snow liquid water content, top-layer soil temperature, skin temperature (a.k.a. radiative skin temperature of the terrestrial environment), bottom-layer snow density, mid-layer snow density, bottom-layer snow temperature, top-layer snow density, near-surface air temperature, and top-layer snow temperature were added one-at-a-time in accordance with increasing complexity based on the results of an earlier sensitivity analysis [61]. SWE sensitivity at model complexity q (q = 1, 2, $\cdots$, 10) is defined as the ratio between the NSC of SWE and the NSC of SWE when the model complexity is q = 1. The validation accuracy level at model complexity q is then defined as the ratio between the mean-squared error (MSE) achieved when q = 10 and the MSE

achieved when model complexity is q. The shaded region in Figure 2.11 is loosely defined as the "Goldilocks" region. Therefore, the SVM using Catchment-derived 1) SWE, 2) snow liquid water content, 3) top layer soil temperature, and 4) skin temperature were ultimately selected for use in this study.

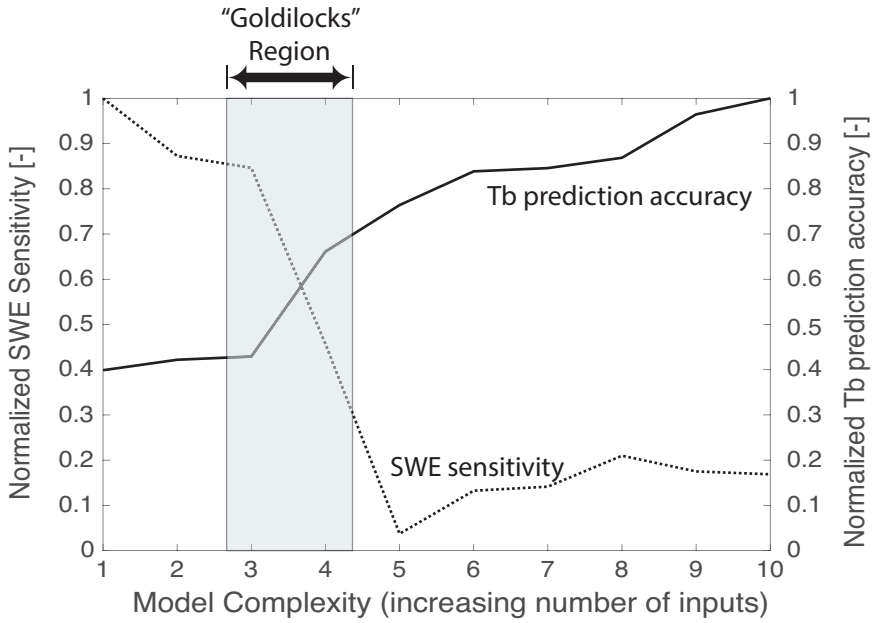

Figure 2.11: Relationship between SVM-based Tb prediction accuracy and SWE sensitivity.

2.4.4 The four-input-state SVM model sensitivity

2.5 Discussions and Conclusions

The sensitivity analysis of Tb estimates for both ANN and SVM models are performed with respect to different models inputs. Based on the computed NSCs, the key findings are summarized as follows:

(1) *Common features among ML-based models:* SWE sensitivities for both of the ML techniques are greatest in non-forested or sparsely-forested regions (i.e., less than 10% forest cover fraction) with relatively high amounts of snow.

(2) *Unique feature of the ANN-based model:* in highly vegetated areas, the sensitivity of the ANN-based model is more dominated by vegetative canopy, surface and soil temperature and less so with snow-related variables. This could be attributed to forest cover attenuation of the emission of radiation from the snow pack prior to reaching the PMW sensor [18, 73].

(3) *Unique feature of the SVM-based model:* in areas of dense vegetation and relatively low SWE, the SVM-based model shows significantly greater sensitivity to snow-related variables compared with those from the ANN-based model.

(4) *ML-based model sensitivity with respect to different model inputs:* compared to the vertically polarized Tb at 10.65 GHz and 18.7 GHz for the SVM-based estimates, Tb at 36.5 GHz tends to have a higher sensitivity with respect to small perturbations in the model input of SWE and top-layer snow temperature. This is partially explained by the fact that higher PMW frequencies possess a smaller emission depth. Hence, the 36.5 GHz channel captures more temporal variability related to the surface of the snow pack. In addition, microwave emission at 36.5 GHz is more responsive to snow pack scattering, which is indirectly associated with SWE estimates while the 18.7 GHz Tb data is less affected by snow scattering processes [78, 79]. It can be further concluded that the SVM-based model is more sensitive to snow-related variables, for example, SWE, TGI, and upper-layer snow temperature during both snow accumulation and ablation phases. Conversely, in

the ANN-based model, Tb estimates are relatively insensitive to TGI and snow density. Additionally, the ANNs sensitivity to SWE is more dependent on a specific location or a specific period of time. Alternatively, the ANN is more sensitive to the near-surface soil temperature across a range of locations and time periods. Hence, the SWE information is often overwhelmed by soil temperature information during ANN-based Tb estimation.

(5) *"Goldilocks region" of the SVM-based model:* the four-input-state SVM with Catchment-derived SWE, SLWC, top-layer soil temperature and skin temperature was selected for use within the proposed DA framework.

In order to explain the relatively low sensitivity to snow temperature and relatively high sensitivity to soil temperature in the ANN-based model, Forman and Reichle (2014) [60] discussed the step-function like behavior of the ANN-derived time series of Tb estimates at 18.7 GHz and 36.5 GHz. The top-layer snow temperature will vary more frequently in time than other soil-related properties since the overlying snow has more opportunities to interact with air and hence undergo more rapid changes in temperatures compared to the more insulated soil temperature. Therefore, it is postulated that the ANN-based model may have difficulty in capturing the high-frequency fluctuations (i.e., day-to-day variations) in the model inputs (e.g., top-layer snow temperature). One of the possible explanations for the insensitivity of the ANN-based model with respect to snow-related states may result from its learning algorithm and the fact that the solution is not guaranteed to converge to the global optimum during training. On the contrary, as discussed in Section 2.2, formulations of SVM-based models are convex and a unique global

optimum will be found.

In order to further explain the relatively high sensitivity to SWE in the SVM-based model compared with those in the ANN-based model, it is hypothesized here that the model response is strongly correlated with model structure and parameterization in the ML-based techniques. For instance, the selection of the number of hidden layer and hidden neurons in the ANN [9,84] and the regulation of the penalty parameter and the adjustable parameter in the kernel function in the SVM [85] are critical to defining ML-based model performance. Therefore, a different ML-based model configuration might lead to different model responses towards the model input state of SWE perturbation. In this study, the formulation of the SVM (i.e., selection of model parameters) is demonstrated to be more favorable at capturing SWE variability under different scenarios in ML-based Tb estimates. In conclusion, compared with the ANN, the SVM (with four-input-state) more properly reproduces the observed Tbs for the right reasons, is much more responsive to changes in snow pack conditions, and hence would presumably serve as a more effective measurement model operator at regional- and continental-scales for forested and non-forested areas as part of a Tb data assimilation framework aimed at enhancing SWE estimation.

Chapter 3: Assimilation of passive microwave brightness temperature observations into a land surface model with support vector machines for snow characterization in Alaska

3.1 Motivation and Objective

The relatively high sensitivity between the prior snow water equivalent (SWE) and the support vector machine (SVM)-based brightness temperature (Tb) predictions investigated in Chapter 2 suggests that SVM could serve as a computationally efficient measurement model operator for continental-scale snow data assimilation. Therefore, this chapter is intended to address the overarching science question: How can the predictability of SWE and snow depth at regional scales be enhanced through the systematic integration of passive microwave (PMW) measurements collected by satellite-based instrumentation and a machine-learning based algorithm into a land surface model?

3.2 Models, data, and methods

3.2.1 Land surface model and study area

The forward (prognostic) land surface model used in this study is the Catchment land surface model (Catchment) [70,86,87] forced by meteorological fields from the Modern Era Retrospective Analysis for Research Application (MERRA) [88] product developed at the Global Modeling and Assimilation Office at the NASA Goddard Space Flight Center. Catchment includes a three-layer snow regime [87] to model snow melt and re-freezing processes, including snow pack consolidation and metamorphosis. These attributes create a unique capability for Catchment in the assimilation of PMW Tb observations for the eventual goal of improving snow water storage estimation.

Catchment was run at a time increment of 450 seconds from 01 August 2002 to 30 June 2011 on the 25-km Equal Area Scalable Earth (EASE) grid. The temporal domain encompasses the full AMSR-E record. The study domain as illustrated in Figure 2.1 encompasses all of Alaska westward of 140° W. This region was selected because the domain includes a diversity of: 1) snow cover classes, 2) elevation ranges 3) land cover classes, and 4) a number of ground-based stations in terms of both snow observation and river discharge observation stations. Blue dots in Figure 3.1d) represent the 40 locations in Alaska with at least one set of in-situ snow observations covering a period of two or more years (see Section 3.2.2.2 for details).

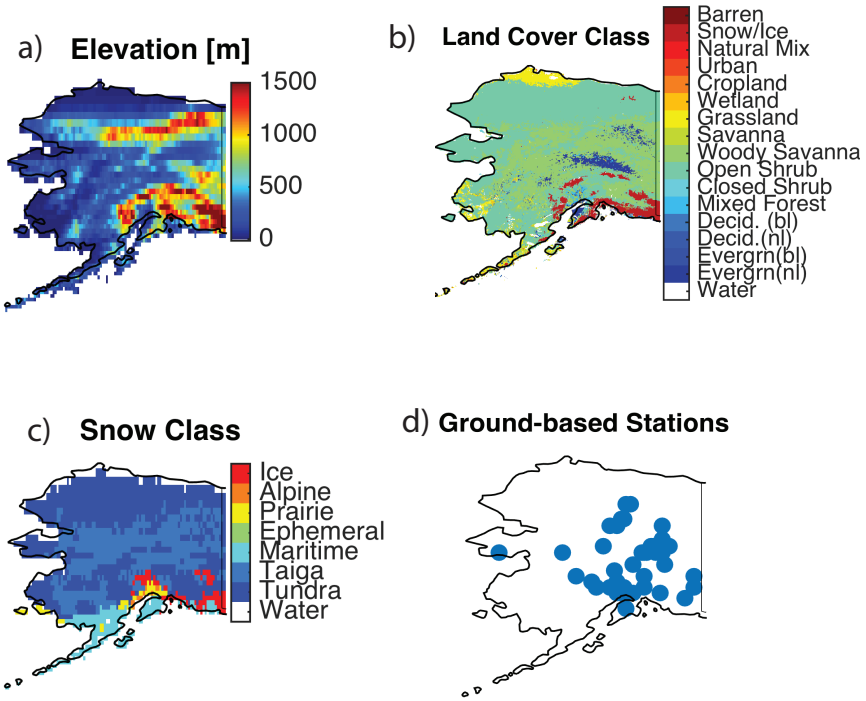

Figure 3.1: a) Global Land One-km Base Elevation Project (GLOBE) (aggregating onto the 25km EASE Grid), b) MODIS MCD12C1 land cover classification product, c) snow cover classification from Sturm et al., 1995 [74], and d) available ground-based stations.

3.2.2 Observations

3.2.2.1 Passive microwave brightness temperature observations

AMSR-E PMW Tb observations used here are on the 25-km EASE grid, which is coincident with the Catchment model grid. Only observations from the nighttime overpass (approximately 01:00 to 01:30 local time) were used in order to minimize wet snow effects. Daily AMSR-E observations at 10.65 GHz, 18.7 GHz, and 36.5 GHz

at both horizontal and vertical polarization were used. Three additional AMSR-E channels at 6.9 GHz, 23.8 GHz, and 89.0 GHz were not used in the experiment. Tb observations at 6.9 GHz were excluded because it has a much larger effective field-of-view (74 km $\times$ 43 km) relative to the re-gridded 25 km $\times$ 25 km EASE Grid pixel. Furthermore, Tb observations at 89.0 GHz and 23.8 GHz are contaminated with atmospheric-related Tb signals due to atmospheric attenuation and emission effects [28,89], and hence they were excluded. It is also worth noting that Tb observations at 18.7 GHz and 36.5 GHz are also affected by the overlying atmosphere [90, 91]. A relatively simple atmospheric decoupling procedure could be used here [92] to remove atmospheric-related Tb signals for both channels. However, no atmospheric decoupling is conducted here as to maintain a tractable project scope and to focus on more first-order effects (e.g., volume scattering by the snow pack). The use of an atmospheric decoupling procedure within a DA framework could be investigated in a follow-on study. (see Chapters 4 and 5).

3.2.2.2 Independent in-situ observations

Evaluations of model skill (with and without DA) were determined, in part, by comparisons against in-situ observations of SWE and snow depth. The Natural Resources Conservation Service (NRCS) National Water and Climate Center, installs, operates and maintains an extensive SNOwpack TELemetry (SNOTEL) network in Alaska. SNOTEL stations measure SWE (via snow pillows) and snow depth (via acoustic depth sensors) in daily increments. SNOTEL data used

here were obtained from https://www.wcc.nrcs.usda.gov/snow/. Further, independent, in-situ snow depth observations were obtained from the U.S. National Climatic Data Center Global Summary of the Day (GSOD) network operated by National Oceanic and Atmospheric Administration (NOAA). GSOD data used here were obtained from https://data.noaa.gov/dataset/global-surface-summary-of-the-day-gsod. Prior to the evaluation procedure, quality control of the ground-based SWE and snow depth observations was first conducted based on the criteria reported in [93] in order to eliminate erroneous data.

In addition, model-derived discharge estimates (with and without DA) were compared against available, daily-averaged, in-situ river discharge observations. These observations were obtained from the Alaska Geospatial Data Committee within the United States Geological Survey (USGS) via http://waterdata.usgs.gov/nwis/. Discharge observations were recorded as stage height and then converted to volumetric flow according to a well-calibrated stage-discharge relation. The runoff observations are used, in part, to test the hypothesis that improved SWE estimates (especially near peak accumulation) will yield improvements in model-derived runoff (in terms of both volume and timing) during the snow ablation season.

3.2.3 Data assimilation (DA) scheme

3.2.3.1 One-dimensional (1D) EnKF

This study employed a one-dimensional (1D) ensemble Kalman filter (EnKF) framework [94, 95] with new enhancements to better estimate snow-related states.

A key feature of the 1D-EnKF is that computational units were processed independently from one another, which is the same as assuming zero spatial error correlations between states from different units. The updated (or posterior) state (i.e., SWE), written as a scalar, x_t^{i+}, was estimated via linear update within a single computational unit as:

$$x_t^{i+} = x_t^{i-} + \mathbf{K}_t[(\mathbf{y}_t + \mathbf{v}^i) - \mathbf{\Phi}_t(x_t^{i-})] \tag{3.1}$$

where i represents a single replicate from the multi-replicate ensemble at time t; x_t^{i-} is the prior estimate of the state obtained from Catchment; $\mathbf{\Phi_t}(\cdot)$ is the observation model operator (i.e., a nonlinear SVM model); $\mathbf{y}_t$ is the observation vector; $\mathbf{v}^i$ is the temporally-uncorrelated observation error; and $\mathbf{K}_t$ represents the Kalman gain, which is used to weigh the uncertainties between the observation, the observation operator estimate, and the prior model estimate. Each term in the Equation 3.1 above is discussed in detail in the following sections.

Updating a model state such as SWE using information that is not SWE – Tb, per se – but rather contains information about SWE requires significant and reliable cross-covariances in the errors of both Tb and SWE. The underlying error correlation structure between the observation operator estimate of Tb and the prior land surface model estimate of SWE was explored in a sensitivity analysis [61], which demonstrated the potential to integrate predictions from a well-trained SVM model into a land surface model using a Bayesian merging process.

The Kalman gain matrix, $\mathbf{K}_t$, shown in Equation 3.1 houses the error structure information between the observation operator estimates and the prior (forward

model) states, which can be written as:

$$\mathbf{K}_t = \mathbf{C}_{xy,t} \left(\mathbf{C}_{yy,t} + \mathbf{C}_{vv} \right)^{-1}, \tag{3.2}$$

where $\mathbf{C}_{xy,t}$ is the error cross-covariance between the prior SWE estimates and the SVM-based (predicted) observations, $\mathbf{C}_{yy,t}$ is the error covariance of the SVM-based (predicted) observations, and $\mathbf{C}_{vv}$ is the observation error covariance.

Catchment was run in both open-loop (OL) mode (i.e., without assimilation) and with PMW radiance assimilation enabled. Catchment was initialized in July 2002 when snow cover is at a seasonal minimum and allowed to spin-up until 01 September 2002 when radiance assimilation was turned on. SWE was updated using the information content in the multi-frequency, multi-polarization PMW radiance emissions using Equation 3.1. Other snow-related states, including snow depth and snow heat content, were subsequently updated within Catchment during redistribution in order to ensure physical consistency and adhere to the fundamental laws of snow pack thermodynamics [49].

3.2.3.2 Machine-learning-algorithm-based observation operators

The expression, "$\mathbf{\Phi}_t(x_t^{i-})$", in Equation A.1 is also known as the "observation operator estimate" or "observation forecast" when using the observation (model) operator of $\mathbf{\Phi}_t(\cdot)$. Previous studies [59, 60, 62, 96] have shown that machine learning algorithms (ANN or SVM) can serve as an alternative to radiative transfer models for use as the observation operator during snow-related radiance estimation. This approach can be applied across regional- and continental-scales using either the

SSM/I, AMSR-E, or Advanced Microwave Scanning Radiometer 2 (AMSR2) Tb observation records. Due to the relatively high sensitivity to SWE in the SVM-based Tb predictions [61], the SVM is adopted here as the observation operator. The four most sensitive model input states derived from Catchment (i.e., snow liquid water content, SWE, top-layer soil temperature and skin temperature) were defined as the inputs during SVM training and prediction procedures [61]. The SVM-based observation operators outlined in [60] handle a near-infinite number of different combinations and permutations of input states. However, only four are selected here in order to maintain a tractable scope (see Chapter 2).

The first-order theory in passive remote sensing of snow, in general, predicts preferential scattering at higher frequency for either vertically- or horizontally-polarized PMW radiation [12, 28]. In other words, the deeper the snow, the greater the relative volume scattering between the two different frequencies. It is shown that the spectral difference between 10.65 GHz and 36.5 GHz ($\Delta Tb_{10-36} = Tb_{10} - Tb_{36}$) at either horizontal or vertical polarization could be used to determine snow depth and SWE in the context of medium to deep snow pack. Analogously, $\Delta Tb_{18-36}(= Tb_{18} - Tb_{36})$ could be used to determine snow depth and SWE in the context of shallow to medium snow pack [4, 89]. A series of synthetic experiments conducted in a separate study [97] also demonstrated that simultaneously assimilating multiple (synthetic) ΔTb observations yielded the best SWE estimate. Therefore, it is assumed here that a combination of four multi-frequency, multi-polarization spectral differences from AMSR-E could serve as the most informative means of relating PMW radiance information from AMSR-E to snow information as represented

by the Catchment model. A simplified flowchart of the multi-frequency and multi-polarization AMSR-E ΔTb assimilation scheme using a 1D-EnKF is shown in Figure 3.2.

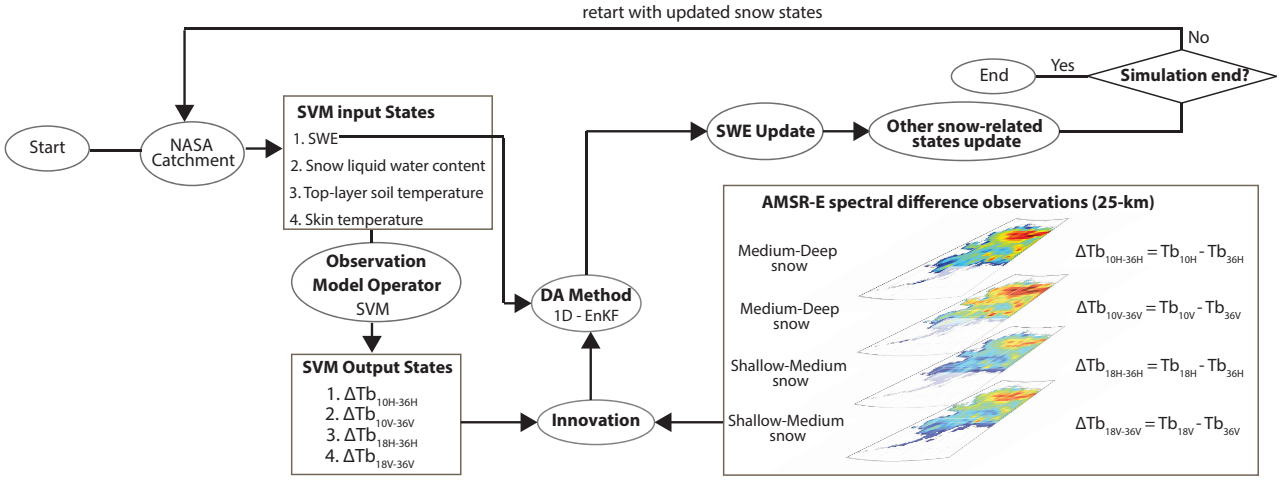

Figure 3.2: Schematic of the multifrequency and multipolarization AMSR-E ΔTb observations assimilation framework using a 1D-EnKF.

3.2.3.3 Observation error, ensemble size, and ensemble perturbation

In order to reduce the potential for filter divergence [68], a temporally-uncorrelated Gaussian-distributed observation error with zero mean was included in the EnKF algorithm as shown in the Equation 3.1. The added observation error is described mathematically as:

$$v^i \sim \mathcal{N}(0, \sigma^2) \tag{3.3}$$

where v^i is the observation error of the i^{th} replicate (i = 1, 2, ... N, where N is the ensemble size) drawn from the normal distribution with a mean of zero and

a standard deviation of σ. In this study, $\sigma = 2$ K was assumed for ΔTb observations of $\Delta\text{Tb}_{10H-36H}$, $\Delta\text{Tb}_{18H-36H}$, $\Delta\text{Tb}_{10V-36V}$, and $\Delta\text{Tb}_{18V-36V}$, respectively. The selection of the observation error standard deviation is partially based on the AMSR-E sensor performance characteristics stated as the observation precision is 1 K at one standard deviation [98]. Based on fundamental variance properties while assuming Tb observations at different frequencies are independent of each other, $\lceil \sigma_{\Delta Tb} \rceil = \lceil \sqrt{1^2K^2 + 1^2K^2} \rceil \approx 2K$ was first selected for each ΔTb observations, where $\lceil \cdot \rceil$ represents the ceiling of the argument.

The ensemble size, N, is another important consideration in ensemble-based filters [99]. A range of ensemble size were tested ranging from 16 to 64. An ensemble size of N = 32 was used based on the convergence of the mean SWE estimates across all ensembles for both OL and DA experiments. Ensemble sizes greater than 32 showed no significant change in the ensemble spread (i.e., standard deviation of the ensemble), hence it was determined that 32 replicates was reasonably adequate. In addition, the perturbation settings shown in Table 3.1 and Table 3.2 for model forcings follow the guidelines outlined in previous studies [49, 100–102].

Table 3.1: Model forcing perturbations used during ensembles generation.

Perturbation	Unit	Type [1]	Standard deviation
Precipitation	-	M	0.5
Shortwave radiation	-	M	0.3
Longwave radiation	W m^{-2}	A	20

[1] M = multiplicative perturbation; A = additive perturbation

3.2.4 Evaluation metrics and methods

3.2.4.1 Comparisons against state-of-the-art snow products

Three different publicly-available, satellite-based snow products were used for comparison against OL- and DA-derived snow estimates. In addition, ground-based in-situ observations were also used for comparison. The first satellite-based snow product is the European Space Agency (ESA) Global Snow Monitoring for Climate Research (GlobSnow) snow water equivalent (SWE) (version 2.0) [10, 52], which is based on a Bayesian spatial assimilation approach with spatial resolution of 25 km and a daily temporal resolution. GlobSnow SWE estimates were generated by combining a semi-empirical snow emission model [103] with space-borne PMW Tb observations from the Scanning Multichannel Microwave Radiometer, the Special Sensor Microwave/Imager, and the Special Sensor Microwave Imager/Sounder at both 18.7 GHz and 36.5 GHz in conjunction with ground-based observations obtained from adjacent weather stations. It is worth noting here that ESA does not provide SWE estimates in mountainous region with complex topography in order to avoid spurious or erroneous observations and estimates [10].

Table 3.2: Error structure in the model forcing perturbations.

	t_{corr} [2]	Cross correlations		
		Precipitation	Shortwave radiation	Longwave radiation
Precipitation	3 days	-	-0.8	0.5
Shortwave radiation	3 days	-0.8	-	-0.5
Longwave radiation	3 days	0.5	-0.5	-

The second satellite-based snow product – Canadian Meteorological Centre (CMC) Daily Snow Depth product [104, 105] – was produced based on optimal interpolation at a spatial resolution of 24 km and a temporal resolution of one day. The CMC product was generated by combining snow depth estimates from the Canadian forecast model with ground-based snow depth observations, including surface synoptic observations, meteorological aviation reports, and special aviation reports from the World Meteorological Organization information system.

The third satellite-based snow product – daily AMSR-E/Aqua L3 Global SWE product (version 2) [106] – was produced based on the observed AMSR-E spectral difference in accordance with [12, 107]. Additional enhancements were conducted to address forest cover effects on SWE estimation using ancillary forest fraction and snow density estimates [14].

3.2.4.2 Comparisons against in-situ snow observations and runoff observations

The relatively simple evaluation method utilized in this study was to compare satellite-derived SWE estimates with its nearest ground-based observations for both GSOD and SNOTEL stations within a radius of 0.25°. Using the closest, independent, ground-based observations as the "best" available information, a number of evaluation metrics were computed including bias, root mean squared error (RMSE), and normalized information contribution (NIC) (see Appendix B for details). In general, bias reflects the systematic error in estimates when compared against ob-

[2] t_{corr} = first-order autoregressive temporal correlation

servations whereas RMSE reflects both systematic and random errors. The standard interpretation of computed NICs is if NIC > 0, then DA-derived estimates are superior to OL-derived results whereas if NIC < 0, the DA-derived estimates are degraded relative to the OL-derived results. For NIC $= 0$, DA does not add any additional skill to the OL [40, 108].

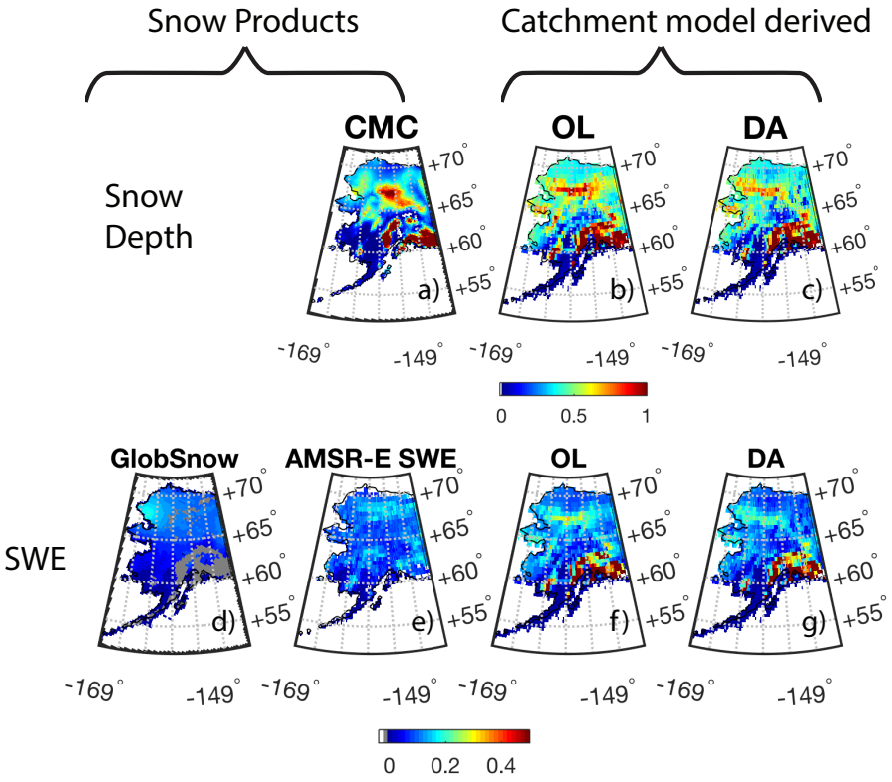

Figure 3.3: Average snow depth estimates obtained from a) CMC product, b) OL experiments, and c) DA experiments on 16 March 2003. Average SWE estimates obtained from d) ESA GlobSnow product, e) AMSR-E SWE product, f) OL experiments, and g) DA experiments on 16 March 2003. Grey regions in d) indicates the presence of the GlobSnow mountain mask.

3.3 Results and Discussions

3.3.1 Comparisons against state-of-the-art snow depth and SWE products

Figure 3.3 shows SWE and snow depth estimates on 16 March 2003. These results were compiled from the various snow products along with OL-derived and DA-derived estimates. Recall that GlobSnow does not provide estimates over mountainous regions, and therefore, a mountain mask is indicated by the grey-colored region in Figure 3.3 [10]. The date of 16 March 2003 is selected as an approximation for peak accumulation. For this date, the snow is neither too shallow nor too wet while at the same time the snow products were reported to achieve decent performance in other domains in the previous studies. For example, [109] concluded that GlobSnow peak SWE accumulation agrees well with AMSR-E SWE product in Kevo, Finland. [110] concluded that CMC agrees well with snow course observations in Canada during March. However, it is still found that a significant mismatch exists between GlobSnow and AMSR-E SWE products in Alaska as illustrated in Figure 3.3. Alternatively, CMC, GlobSnow, OL, and DA estimates share a similar distribution pattern. Although circumstantial, it is encouraging to see that when compared with OL estimates, DA-derived estimates tend to move towards better agreement with both CMC and GlobSnow for snow depth and SWE estimates, respectively.

3.3.2 Comparisons against ground-based observations

3.3.2.1 Ground-based discharge observations

Model-derived runoff estimates are compared against daily, in-situ discharge observations recorded at USGS gauge stations in Alaska from 2002 to 2011. In order to quantitatively measure how much information has been added to the model predictability as a result of assimilation, NICs, including NIC_{RMSE} and NIC_{NSE}, were computed during comparison against USGS discharge observations. It was found that approximately 40% (11 out of 28) of the basins degraded daily runoff estimation skill in DA relative to OL. Three out of 28 basins have zero NICs, and 14 out of 28 basins have positive NICs. The degradation of the DA in daily runoff predictability is indicated by either negative NIC_{RMSE} or negative NIC_{NSE}. The degraded behavior of the DA across some of the basins might be due to, but not limited to the lack of river routing routines within the Catchment model.

In order to minimize the effects of river routing, model-derived cumulative runoff estimates are compared against cumulative in-situ discharge observations recorded at USGS gauge stations in Alaska from 2002 to 2011. It was found that approximately 21% (six out of 28) of the basins degraded cumulative runoff estimation skill in DA relative to OL. Six out of 28 basins have negative NICs, and three out of 28 basins have positive NICs. Again, the degradation of the DA in cumulative runoff predictability is indicated by either negative NIC_{RMSE} or negative NIC_{NSE}. Among these six basins, two of them are with drainage areas below 235 km^2, which

are relatively small compared with the horizontal resolution of 25 km × 25 km for the model grid, and therefore, sub-grid scale variability in the modeled runoff might play a critical role in this case. In addition, one of the six basins has only four months (i.e., from 01 March 2011 to 01 July 2011) of in-situ discharge observations, which might not be sufficient to compare against. There might be other reasons to explain the degraded behavior of the DA across some basins, including (1) observation errors related to empirical stage-discharge relationship, or (2) the presence of ice jams, which are not accounted for in the model. Also, (3) dams, irrigation (small), or other management activities might affect in-situ observations. These issues are important, but are well beyond the scope of this current study. Despite the uncertainty in the discharge observations and relatively significant sub-grid scale variability in the modeled runoff across small basins, in general, relatively improved model behavior were achieved in the DA-derived cumulative runoff estimates relative to OL.

3.3.2.2 Ground-based snow observations

The AMSR-E SWE product, CMC snow depth product, GlobSnow SWE product, and model-derived SWE and snow depth estimates obtained from both OL and DA experiments are compared against ground-based, in-situ snow depth and SWE observations in Alaska from 2002 to 2011. It is worth noting here that the CMC snow depth product is not used to compare against GSOD observations since GSOD observations were directly integrated as part of the CMC reanalysis product gen-

eration, which violates the assumption of independence between the estimates and observations used during evaluation.

3.3.2.3 Effects of representativeness errors

The performance of Catchment is influenced, in part, by the representativeness of the ground-based station used during the model evaluation. Representativeness errors include the elevation difference between the ground-based station and the relatively large-scale model grid. In other words, it is relatively difficult to justify that each in-situ, ground-based SWE (or snow depth) measurement (with spatial resolution $\mathcal{O}(1)$ m^2) is spatially-representative of the colocated, large-scale satellite observations (with spatial resolution $\mathcal{O}(100)$ km^2). An example location is shown in Figure 3.4 in order to demonstrate the effect of representativeness errors. Both OL and DA-derived snow depth estimates have a bias $\approx$ 1 m and RMSE $\approx$ 1 m when compared against the closest GSOD observations (i.e., the distance between GSOD station and the EASE-Grid center is 0.02 degree). The relatively large bias and RMSE are, in large part, explained by the elevation difference between the ground-based station and the corresponding model pixel. The average elevation for the model pixel is 961.5 m whereas the elevation for the in-situ GSOD station is 167.6 m. Therefore, it is obvious that the closest ground-based GSOD station is not always representative of the snow conditions across the colocated model pixel. On the other hand, given similar elevation conditions between the SNOTEL station and the colocated model pixel (with an absolute relative elevation difference $<$

10%), both DA-derived SWE and snow depth estimates were superior to either the OL estimates, AMSR-E SWE retrievals, or CMC estimates in terms of lower bias and lower RMSE. Again, GlobSnow is not available at this location due to ESA's application of a mountain mask.

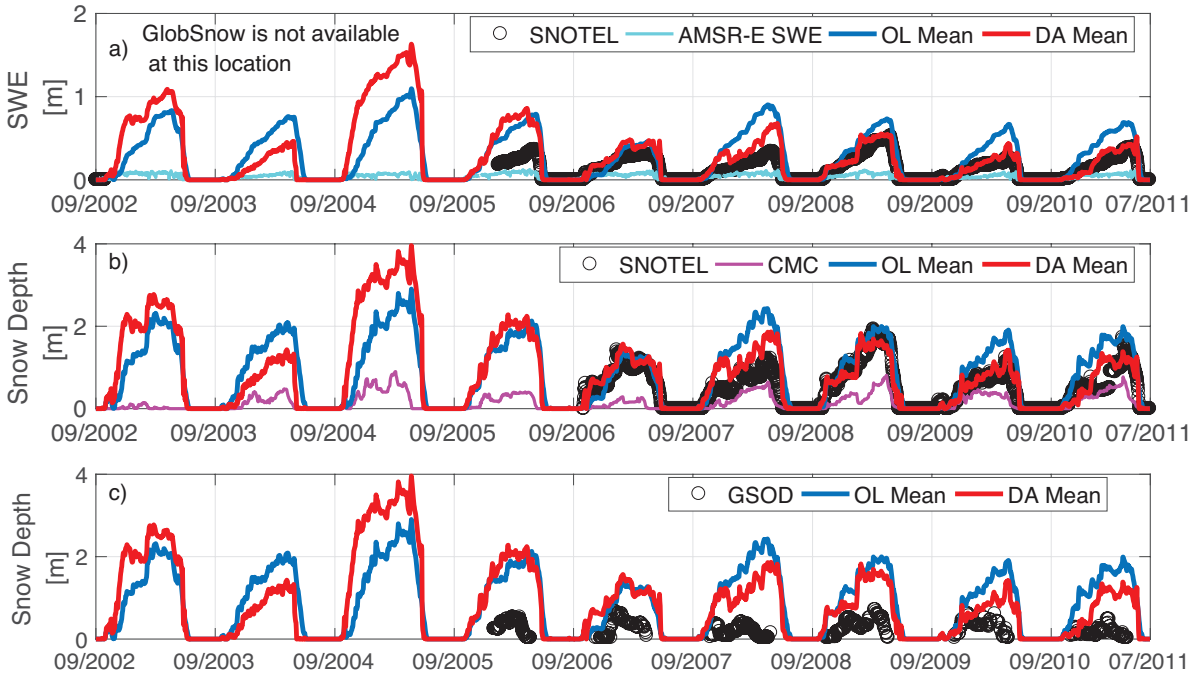

Figure 3.4: Example time series of a) SWE estimates, and b) c) snow depth estimates for (61.74° N, 148.89° W) from 01 Sep 2005 to 01 Jul 2011. Both OL and DA ensemble means were used to compare against AMSR-E SWE product, CMC snow depth product, in-situ SNOTEL SWE observations, in-situ SNOTEL snow depth observations, and in-situ GSOD observations. No estimates prior to 01 Sep 2005 were shown because ground-based observations were not available.

To minimize the effect of representativeness errors during model evaluation, pixels (five out of 40) that were significantly affected by elevation discrepancies (namely, when the absolute relative elevation difference $> 150\%$) were removed from

Table 3.3: Comparison against SNOTEL SWE observations, excluding mountainous regions (sample size = 9).

Experiment	Average bias [m]	Average RMSE [m]
OL	-0.016	0.044
DA	-0.014	0.043
AMSR-E	-0.010	0.048
ESA GlobSnow	-0.015	0.049

comparison. The box plots of computed relative elevation difference between ground-based stations and colocated model pixel are shown in Figure 3.5 after applying the elevation discrepancy threshold. The threshold of 150% is somewhat conservative and arbitrary, and was determined based on visualization of the elevation difference distribution across all available stations. Box plots shown in Figure 3.6 demonstrate the comparison results based on two statistical metrics used during evaluations (Tableted statistics were shown in Tables 3.3, 3.4, 3.5, and 3.6). GlobSnow was not available to compare against at high altitudes, and therefore, box plots with shaded-gray background were statistical metrics computed for stations (nine out of 35 stations) where GlobSnow has SWE estimates. It is worth mentioning that DA estimates were better than OL estimates, AMSR-E SWE retrieval, and GlobSnow in terms of a lower averaged RMSE ($\sim$0.06 m) and a close-to-zero averaged bias ($\sim$0.008 m). It is also noticeable that there is a relatively significant negative bias in the AMSR-E SWE product. The underestimation of the AMSR-E SWE retrieval could be attributed to snow grain size evolution, wet snow cover presence, sub-grid scale lakes, or signal saturation effects [26].

In general, DA outperformed OL in terms of reducing both systematic and

Table 3.4: Comparison against SNOTEL SWE observations (sample size = 15).

Experiment	Average bias [m]	Average RMSE [m]
OL	0.031	0.088
DA	0.008	0.065
AMSR-E	-0.027	0.070
ESA GlobSnow	N/A	N/A

Table 3.5: Comparison against SNOTEL snow depth observations (sample size = 21).

Experiment	Average bias [m]	Average RMSE [m]
OL	0.064	0.248
DA	-0.034	0.207
CMC	0.023	0.277

Table 3.6: Comparison against GSOD snow depth observations (sample size = 14).

Experiment	Average bias [m]	Average RMSE [m]
OL	0.008	0.261
DA	-0.020	0.230

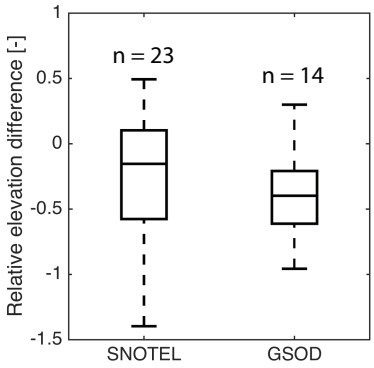

Figure 3.5: Box plots of computed relative elevation difference between SNOTEL stations (n = 23), GSOD stations (n =14), and colocated model pixels, where the variable n is the number of ground-based stations used for evaluation. The boxes show the median (marked as solid line in the box) along with the 25th and 75th percentiles whiles the whiskers show the 5th and 95th percentiles.

random errors in the modeled snow states. During the comparison against SNOTEL SWE observations (see Table 3.4), the bias was reduced by ∼73% and RMSE was reduced by ∼26% from the OL to DA. During the comparison against SNOTEL snow depth observations (see Table 3.5), the bias was reduced by ∼50% and RMSE was reduced by ∼17% from the OL to DA. During the comparison against GSOD snow depth observations, the bias was increased by ∼22%, but RMSE was still reduced by ∼12% from the OL to DA (see Table 3.6). The latter shows DA slightly overestimates the depth, but still managed to reduce the random error.

In order to quantitatively measure how much information has been added to the model predictability as a result of assimilation, NICs, including NIC_{RMSE} and NIC_{NSE}, were computed during comparison against SNOTEL SWE observations, SNOTEL snow depth observations, and GSOD snow depth observations (see Table

3.7). Due to the relatively high variability of NICs in the SNOTEL comparisons, Student's t-test suggests the computed mean NICs are not statistically different from zero at the significance level of 5%. The relatively high variability of NICs might be attributed to representativeness errors, noise in the assimilated Tb observations, or limitations in the SVM-based observation model operator. Figure 3.5 highlights the relatively wide variability (i.e., from -150% to +50%) in the computed relative elevation difference between SNOTEL stations and colocated model pixels, which helps illustrate variability arising from representative errors.

Unlike SNOTEL stations, ground-based GSOD stations have much less variability in the computed elevation differences, which is more likely to yield smaller variations in the computed NICs. During comparison against in-situ GSOD observations, the Student's t-test suggests rejecting the null hypothesis. The null hypothesis used in the Student's t-test (one tail) states the computed mean NIC metric is not statistically different from zero at a significance level of 5%. That is, DA reduces random errors in the snow depth estimates (in a statistically significant sense) as well as improves peak snow accumulation estimates relative to the OL. More work is required in the future to better minimize representativeness errors. However, even with a simple, conservative threshold applied here, it is clear that systematic improvement are made across the Alaska domain in terms of SWE and snow depth estimation.

Table 3.7: Computed NICs during comparison against SNOTEL SWE, SNOTEL snow depth, and GSOD snow depth observations. $\sigma_{NIC_{RMSE}}$ is the standard deviation of the NIC_{RMSE} whereas $\sigma_{NIC_{NSE}}$ is the standard deviation of the NIC_{NSE}. The null hypothesis used in the Student's t-test (one tailed) states the computed mean NIC metric is not statistically different from zero at a significance level of 5%. P-value indicates how likely the null hypothesis is true.

In-situ observations	Mean NIC_{RMSE} $\pm$ $\sigma_{NIC_{RMSE}}$	Mean NIC_{NSE} $\pm$ $\sigma_{NIC_{NSE}}$	Student's t-test (one tailed) @ 5%	p-value
SNOTEL SWE	0.06 $\pm$ 0.27	0.04 $\pm$ 0.49	accept the null hypothesis	0.21
SNOTEL snow depth	-0.02 $\pm$ 0.32	-0.15 $\pm$ 0.72	accept the null hypothesis	0.38
GSOD snow depth	0.09 $\pm$ 0.12	0.15 $\pm$ 0.22	reject the null hypothesis	0.007

3.3.2.4 Effects of land cover on 1D-EnKF

Evergreen needle leaved forest, woody savanna, and open shrub are the three land cover types used by Catchment in Alaska. Pixels covered with the same land cover type were categorized. Average NICs, including NIC_{RMSE} and NIC_{NSE}, were computed across each category as shown in Figure 3.7. Due to the limited sample size used during evaluation within each land cover category, none of the NIC values in Figure 3.7 are statistically significant based on the Student's t-test at a significance level of 5%. However, the sign-change behavior of the computed average NICs between different land cover categories is worth mentioning here, especially during comparison against SNOTEL SWE observations. In general, the NICs computed over the evergreen needle leaved forest pixels are the lowest as compared to woody savanna and open shrub types. In other words, DA added the least amount of information (or even degraded the model) relative to OL experiments in the forested regions for both SWE and snow depth estimation.

It is widely acknowledged that overlying vegetation tends to attenuate PMW radiation emitted from the underlying snow pack while simultaneously adding its own contribution to the signal as measured by the radiometer [111]. Therefore, it is hypothesized here that overlying forest cover is a significant factor that can impede DA performance. Removing the forest-related Tb signal from the observations prior to SVM training could be effective at decoupling non-SWE related Tb signals from the original AMSR-E Tb observations. A systematic forest decoupling procedure [92] could be beneficial in the extraction of information from the Tb observations that is most relevant to SWE estimation [112]. However, no forest decoupling procedure was conducted here as to maintain a tractable project scope. The use of a forest decoupling procedure within a DA framework will be investigated in Chapter 5.

3.3.2.5 Innovation and filter sub-optimality assessment

Kalman filter theory assumes unbiased observations and unbiased observation operator estimates, and thus, unbiased innovations [99]. Innovations, (a.k.a., residuals) are defined as the difference between observations and observation operator estimates. In an ensemble context, previous studies [49, 101, 113] investigated the normalized innovation (NI) sequence (see Appendix C) in order to assess filter performance. The NI sequence is a useful tool in assessing whether or not the error parameters listed in Tables 3.1 and 3.2 have been appropriately selected assuming the Catchment model and the observation model operator is linear and all errors (including both model and observation errors) are Gaussian [114]. The 1D-EnKF used

here employs a non-linear forward model with non-Gaussian model errors, hence, it is known *a priori* that the filter is sub-optimal in a minimized variance sense. However, the investigation of the normalized innovation sequence can still provide useful information as to the filter performance given the filter is sub-optimal [49, 101, 113].

It is worthwhile pointing out that multiple observations were assimilated at a given time and location in the DA experiment (in the form of multi-frequency, multi-polarization ΔTb observations). In order to assess filter sub-optimality given multiple observations, it is essential to compute the NI sequence separately for each observation channel using the diagonal elements of the observation error covariance and the observation operator estimate error covariance (see Appendix C for proof) [114]. If the NI sequence for each observation appears as white noise, then the filter is presumably extracting the most information from the available observations. Using $\overline{NI}$ to denote the temporal average of the NI sequence, it is found that the spatially-averaged $\overline{NI}$ are close to zero for each frequency and polarization combination as shown in Table 3.8. Further, the spatially-averaged σ_{NI} are generally greater than one. The relatively high σ_{NI} might be partially explained by the underestimation of observation error and/or observation operator estimate error. It might also be explained by the violation of (1) Gaussianity, and/or (2) linearity as required by the Kalman filter theory [99, 115]. Further analysis is required to better investigate the effect of observation error on the 1D-EnKF.

Table 3.8: Domain-averaged statistics of the NI sequences in Alaska from 01 Sep 2002 to 01 Jul 2011. $\overline{NI}$ represents the temporal mean whereas σ_{NI} represents the temporal standard deviation. Each column represents a different spectral difference, ΔTb, dependent on frequency and polarization combination.

ΔTb channel	10H - 36H	10V - 36V	18H - 36H	18V - 36V
$\overline{NI}$ [-]	-0.06	-0.02	-0.08	-0.05
σ_{NI} [-]	2.69	2.60	1.90	1.81

3.4 Conclusions and future work

This study explored the use of a SVM-based observation operator within a PMW radiance assimilation system in order to better characterize snow mass across regional and continental-scales. Results showed that DA-derived SWE and snow depth were consistently improved (relative to OL) after assimilating multi-frequency, multi-polarization ΔTb observations collected by AMSR-E. On average, the systematic and random errors in SWE estimates were reduced by $\sim$73%, and $\sim$26%, respectively. The systematic and random errors in snow depth estimates were reduced by $\sim$14%, and $\sim$15%, respectively. It is also encouraging to see that the relatively good snow estimates obtained from DA (relative to OL) also translates into cumulative runoff estimates when compared against in-situ USGS discharge observations.

A comparison against state-of-the-art snow retrievals showed that DA-derived estimates (relative to OL) tend to agree better with CMC and ESA GlobSnow products for snow depth and SWE estimates, respectively. AMSR-E snow retrieval, on the other hand, significantly underestimates SWE across Alaska. In general, the

improvements seen in the goodness-of-fit statistics as a result of the DA procedure are beneficial.

In addition, the study explored two important factors that impact DA performance. One factor is representativeness error between the ground-based, point-scale in-situ observations and the satellite-scale ($\sim$100 km^2) estimates. The disparities in horizontal support (resolution) are further exacerbated by differences in vertical elevation, which introduces precipitation bias. Given that representativeness errors exist, the positive NIC values computed using the GSOD observations suggest that DA reduces random errors in the snow depth as well as improves peak snow estimates relative to the OL. The other factor that might negatively affect the DA is the overlying vegetation cover. In general, the NICs computed over the evergreen needle leaved forest pixels are the lowest as compared to woody savanna and open shrub types. It is suggested that AMSR-E Tb observations (especially those collected over dense forest) should have the atmospheric and forest components decoupled from the snow-related portion of the Tb signal prior to assimilation [92].

Therefore, the study here shows the use of the SVM-based observation operator within a PMW radiance assimilation framework did show some promise in regional snow mass characterization. These preliminary findings are encouraging and suggest the potential for global-scale snow estimation as well as for further improvement via integrating with an atmospheric-and-forest decoupling procedure [92] to enhance snow estimation in forested regions.

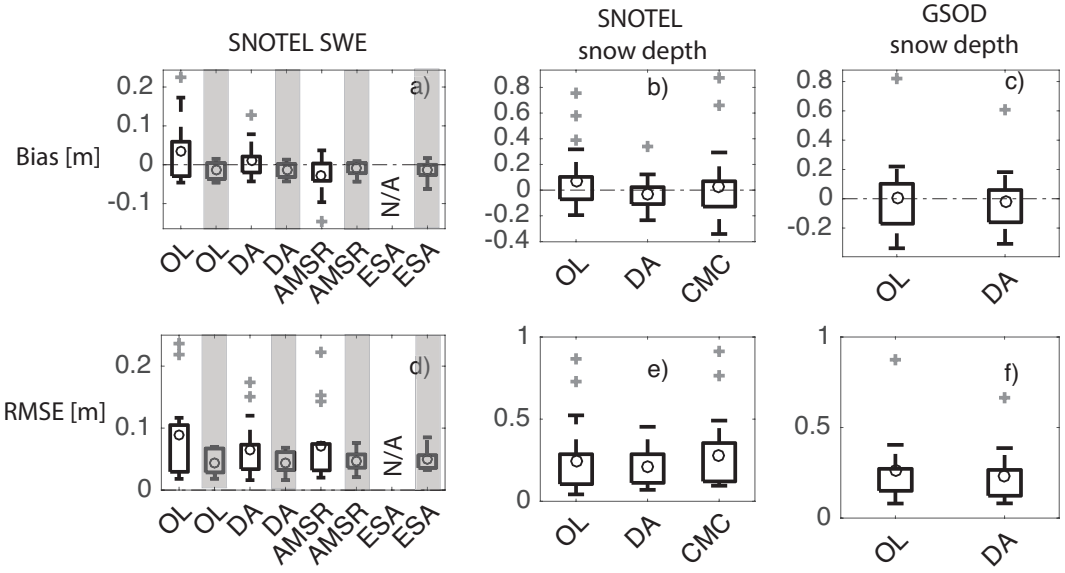

Figure 3.6: Box plots of statistical metrics computed from 01 Sep 2002 to 01 Jul 2011 for model-derived estimates (i.e, OL and DA ensemble means) and snow retrievals (i.e., ESA GlobSnow, CMC, and AMSR-E SWE) comparisons against in-situ observations. The top row is the computed bias whereas the bottom row is the computed RMSE. Each column corresponds to in-situ data sources, including SNOTEL SWE observations, SNOTEL snow depth observations, and GSOD snow depth observations as labeled. The boxes show the mean (marked as "o"s) along with the 25th and 75th percentiles whiles the whiskers show the 5th and 95th percentiles. The outliers are marked as "+"s. Box plots with gray-shaded background are statistical metrics excluding mountainous terrain because GlobSnow does not provide SWE estimates in mountainous regions.

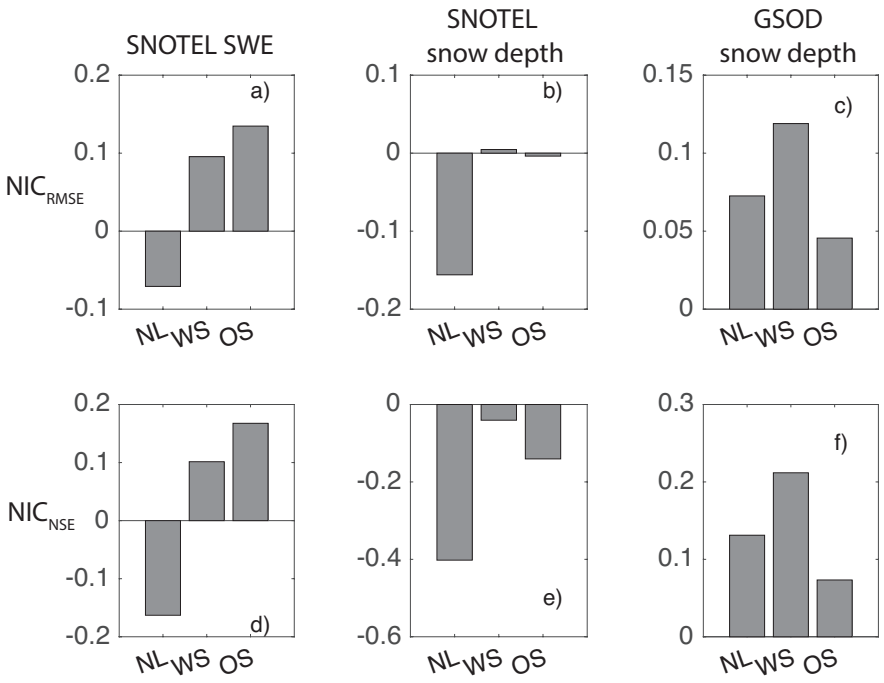

NL = Evergreen needle leaved forest; WS = Woddy savanna; OS = Open shrub

Figure 3.7: Average NICs computed for different land cover types in Alaska. The top row is NIC_{RMSE} and the bottom row is NIC_{NSE}. Each column correspond to in-situ data sources, including SNOTEL SWE observations, SNOTEL snow depth observations, and GSOD snow depth observations.

Chapter 4: Atmospheric and forest decoupling of passive microwave brightness temperature observations over snow-covered terrain in North America

4.1 Motivation and Objective

This chapter is intended to address two significant sources of uncertainty prevalent in snow water equivalent (SWE) retrievals derived from the Advanced Microwave Scanning Radiometer - Earth Observing System (AMSR-E) passive microwave (PMW) brightness temperature (Tb) observations at 18.7 GHz and 36.5 GHz. That is, the overlying atmosphere (i.e., atmosphere in between satellite-based sensor and the snow surface) attenuates surface emission while emitting its own radiation towards the satellite-based radiometer [90,116,117]. In the context of overlying vegetation, it is commonly acknowledged that vegetation attenuates PMW radiation emitted from the underlying snow pack and simultaneously adds on its own contribution to the signal as measured by the radiometer [76, 111, 118–120] (see Figure 4.1 and Equation 4.7 for details). In addition, previous studies reported that vegetation is known to damp the variability in the snow-related Tb signal that we wish to leverage [121], which further complicates the process of decoupling forest-related

information from the Tb observations. It is hypothesized here that vegetation moisture content effectively damps the variability in the diurnal temperature variation of the skin (vegetation canopy) temperature, and hence, leads to a decrease in the measured Tb signal variability, which further impacts the variability of the snow-related information embedded within the measured Tb signal. Therefore, it is important to decouple atmospheric and overlying forest effects from the original AMSR-E PMW Tb observations. The research presented here has been published in IEEE Journal of Selected Topics in Applied Earth Observations and Remote Sensing.

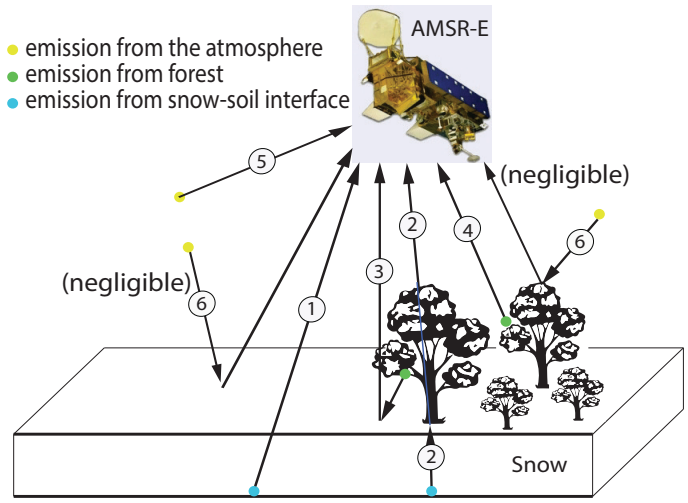

Figure 4.1: Contributions to observed PMW Tb as seen by AMSR-E. Marker ① is direct emission from snow-soil interface in forest-free regions; marker ② is direct emission from snow-soil interface under the forest canopy; marker ③ is downwelling forest emission reflected upward by the snow surface; marker ④ is direct forest emission; marker ⑤ is upwelling atmospheric constituent of the brightness temperature; and the marker ⑥ is downward atmospheric emission reflected back to the satellite, which is assumed negligible.

4.2 Methodology and Application

4.2.1 Atmospheric decoupling from PMW Tb observations

Atmospheric influence on measured PMW Tb is most notable when the observations are at high microwave frequencies (i.e., greater than 10 GHz) [122]. The observed Tb at frequency f, $Tb_{obs,f}$, with units of K as viewed from a satellite can be described as [73]:

$$Tb_{obs,f} = Tb^{\uparrow}_{atm,f} + Tb_{surf,f} \cdot t_{atm,f} \tag{4.1}$$

where the subscript f stands for frequency, $Tb^{\uparrow}_{atm,f}$ with units of K is the upwelling atmospheric brightness temperature, $t_{atm,f}$ is the atmospheric transmissivity (unitless), and $Tb_{surf,f}$ with units of K is the brightness temperature due to surface radiation emission given by [122]:

$$Tb_{surf,f} = (1 - e_f) \cdot Tb^{\downarrow}_{atm,f} + e_f \cdot Tb'_{surf,f} \tag{4.2}$$

where e_f is the surface emissivity (unitless), $Tb^{\downarrow}_{atm,f}$ with units of K is the downwelling atmospheric brightness temperature, and $Tb'_{surf,f}$ with units of K is the brightness temperature term due to the effective surface emission. Given the relatively high microwave emissivity of snow-covered land (e.g., typically 0.78-0.91 for dry winter snow pack and 0.98 for wet snow at frequencies between 10 GHz and 40 GHz [123]), the downward $Tb^{\downarrow}_{atm,f}$ component that is reflected back toward the satellite and then travels through the atmosphere was assumed negligible due to the relatively low (i.e., less than 0.05) reflectivity of the snow surface [73, 82].

The transmission coefficient, $t_{atm,f}$, was obtained from the optical thickness, τ_f, as [122]:

$$t_{atm,f} = \exp\left(-\frac{\tau_f}{\cos\theta}\right) \tag{4.3}$$

where θ is the incidence viewing angle toward nadir of the radiometer (i.e., 55° for the AMSR-E observations). Estimation of τ_f using semi-empirical equations as a function of the total precipitable water (TPW) [122, 124] was computed as:

$$\tau_f = a_{1,f} + b_{1,f} \cdot TPW \tag{4.4}$$

where hourly TPW estimates (with units of kg/m^2) were obtained from the NASA MERRA product [88] available through the NASA Goddard Earth Sciences Data and Information Services Center (GES DISC). $a_{1,f}$ (unitless) and $b_{1,f}$ (with units of mm^{-1}) are empirical regression coefficients [73, 122, 125]. Hence, the upwelling atmospheric Tb, $Tb^{\uparrow}_{atm,f}$, was computed in accordance with [122] as:

$$Tb^{\uparrow}_{atm,f} = (T_a - (c_{1,f} + d_{1,f} \cdot TPW)) \cdot (1 - t_{atm,f}) \tag{4.5}$$

where T_a is the near-surface air temperature (approximately 2 meters above the ground surface) with units of K derived from MERRA whereas $c_{1,f}$ with units of K and $d_{1,f}$ with units of $K \cdot m^2 \cdot kg^{-1}$ are empirical regression coefficients [122]. Thus, the atmospherically-decoupled Tb, $Tb_{decouple-noatm,f}$ with units of K can be estimated via:

$$Tb_{decouple-noatm,f} \approx \frac{Tb_{obs,f} - Tb^{\uparrow}_{atm,f}}{t_{atm,f}}. \tag{4.6}$$

PMW emission from snow-covered land can be measured using satellite-based or airborne radiometers. Due to the relatively short distance between the airborne radiometer and the snow-covered surface (less than 4 km compared to the 80-100 km

atmospheric thickness between the snow surface and the satellite-based radiometer), airborne observations are not significantly influenced by the atmosphere relative to the satellite-based observations. Therefore, it is assumed that airborne PMW Tb observations can be used as the "best available information" to assess atmospheric effects on coincident AMSR-E observations (in space and time) at 10.65 GHz, 18.7 GHz and 36.5 GHz at both vertical and horizontal polarizations. The evaluation of the proposed atmospheric decoupling procedure was conducted via comparison to the multi-band polarimetric airborne Tb measurements collected by Environment Canada (EC) [126] and the International Polar Year (IPY) Canadian Field Project Campaign [127, 128] that were subsequently aggregated up in space to the corresponding EASE grid cell via arithmetic averaging.

Only the decoupled 18.7 GHz and 36.5 GHz Tb observations are shown in the Results Section 4.4 since these two frequencies are most relevant for moderate SWE and snow depth estimation. Quality control of the airborne Tb observations was first conducted in order to eliminate individual observations collected during large deviations from the intended viewing angles of the radiometer associated with deviations in intended aircraft pitch, roll, and yaw.

4.2.2 Forest decoupling using atmospherically-decoupled PMW Tb observations

The atmospherically-decoupled Tb, $Tb_{decouple-noatm,f}$, is a mixture of signals received from both forested and snow-covered areas (see Figure 4.1) and can be

decomposed as:

$$
\begin{aligned}
Tb_{decouple-noatm,f} \quad = \quad & \underbrace{(1-F)\,Tb_{snow,f}}_{(1)} + \cdots \\
& \underbrace{F\,t_{forest,f}\,Tb_{snow,f}}_{(2)} + \cdots \\
& \underbrace{F\,t_{forest,f}\,(1-\omega_{forest})(1-t_{forest,f})\,(1-e_{snow,f})\,T_{forest}}_{(3)} + \cdots \\
& \underbrace{F\;(1-\omega_{forest})\,e_{forest,f}\,T_{forest}}_{(4)}
\end{aligned}
\tag{4.7}
$$

where F is the forest fraction obtained from the MODIS forest product (MOD44B) [75, 129]; T_{forest} with units of K is the canopy (skin) temperature obtained from the NASA Catchment land surface model (Catchment; [70]); $t_{forest,f}$ is the forest transmissivity and is unitless; $e_{forest,f}$ is the forest emissivity that can also be written as (1 - $t_{forest,f}$) and is unitless; $e_{snow,f}$ is the snow emissivity and is unitless; ω_{forest} is the forest single scattering albedo and is unitless. Due to the relatively small magnitude of the single scattering albedo in the domain of interest (i.e., woody savanna and evergreen needle leaved forest covered regions) [130, 131], it is assumed negligible in this study for all four frequency and polarization combinations [73]. $e_{snow,f}$ was computed as the ratio between the Tb of the snow ($Tb_{snow,f}$) and the physical temperature of the snow pack (T_{snow}) where T_{snow} was obtained from Catchment. Except for $Tb_{snow,f}$, only one unknown parameter in Equation 4.7 exists, namely, forest transmissivity. The forest transmissivity mapping procedure is discussed in more detail below.

4.3 Forest transmissivity mapping using a first-order, physically-based radiative transfer model

Three different forest transmissivity retrieval models [73, 132, 133] were tested using different biophysical vegetation parameters. The three different parameters (and products) include: a) the MODIS global leaf area index (LAI) and fraction of photosynthetically active radiation Collection 5 product (MCD15A2), b) a re-processed global LAI product derived from MODIS observations and produced at Beijing Normal University (BNU) [134], and c) a stem volume (SV) retrieval product [135]. Initial testing suggest the first-order transmissivity model employing the BNU LAI product as applied in Equation 4.7 was most appropriate (further discussions provided below).

The first-order radiative transfer model used during forest transmissivity estimation was computed as [73, 111, 133]:

$$t_{forest,f} = \sqrt{\frac{Tb_{obs,f} - T_{forest}}{Tb'_{obs,f} - T_{forest}}} \tag{4.8}$$

where $Tb'_{obs,f}$ is the spatially-averaged, original (i.e., coupled) Tb observations at non-vegetated, snow-covered pixels (i.e., LAI=0) whereas $Tb_{obs,f}$ is the Tb observation at vegetated pixels (i.e., LAI $\neq 0$) adjacent to the geometric center of the non-vegetated snow-covered pixels (see Figure 4.2 for an example). The original Tb observations, instead of atmospherically decoupled Tb estimates, were used here such that the forest transmissivity retrieval is independent of the atmospheric-related Tb decoupling procedure. Furthermore, calculations using atmospherically-decoupled

Tb values as applied in Equation 4.8 suggested the LAI-transmissivity relationship was not significantly impacted since the magnitude of the atmospherically-contributed Tb is relatively small compared to the original Tb observations (i.e., two orders of magnitude smaller than the original Tb observations). The BNU LAI (with an increment of 0.1 m^2 leaf m^{-2} ground) conducted an additional analysis beyond the original MODIS LAI product produced at NASA for the period of 2001 through 2013 with an 8-day time step and a 1-km resolution on a sinusoidal grid. LAI "tiles" were subsequently re-gridded using Delaunay triangulation onto the 25 km $\times$ 25 km EASE-Grid for each 8-day period. The re-gridding practice was necessary in order to align all relevant information sources, including forest cover fraction, snow cover class, land cover type, Catchment-based model outputs, MERRA-derived TPW, and Tb observations on a coincident grid. The study also compared three different interpolation methods (i.e., nearest neighbor, natural neighbor and linear interpolation). It was found that the LAI difference between any two of these three interpolation methods was bounded between -0.1 and 0.1 within the study domain. Therefore, it is believed that the re-gridding process introduced less uncertainty relative to that associated with parameter error or model structure error introduced in the LAI retrieval procedure (see Appendix D for details).

A SWE threshold of 10 mm is used as the lower limit in the investigation at which a pixel is considered snow-covered, which is consistent with the lower threshold used in previous studies [59–61] as well as in accordance with other published recommendations [136]. Ideally, only pixels covered with the same type of snow (according to the seasonal snow cover classification system proposed by [74]) and

with exactly the same amount of modeled SWE should be selected in both vegetated and non-vegetated regions. This practice was deemed effective in the process of de-correlating snow Tb information content from the mixed PMW Tb observations in the vegetated regions such that forest-related Tb contributions could be extracted as a function of the LAI variation only. However, it is important to note that SWE values were obtained from the Catchment land surface model output and are inherently uncertain due to model structure and parameterization errors [7]. Therefore, the criteria for selecting pixels with similar amounts of SWE was defined as the difference between the maximum and the minimum SWE values between a given set of pixels and should not exceed 0.04 m. The value of 0.04 m was selected based on the SWE estimation uncertainty analysis shown in [7] that considered both model bias and root mean squared error. A range of SWE estimation difference thresholds was also tested that ranged from 0.01 m to 0.05 m. A threshold of 0.04 m was ultimately selected because it yielded a sufficient sample size as well as reasonable representation of PMW Tb magnitudes across non-vegetated, snow-covered land.

Since LAI is a valuable source of information due to its ability in distinguishing between vegetated and non-vegetated land, the accuracy of the regional daily LAI mapping (with a particular interest over snow-covered land) might adversely impact the forest-related portion of the Tb decoupling procedure. Recent studies demonstrated that MODIS-based LAI values are discontinuous and inconsistent in space and time due to the presence of clouds and seasonal snow cover [137, 138]. Therefore, this study employed an alternative LAI product produced at BNU [134] during the forest decoupling process to help mitigate the presence of clouds and/or

snow cover. Further, the study refers to the method of searching for adjacent pixels matching the criteria as a "spatial localization" approach. Localization is defined here as a procedure that employs a cutoff distance that excludes the pixels beyond a certain threshold distance (defined *a priori* by the user) from the center of the target. In this study, the localization length is set to seven degrees to ensure that the resulting sample size is large enough while also increasing the likelihood that samples are effectively grouped by similar climatology (see Figure 4.2).

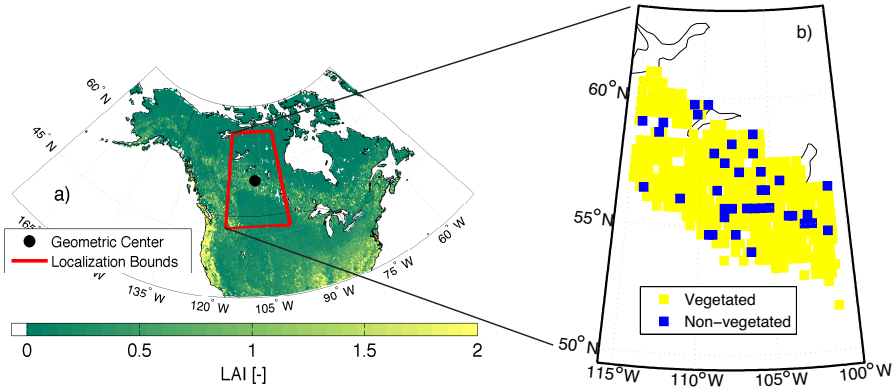

Figure 4.2: An example of remapped BNU LAI in North America on 06 Mar 2003 is shown in Figure 4.2a). The geometric center of the non-vegetated (i.e., LAI=0) taiga snow covered land is marked as a black dot. The localization bounds are marked as red lines where the distance between each bound and the geometric center was set to seven degrees. Evergreen needle-leaved forest covered pixels colocated with taiga snow cover are marked as yellow squares in Figure 4.2b) whereas non-vegetated land colocated with taiga snow covered pixels are marked as blue squares.

Four assumptions were required before calculating Equation 4.8 en route to estimating forest transmissivity as a function of microwave frequency and polarization. First, the study only focuses on dry snow conditions, which allows for a strong radiometric contrast between vegetated and non-vegetated areas over snow-covered

terrain [133]. Therefore, only locations with non-zero snow depth (as estimated by Catchment) during early December to late March and zero snow liquid water content as estimated by the Catchment model (i.e., negligible liquid water coats the individual snow grains [122]) are defined here as "dry snow" pixels. In addition, it is necessary to assume a relatively stable and nearly uniform temperature profile above the snow surface over a distance of meters in order to avoid a significant amount of heat transfer between the overlying canopy, the overlying air, and the underlying snow pack. Therefore, only pixels with Catchment-derived skin temperature (T_{forest}) and physical snow temperature (T_{snow}) within +/- 2 K of one another as estimated by the Catchment model. The +/- 2 K was selected to approximate the uncertainty of Catchment-derived estimates across different landscape elements within the satellite field-of-view [139]. Further, it is believed that Equation 4.8 should be employed as a function of snow class and land cover type across snow-covered portions of the North America domain. This is because: (1) land cover type has a strong influence on the brightness temperature of dry snow-covered terrain [111, 140], and (2) snow class has been shown to impact SWE estimation accuracy [78]. Additional assumptions include that changes in biotic disturbances (e.g., large-scale deforestation), land cover classification, and snow cover classification (see Figure 4.3) are relatively constant across the time period of investigation. It is acknowledged that the emissive properties of the soil beneath the snow pack will also influence the brightness temperature observations. However, previous study [27] showed that the use of the spectral difference algorithm is assumed to minimize many of the errors in the SWE and snow depth retrieval (see Section 4.3.1 for details) such as the dielectric constant

of the soil and the surface roughness.

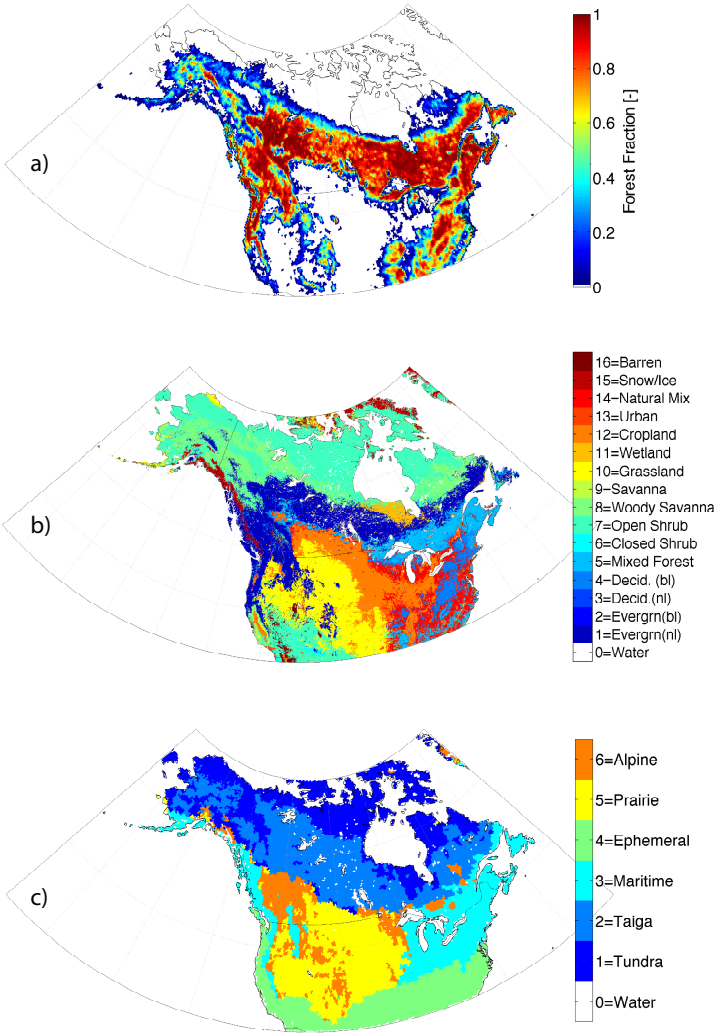

Figure 4.3: Remapped forest cover distribution from [75] is shown in Figure 4.3a), remapped MODIS MCD12C1 land cover classification product in North America is shown in Figure 4.3b), and remapped snow cover classification from [74] is shown in Figure 4.3c).

4.3.1 Forest decoupling model evaluation

Since upward and downward radiometer observations below and above the canopy, respectively, are not available, the evaluation of the forest decoupling is made here *indirectly* via comparisons with ground-based SWE and snow depth measurements as well as against satellite-based SWE and snow depth retrievals. A relatively simple snow depth-Tb relationship for a dry, uniform snowfield in the absence of overlying vegetation can be expressed as [12]:

$$SD = 1.59 \times (Tb_{18,H} - Tb_{36,H}) \tag{4.9}$$

where SD is the snow depth in centimeters (cm); $\mathrm{Tb}_{18,H}$ denotes the Tb with units of K at 18.7 GHz and horizontal polarization; and $\mathrm{Tb}_{36,H}$ is the Tb with units of K at 36.5 GHz and horizontal polarization. The study shown in [141] improved the snow retrieval and applied it in forested regions in order to compute snow depth as:

$$SD = 1.59 \times \frac{(Tb_{18,H} - Tb_{36,H})}{1 - ff} \tag{4.10}$$

where SD is the snow depth in centimeters (cm), ff is the dimensionless forest cover fraction, and the calibrated coefficient value of 1.59 has units of cm/K.

During SWE retrieval using a spectral difference of Tb (ΔTb), the following three empirical equations could be used. If the snow is homogenous with a mean snow grain radius of 0.3 mm and a snow density of 300 kg m^{-3}, the SWE-Tb relationship can be expressed as:

$$SWE = 4.8 \times (Tb_{18,H} - Tb_{36,H}) \tag{4.11}$$

where SWE is the snow water equivalent in millimeters (mm) and the calibrated coefficient value of 4.8 has units of mm K^{-1} [12]. Without the assumptions of snow grain size and density, a more generalized equation was proposed by [142] for estimating SWE that could be written as:

$$SWE = a + b \cdot (Tb_{18,H} - Tb_{36,H}) \tag{4.12}$$

where SWE is the snow water equivalent in millimeters (mm) and the coefficients a and b are -25 mm and 4.8 mm/K, respectively [15]. In forested areas, Equation 4.12 can be re-written as [15]:

$$SWE = a + b \cdot (Tb_{18,H} - Tb_{36,H})(1 - ff) \tag{4.13}$$

where SWE is the snow water equivalent in millimeters (mm) and ff is the dimensionless forest cover fraction.

In addition to snow mass retrieval equations computed as a function of ΔTb (i.e., $\Delta Tb = Tb_{18H/18V} - Tb_{36H/36V}$), comparisons were also conducted during forest decoupling validation activities against available in-situ SWE measurements such as the Natural Resources Conservation Service (NRCS) National Water and Climate Center SNOwpack TELemetry (SNOTEL) network (http://www.wcc.nrcs.usda.gov/snow/) as well as the U.S. National Climatic Data Center Global Summary of the Day (GSOD) network operated by National Oceanic and Atmospheric Administration (NOAA) (https://data.noaa.gov/dataset/global-surface-summary-of-the-day-gsod). As stated previously, since Tb observations above and below the canopy are not available for use, the resulting impact on the snow depth retrieval or SWE retrieval

is used here as a proxy to assess the efficacy of the proposed forest decoupling procedure. It should also be noted that the computed improvements to goodness-of-fit statistics (e.g., root mean squared error (RMSE), bias, and unbiased RMSE; see Appendix B for details) are complicated by additional uncertainty due to a spatial scale mismatch between the satellite-based estimates (with spatial resolution $\mathcal{O}(100)$ km^2) and ground-based observations (with spatial resolution $\mathcal{O}(1)$ m^2) where $\mathcal{O}(\cdot)$ represents order-of-magnitude. In other words, it is relatively difficult to justify that each in-situ, ground-based SWE (or snow depth) measurement is spatially-representative of the colocated, large-scale satellite observations. However, in the absence of spatially-dense observational networks, these comparison results are useful since they can serve as a proxy demonstrating the effectiveness of the proposed forest decoupling technique.

4.4 Results and Discussions

4.4.1 Results of atmospheric decoupling

Tb observations shown as whisker-and-box plots in Figures 4.4a), b), c), d and e) were obtained from the EC airborne survey on 13 Mar 2006, 26 Feb 2008, 03 Apr 2008, 08 Apr 2008, and 10 Apr 2008, respectively. Observations in Figures 4.4f), g), and h) were obtained from the IPY helicopter flights on 21 Feb 2008. The original (i.e., coupled) AMSR-E Tb measurements and the decoupled Tb (i.e., after atmospheric decoupling) are marked on each of the plots in Figure 4.4. It is noticeable that after conducting the atmospheric decoupling procedure, compared

with the original AMSR-E measurements, the decoupled Tb values are closer to the median of the aggregated EC and IPY Tb observations. In general, the atmospherically contributed component of Tb ranges from 1 K to 3 K depending on the frequency and TPW content at the time of AMSR-E overpass. However, relatively large adjustments were witnessed for AMSR-E Tb observations at shorter wavelengths (e.g., 36.5 GHz) since they are less transparent to the overlying air due to the relatively low transmission factor (see Equations 4.3 and 4.4 for details). Even though the improvements are small, they systematically improve the Tb estimates relative to the independent airborne Tb observations and suggest viability in the proposed approach.

It is also interesting to note that the amplitudes of atmospherically contributed Tb information content obtained from [131] are 21.3 K at 18.7 GHz and 29.2 K at 36.5 GHz, respectively, which is approximately 10 to 20 times greater than those derived from the radiative transfer model presented in this study. It is also worth noting that the time period of interest in this study is vastly different from that investigated in [131]. That is, the temporal domain selected in this study is from late December to early March whereas results concluded in [131] were analyzed in the summer season, namely from July to October in Quebec, Canada. Therefore, a larger amount of TPW in the summer might result in higher magnitudes of upwelling atmospherically-contributed Tb components. In addition, it is postulated that influences in the empirical coefficients used in Equations 4.4 and 4.5 might be responsible for the large differences between these two studies in terms of deriving atmospherically-contributed Tb as a function of TPW. On the other hand, a study

conducted on the Tibetan Plateau [91] found that the average atmosphere-related Tb contribution at 18.7 GHz and 36.5 GHz was approximately 0.3 K, and 0.5 K, respectively. Compared with Qiu et al. [91], the atmosphere decoupling results derived from this current study are much smaller at both AMSR-E frequencies. This is mostly likely due to the relatively thin and dry air in the cloud-free winter days on the Tibetan Plateau where the water vapor concentration is low. When compared with the AMSR-E decoupling results from [90] that used a different radiative transfer model [143] and was applied during winter season using parameters derived from available rawinsonde observations collected in the U.S., this current study yields relatively similar magnitudes of Tb components related to atmospheric emissions, i.e., $\mathcal{O}(1)$ K depending on the relevant frequency of interest. Therefore, it is believed that the atmospheric decoupling procedure in this study is effective for use during removing atmospheric-related Tb signals at both 18 GHz and 36 GHz.

4.4.2 Results of forest decoupling

4.4.2.1 Forest transmissivity retrieval

Forest transmissivity retrieval was conducted as function of snow class, land cover type, microwave frequency, and polarization across snow-covered land in North America. Among all 16 land cover types (see Figure 4.3), evergreen needle leaf, mixed forest, and woody savanna are the three dominant categories that are most likely to be colocated with appreciable snow cover. Mixed forest is defined as a transitional zone and often consists of mosaicked forest communities [144]. The intrinsic

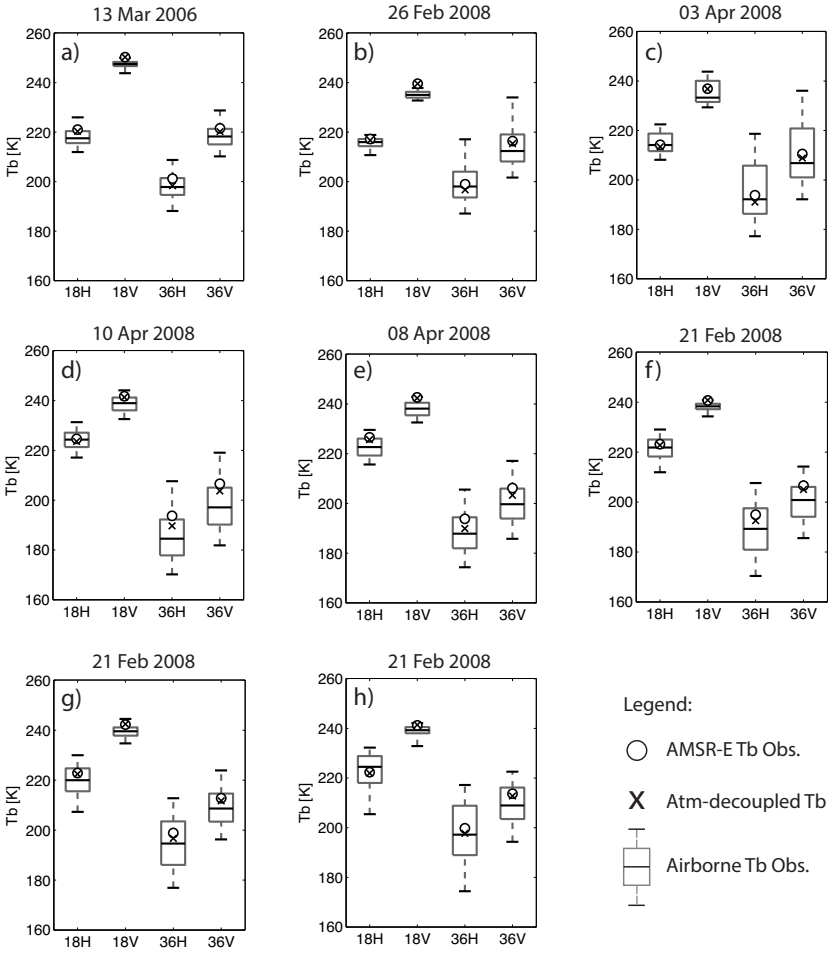

Figure 4.4: Atmospherically-decoupled satellite-based Tb estimates compared against spatially-aggregated airborne Tb observations. AMSR-E measurements are marked as dots and atmospherically-decoupled Tbs are marked as 'x's. The boxes show the median (marked as the black line in the box) along with the 25th and 75th percentiles while the whiskers show the 5th and 95th percentiles.

nature of the mixed forest category makes it difficult to retrieve transmissivity based on structural similarities [145] and is well beyond the scope of this current study. Unlike the mixed forest class, woody savanna and evergreen needle-leaved forest classifications are not typically associated with forest-transitional zones [144]. Woody savanna is defined as the land cover dominated by herbaceous systems and is mostly found north of 60° latitude and is often colocated with snow cover classes of taiga and tundra according to [74]. Further, evergreen needle-leaved forest dominates over other forest types in snow-covered terrestrial environments across North America, and is closely colocated with seasonal snow cover classes of taiga, maritime, prairie, and alpine snow [74].

Figures 4.5 and 4.11 show a consistent relationship between LAI and forest transmissivity where forest transmissivity decreases as LAI increases across woody savanna and evergreen needle-leaved forest regions. When the remotely-sensed value of LAI is numerically zero (i.e., negligible vegetation present), forest transmissivity is unity. As LAI increases, transmissivity asymptotically approaches a lower threshold. This lower threshold is also known as the "saturated transmissivity", which represents the transmissivity value for a very dense forest covered pixel [133]. The "very dense" forest cover in this study is defined as pixels with winter LAI values greater than 2 m^2 leaf m^{-2} ground or SV values greater than 250 m^3 ha^{-1}. The relationship between transmissivity and LAI could be modeled as an exponential function [132, 133] taking the form as:

$$t_{forest,f} = a + (1 - a) * \exp(-b * LAI) \tag{4.14}$$

where a and b are unitless regression coefficients. Transmissivity values greater than 1.0 as calculated from Equation 4.8 arise due to inherent uncertainty in the Catchment model outputs (i.e., skin temperature and SWE estimates) in conjunction with observation error in the MODIS-derived LAI observations.

The exponential function derived in this study requires a minimum of 25 samples and can often exceed more than 100 samples. However, it is still difficult to ensure that these samples are equally distributed within each LAI bin. That is, LAI values are relatively low and stable during the winter season (due to low growth rates) in evergreen needle-leaved forest and woody savanna regions. A lack of samples with relatively high values of LAI (marked as grey squares in Figures 4.5 and 4.11) may yield a less robust estimate of transmissivity. Therefore, the exponential relationship developed in this study as applied in the evergreen needle-leaved forest regions is not intended for use when LAI is beyond 1.5. When computing the transmissivity in woody savanna regions, the study suggests using winter LAI less than 0.8 during the regression analysis.

It is encouraging to witness a similar exponential relationship in both woody savanna and evergreen needle-leaved regions when colocated with different types of snow. It is also important to note that regions with different snow cover classifications and forest cover types should have different regression coefficients (i.e., a and b) as applied in Equation 4.14. Regression coefficients at either 18.7 GHz or 36.5 GHz at horizontal and vertical polarization were determined based on the mean values of a's and b's derived from all selected fitted exponential functions across the time period of investigation in both evergreen needle-leaved forest and woody

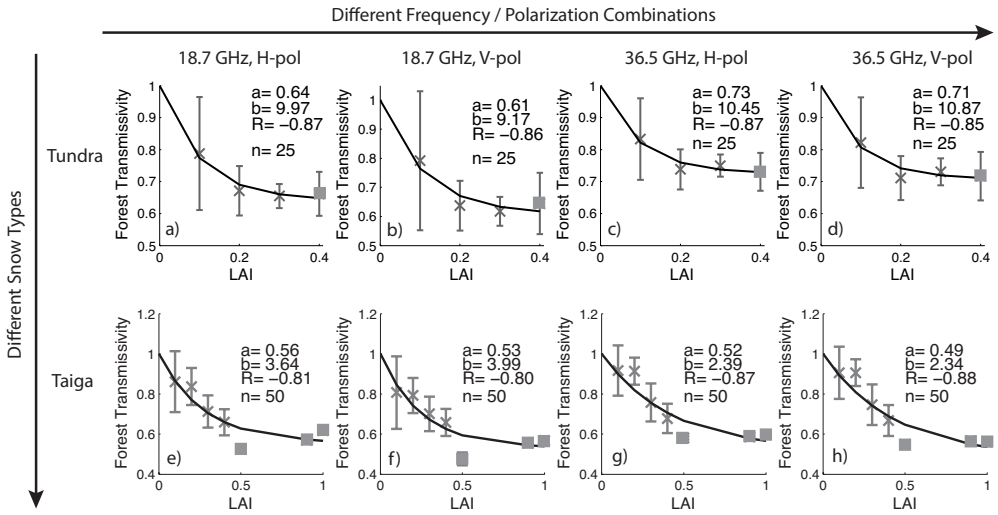

Figure 4.5: Relationship between LAI and forest transmissivity across woody savanna regions covered with tundra snow on 26 Feb 2003 (Figure 4.5a through Figure 4.5d) and regions covered with taiga snow on 10 Feb 2003 (Figure 4.5e through Figure 4.5h) , respectively. Each column represents different transmissivity estimates at different frequencies and polarizations. The 'x' marker is the mean transmissivity computed at each corresponding LAI bin while upper and lower grey bars indicate one standard deviation from the mean, respectively. The solid black line is the fitted exponential curve obtained from Equation 4.14 with regression coefficients a and b, n is the total sample size, and R is the correlation coefficient (see Appendix B for details). Forest transmissivity computed at undersampled LAI bins (i.e., with sample size less than 3) are marked as solid squares.

savanna regions (see Table 4.1). It is interesting to point out that the decay rate, b, is generally lower in the evergreen needle-leaved forest regions relative to those obtained from woody savanna areas colocated with taiga snow. That is, the rate of change in transmissivity with respect to LAI in woody savanna covered areas is generally higher than those obtained from evergreen needle-leaved forest covered regions during the winter. This phenomenon might be explained by the difference in volume scattering effects arising from forest structure and forest density differences.

Table 4.1: Forest transmissivity retrieval models with regression coefficients applied in Equation 4.14 for: top) evergreen needle-leaved forest covered regions colocated with taiga snow, and bottom) woody savanna regions colocated with taiga snow.

Snow and forest types	Microwave channel	Model parameter a	Model parameter b
Taiga snow + evergreen needle leaved forest	18H	0.89	1.94
	18V	0.88	2.63
	36H	0.82	1.42
	36V	0.85	1.74
Taiga snow + + woody savanna	18H	0.65	2.75
	18V	0.59	2.92
	36H	0.61	2.05
	36V	0.64	2.02

Volume scattering by canopies and leaves is relatively dominant for shorter wavelengths (i.e., 18.7 GHz and 36.5 GHz used here) as compared with L-band (∼1-2 GHz) in the microwave spectrum [146]. Discontinuous media (i.e., forest cover in the context) consisting of discrete elements (i.e., twigs, branches, leaves, and stems) will absorb, emit, or scatter radiation. Forest density and forest cover fraction are generally higher in evergreen needle-leaved areas (relative to woody savanna regions) based on the NASA forest product (i.e., MOD44B) [75]. A large number of small needle-shaped leaves are likely to behave as numerous small scatterers, and hence, these discontinuous media (i.e., evergreen needle-leaved forest) now behave like continuous media and the internal scattering becomes minimal as compared to more dominant radiation absorption processes [146]. Therefore, given the same magnitude of LAI, forest transmissivity computed in evergreen needle-leaved regions is generally higher than those in the woody savanna regions.

Prior to calculating decoupled snow Tbs using retrieved forest transmissivity in

Table 4.2: Comparisons of existing forest transmissivity retrieval models (selected).

Reference	Measurement type [1]	Structural parameter	Model formulation
Kruopis et al. (1999)	G	SV	t = a + (1-a) * exp(-b * SV)
Parde et al. (2005)	G	SV	t = a + (1-a) * exp(-b * SV)
Langlois et al. (2011)	A, G	SV	t = a + (1-a) * exp(-b * SV)
Roy et al. (2012)	A, G	SV	t = a + (1-a) * exp(-b * SV)
Roy et al. (2014)	S	MODIS LAI	t = a + (1-a) * exp(-b * LAI)
Vander Jagt et al. (2015)	A, S	MODIS LAI	t = a * exp(b * LAI) + c * exp(d * LAI)
This study	S	BNU LAI	t = a + (1-a) * exp(-b * LAI)

Section 4.4.2.2, it is important to first demonstrate the differences in transmissivity values retrieved from this study relative to other studies that used forest structural-related parameters. Since the majority of the existing transmissivity retrieval studies were conducted in areas covered with black spruce, which is a type of evergreen needle-leaved forest, coefficients shown in Table 4.1 are used for comparison.

The comparison of saturated transmissivity values (i.e., transmissivity for a very dense forest; see Figure 4.6) obtained from each model can not provide definitive proof of the rationality of coefficients for each retrieval approach since each model was evaluated based on different measurements colocated across a range of spatial scales (see Table 4.2). In a quantitative fashion, the study of Vander Jagt et al. (2015) [147] might underestimate forest transmissivity to some extent because the variance of air temperature was completely removed from the variance embedded in the Tb measurements. Furthermore, as discussed in Roy et al. (2014) [132], the

[1] A=Airborne, G=Ground-based, S=Space-based

transmissivity results from Kruopis et al. (1999) [133] might be underestimated at low LAI values. Therefore, transmissivity values presented in this study are generally higher than those presented in Vander Jagt et al. (2015) [147] and Kruopis et al. (1999) [133]. Such differences will only be reconciled once more coherent ground-based measurements below and above the canopy are available for scrutiny.

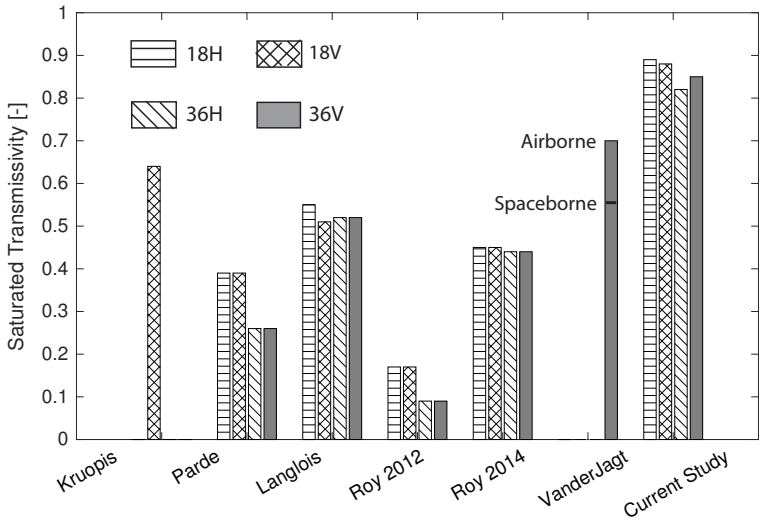

Figure 4.6: Comparisons of saturated transmissivity estimates obtained from existing studies (see Table 4.2). Results presented in Vander Jagt et al. (2015) [147] include two transmissivity values, namely, 0.70 for airborne-derived transmissivity and 0.58 for space-borne-derived transmissivity at 36V.

4.4.2.2 Non-SWE related Tb components in the measured PMW Tb

Regression coefficients used to estimate forest transmissivity across different land cover types and different snow types applied in Equation 4.8 should, if possible, consider all of the permutations between the two different sets of classes. Due to the dominance of evergreen needle-leaved forest in North America, this section

focused on the contributions of non-SWE related Tb components of the measured Tb arising from the atmosphere or from the vegetation with particular focus on evergreen needle-leaved forested areas, which during the snow season are typically colocated with taiga snow cover class. The sensitivity analysis of both model input states and model parameters are briefly discussed in the Appendix D.

Histograms are shown in Figure 4.7 in order to visualize the average amplitude of forest-decoupled Tb estimates at 18.7 GHz and 36.5 GHz using either horizontal or vertical polarization as a function of LAI. The vegetation-contributed component of Tb is defined as vegetation emission effects minus attenuation effects, and hence, it could be further written as "$Tb_{decouple-noatm,f} - Tb_{snow,f}$" (following the same nomenclature used in Equation 4.1). The magnitude of the vegetation-related component of measured Tb generally increases as LAI increases due to the increasing significance of vegetation emission relative to vegetation scattering. In addition, analysis across all available measurement dates suggests that the influence of vegetation is more pronounced at higher frequency and at horizontal polarization. The higher values of Tb contributions at horizontal polarization from vegetation could be partly explained by the dominant orientation of branches and coniferous needles in the evergreen needle-leaved forested regions as discussed in [133]. On the other hand, higher Tb contributions from vegetation at higher frequency could be explained by the fact that underlying surface (i.e., snow underlying the forest cover) has less influence on observed Tb at higher frequency due to a shorter PMW emission depth [111]. Further, histograms in Figure 4.7 help convey the average amplitude of forest-decoupled Tb estimates at 18.7 GHz or 36.5 GHz using either horizontal or

vertical polarization as a function of TPW. In accordance with conclusions drawn from Section 4.4.1, results here suggest that relatively large Tb impacts arising from the overlying atmosphere are present in Tb observations at 36.5 GHz at both horizontal and vertical polarizations. The atmospheric impacts on the measured Tb at 18.7 GHz are much less relative to 36.5 GHz, which is intuitive given greater transmissivity at a longer wavelength (i.e., lower frequency).

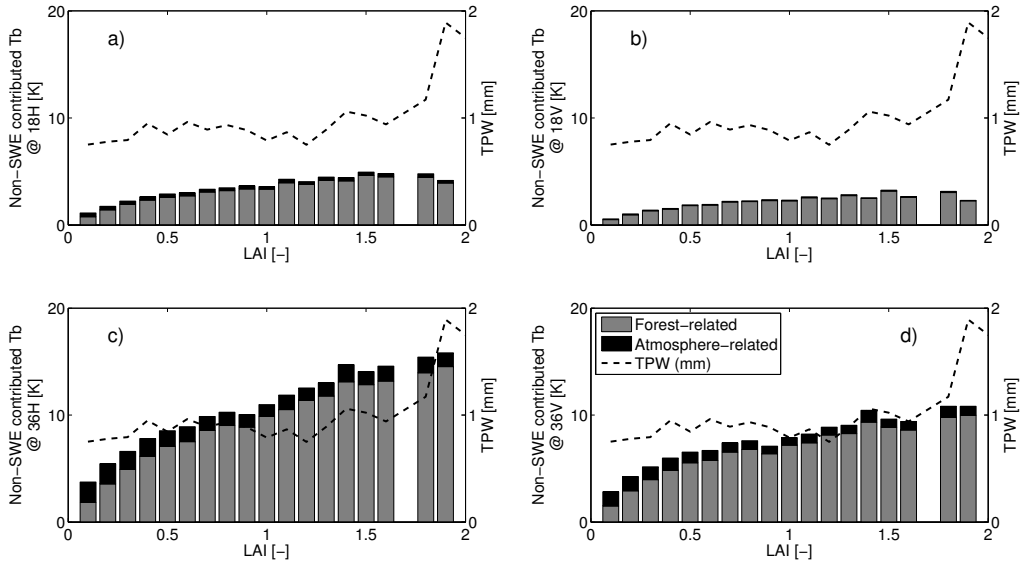

Figure 4.7: Histograms of area-averaged, non-SWE related Tb component in evergreen needle-leaved forest colocated with taiga snow cover on 06 Mar 2003. Atmospherically-contributed Tb information and forest-contributed Tb at 18H and 18V are shown in Figure 4.7a) and 4.7b), respectively. Forest contributed Tb at 36H and 36V are shown in Figure 4.7c) and 4.7d), respectively. Dashed lines indicate the mean total precipitable water content for the region of interest.

4.4.2.3 Impacts of Tb Decoupling on a Parsimonious SWE Retrieval

Equations shown in Section 4.3.1 suggest that shallow to moderate SWE (or snow depth) is proportional to computed ΔTb. To help illustrate this behavior, Figure 4.8 shows histograms of the average impacts to ΔTb due to the effects of forest emission and attenuation. In general, atmospheric adjustment (decoupling) of ΔTb increases as TPW increases. This argument holds true when TPW is relatively small as witnessed in both Figures 4.7 and 4.8 when the average TPW is less than 1.2 mm. However, when TPW exceeds a threshold, the overlying atmosphere behaves more like a "scatterer" of PMW radiation rather than an "emitter" as suggested by Equation 4.5, and hence, the atmospheric-related contribution to ΔTb decreases at relatively high TPW. This phenomenon is more pronounced at relatively high LAI values (i.e., LAI greater than 1.5) where an increase in TPW yields a decrease in the atmospheric component of Tb and ΔTb as shown in Figures 4.7 and 4.8, respectively. In addition, it can also be seen that the forest impacts on ΔTb increases with increasing LAI. The increase in the ΔTb at either horizontal or vertical polarization suggests that removal of vegetation information from the measured Tb would yield more SWE than by simply using the original AMSR-E Tb measurements directly.

Previous studies also provide us with some measure of vegetation (or non-SWE related) contributions to total Tb signals as measured with a PMW radiometer (see Table 4.3). It is clear from this study that the overall vegetation contribution (defined as emission effects minus attenuation) is generally less than values presented in other studies. This could be due, in part, to differences in measurement scales

used during evaluation, differences in forest transmissivity values, and differences in vegetation parameters (a.k.a., types or classes). When considering differences in measurement scales, study results concluded from Li and Kelly (2014) [148] are most comparable to this current study. Since no atmospheric decoupling procedure was applied in Li and Kelly (2014) [148], these results could overestimate the maximum amplitude of the Tb signal arising from the overlying vegetation only. With that said, it is encouraging to see that the vegetation-contributed Tb components computed from this study, in general, are lower than the values reported in [148] except for vertically-polarized Tb at 36.5 GHz. However, without ground-based measurements obtained from both above and below the canopy, it is difficult to tell exactly which model is indeed the most accurate measure of vegetation information given the mixed signal as measured by a spaceborne radiometer.

As stated previously, the evaluation of the forest decoupling procedure could also be made indirectly using snow depth and SWE information given the absence of both upward and downward radiometer observations below and above the canopy. Comparisons of SWE were first made between ground-based SWE measurements and SWE estimates (computed as a function of ΔTb) in evergreen needle-leaved forest regions colocated with taiga snow cover. Six different sets of SWE estimates (denoted as Exp.i to Exp.vi) were computed as a function of ΔTb using coupled AMSR-E Tb observations or decoupled Tb estimates as applied in Equations 4.11, 4.12 and 4.13 (see Figure 4.9a).

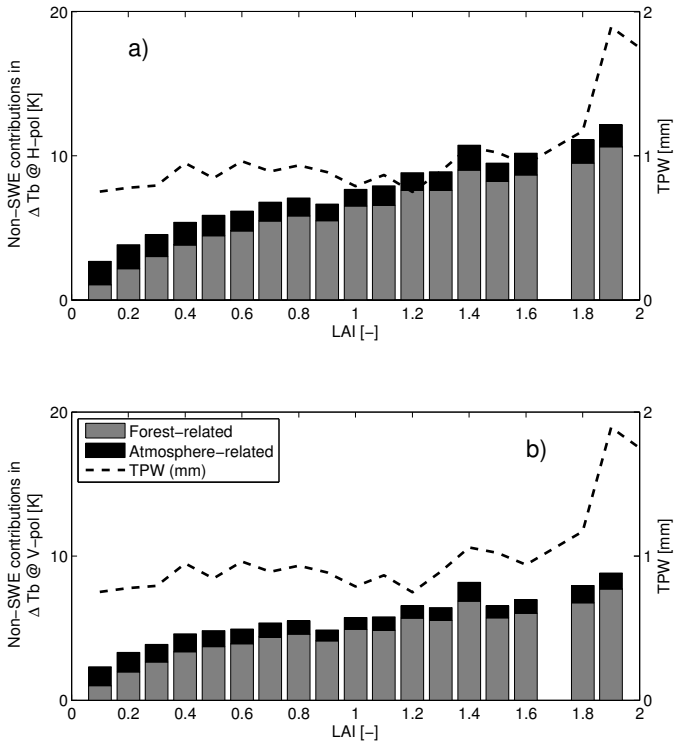

Figure 4.8: Histograms of area-averaged, non-SWE related ΔTb contributions in evergreen needle-leaved forest colocated with taiga snow cover on 06 Mar 2003. Average impacts of ΔTb at horizontal polarization ($\Delta Tb_H = Tb_{18H} - Tb_{36H}$) due to the forest decoupling procedure are shown as grey bars in Figure 4.8a). Average impacts of ΔTb_H due to atmospheric decoupling procedure are shown as black bars in Figure 4.8a). Figure 4.8b) is the same as Figure 4.8a) except for ΔTb at vertical polarization ($\Delta Tb_V = Tb_{18V} - Tb_{36V}$). Dashed lines show the mean total precipitable water content for the region of interest.

Table 4.3: Comparisons of forest contributions derived from the original, coupled PMW Tb observations.

Reference	Measurement type [1]	Study domain	Methodology	Vegetation Contribution to Tb
Langlois et al. (2011)	A, G	Quebec, Canada	Microwave transmissivity retrieval based on SV	27.4 K @ 18H (on average) 11.7 K @ 18V (on average) 24.2 K @ 36H (on average) 14.2 K @ 36V (on average)
Roy et al. (2012)	A, G	Quebec, Canada	Microwave transmissivity retrieval based on SV	125.1 K @ 18H 125.1 K @ 18V 138.8 K @ 36H 138.8 K @ 36V
Li and Kelly (2015)	S	Northern Hemisphere	Optical forest transmissivity [2] retrieval based on forest fraction as applied in PMW Tb regression	[-3.05 K, 26.95 K] @ 18H [-1.57 K, 8.00 K]@ 18V [-2.90 K, 31.07 K] @ 36H [-1.43 K, 13.42 K] @ 36V
This study	S	North America	Microwave transmissivity retrieval based on LAI as a function of snow snow cover type and forest type	[0 K, 9 K] @ 18H [0 K, 7 K]@ 18V [0 K, 21 K] @ 36H [0 K, 16 K] @ 36V [3]

[1] A=Airborne, G=Ground-based, S=Space-based

[2] wavelength ranges from 400 nm to 2500 nm

[3] "[ ]" stands for a closed interval. Data reported here were obtained from taiga snow class colocated with evergreen needle leaved forest regions

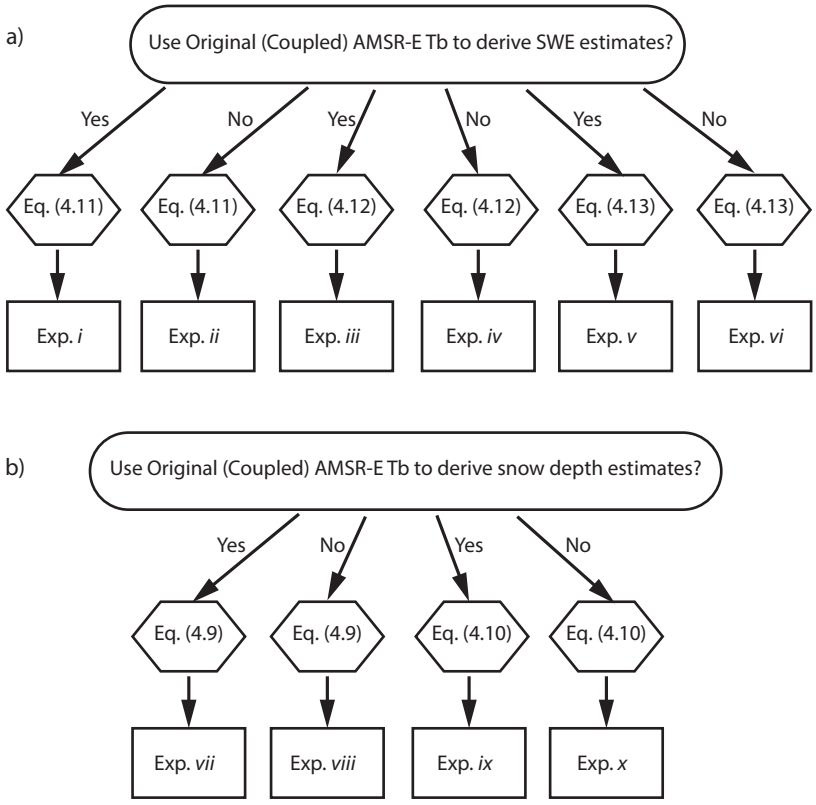

Figure 4.9: Experimental setup in a) SWE retrieval and b) snow depth retrieval as part of forest decoupling evaluation using Equations 4.9 through 4.13 (see Section 4.3.1). Retrievals computed with the original (coupled) AMSR-E Tb observations are denoted as "Yes" whereas results computed with the decoupled snow Tb estimates are denoted as "No". Different experiments are denoted as Exp.i to Exp.vi for the SWE retrieval results evaluation whereas Exp.vii to Exp.x are used to denote experiments conducted for the snow depth retrieval evaluation.

Using the closest (to the center of the EASE-Grid pixel) in-situ SNOTEL SWE measurements obtained from snow pillows as the "truth", goodness-of-fit statistics, including bias, RMSE, and unbiased RMSE were plotted in Figure 4.10, which were computed on 06 Mar 2003, 05 Mar 2004, 06 Mar 2005, 06 Mar 2006, and 06 Mar 2006, respectively. Early March is selected for each year as an example because the overlying snow pack, in general, is neither too wet nor too thin during

this time of the year for the domain used in this study. The SWE retrievals are generally more accurate during dry snow conditions (pre-ablation) with moderate snow depth relative to those during wet or thin snow conditions. It is encouraging to see that statistical metrics improve when implementing the two-step decoupling procedures no matter which of the three selected snow depth retrieval models is used. It is further worth noting that the use of the decoupled snow Tbs in the production of the SWE estimates using Equation 4.11 achieves a ∼55% reduction in bias, a ∼45% reduction in RMSE, and a ∼20% reduction in ubRMSE relative to that when using the original, coupled Tb observations. Even though relatively high ubRMSE were witnessed across all retrieval algorithms, they systematically improve the SWE estimates relative to the independent SNOTEL SWE observations and suggest viability in the proposed approach.

Similar to SWE estimate comparisons using decoupled and coupled Tb observations, respectively, comparisons of snow depth were conducted using ground-based snow depth measurements and snow depth estimates across evergreen needle-leaved forest region colocated with taiga snow cover during the month of March for the years 2004 to 2009. Four different sets of snow depth estimates (denoted as Exp.vii to Exp.x) were computed as a function of ΔTb using coupled AMSR-E Tb observations or decoupled Tb estimates as applied in Equations 4.9 and 4.10 (see Figure 4.10b).

In a similar manner as conducted previously with SNOTEL SWE observations, the in-situ GSOD snow depth measurements were used as the "truth". The resulting goodness-of-fitness statistics (i.e., bias, RMSE, and ubRMSE) are shown

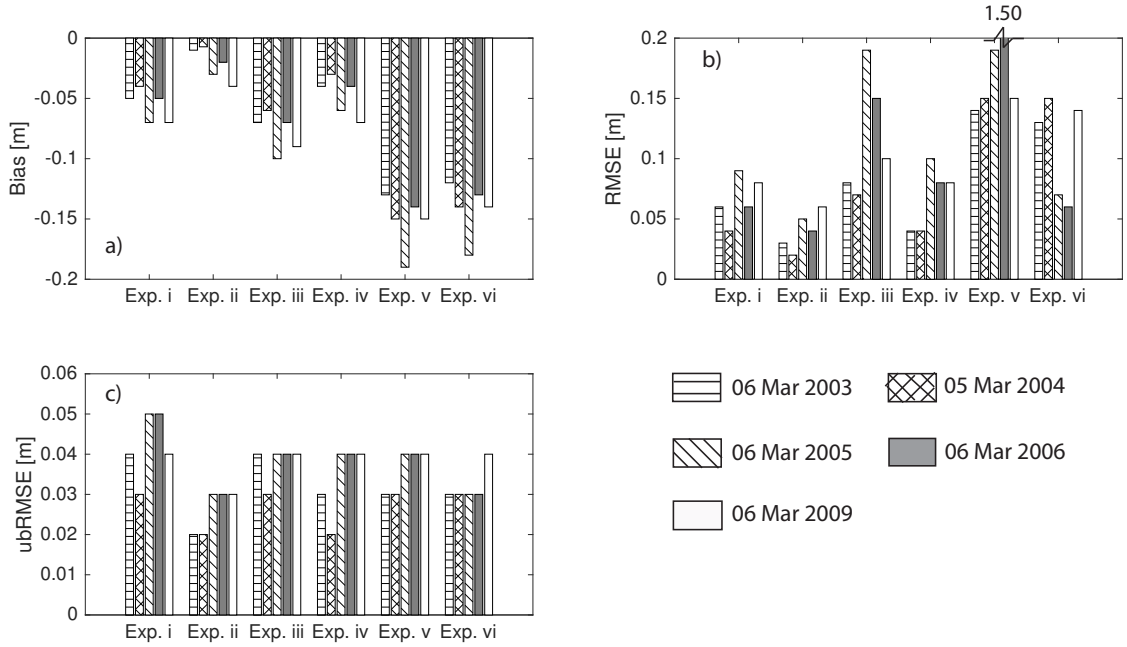

Figure 4.10: Statistical comparisons for a) bias, b) RMSE, and c) ubRMSE for SWE estimates compared against SNOTEL observations on 06 March 2003, 05 March 2004, 06 March 2005, 06 March 2006 and 06 Mar 2009 over evergreen needle-leaved forest covered regions (0<LAI<1.5) colocated with taiga snow cover. Labels along the x-axis indicate which experiment in Figure 4.10 was used in the SWE comparisons and the experiment setup as described in Section 4.3.1.

in Table 4.4. It is interesting to note that snow depth retrieval using Equation 4.10 often yields relatively large positive biases when compared with in-situ observations. The statistics for snow depth degrade when using decoupled Tbs relative to snow depth estimates using the original, coupled Tb information. Positive biases could be related to uncertainty in the forest fraction product or uncertainty in the calibration coefficients (a.k.a., model structure error) used in Equation 4.9 that are dependent on snow cover class, forest cover type, snow grain size, snow density, and other snow microphysical parameters. The estimation uncertainty related to the retrieval model

parameterization tends to increase as forest density increases [141]. In addition, it is encouraging to see that statistical metrics improve with the two-step decoupling procedure when applied to Equation 4.9. The use of the decoupled snow Tbs to estimate snow depth yields more accurate estimates and achieves a ∼60% reduction in bias, a ∼12% reduction in RMSE, and a ∼5% reduction in ubRMSE relative to estimates based on the original, coupled Tb observations. However, it should be clearly stated that high values of RMSE and ubRMSE values suggest random errors in the snow depth retrievals exist in appreciable quantities (with or without application of the decoupling procedures) and should be further investigated in a follow-up study.

4.5 Conclusions and Implications

A complete and accurate estimation of the relationship between snow mass and the passive microwave electromagnetic response of that snow mass remains elusive, especially in densely-forested areas. The nature of the close-to-random spatial distribution of tree branches and the dynamics of forest cover evolution is one significant limitation in the accuracy of SWE retrievals relying on satellite or airborne-based passive microwave observations. In order to isolate the non-SWE related Tb information content associated with atmospheric and vegetative effects, it is worthwhile adopting a two-step decoupling procedure before using PMW Tb observations in SWE retrievals or SWE-centric Tb assimilation studies.

The first decoupling procedure removes atmospheric-related Tb information

Table 4.4: Statistical comparisons of estimated snow depth against GSOD observations in evergreen needle-leaved forest covered regions (0<LAI<1.5) colocated with taiga snow class. Snow depth retrieval models with the best statistical metrics (i.e., lowest absolute values of bias, RMSE, and ubRMSE) are bolded.

Date and year	Retrieval method	Bias [m]	RMSE [m]	ubRMSE [m]	Use original (coupled) AMSR-E Tb?	Exp. number	Average forest cover fraction
05 Mar	Eq. 4.9	-0.04	0.12	0.11	Yes	Exp.vii	75.52%
Mar	**Eq. 4.9**	**0.02**	**0.10**	**0.10**	**No**	Exp.viii	
2004	Eq. 4.10	9.43	25.21	23.38	Yes	Exp.ix	
	Eq. 4.10	12.88	35.38	32.95	No	Exp.x	
06	Eq. 4.9	-0.21	0.28	0.19	Yes	Exp.vii	74.87%
Mar	**Eq. 4.9**	**-0.18**	**0.26**	**0.18**	**No**	Exp.viii	
2005	Eq. 4.10	1.37	3.11	2.79	Yes	Exp.ix	
	Eq. 4.10	1.61	3.72	3.35	No	Exp.x	
14	Eq. 4.9	-0.05	0.28	0.19	Yes	Exp.vii	76.02%
Mar	**Eq. 4.9**	**0.01**	**0.26**	**0.18**	**No**	Exp.viii	
2006	Eq. 4.10	5.40	3.11	2.79	Yes	Exp.ix	
	Eq. 4.10	7.33	3.72	3.35	No	Exp.x	
06	Eq. 4.9	-0.12	0.19	0.18	Yes	Exp.vii	70.61%
Mar	**Eq. 4.9**	**-0.07**	**0.18**	**0.18**	**No**	Exp.viii	
2007	Eq. 4.10	5.62	15.78	14.83	Yes	Exp.ix	
	Eq. 4.10	7.15	22.24	21.00	No	Exp.x	
05	Eq. 4.9	-0.04	0.20	0.20	Yes	Exp.vii	76.05%
Mar	**Eq. 4.9**	**0.01**	**0.19**	**0.19**	**No**	Exp.viii	
2008	Eq. 4.10	8.23	23.85	22.39	Yes	Exp.ix	
	Eq. 4.10	10.14	30.04	28.27	No	Exp.x	
06	Eq. 4.9	-0.14	0.33	0.30	Yes	Exp.vii	77.96%
Mar	**Eq. 4.9**	**-0.09**	**0.30**	**0.29**	**No**	Exp.viii	
2009	Eq. 4.10	8.28	22.00	20.38	Yes	Exp.ix	
	Eq. 4.10	10.63	28.65	26.61	No	Exp.x	

based on empirical functions and a dynamic estimate of TPW content as estimated by NASA's MERRA product. The results demonstrate that atmospherically-contributed Tb ranges from 1 K to 3 K and depends on the frequency, polarization, and the meteorologic conditions at the time of AMSR-E overpass. The second decoupling procedure to remove the vegetation-related signal employs a MODIS-derived LAI product to first compute forest transmissivity prior to computing radiance emission directly from the underlying snow. The fitted exponential functions are shown to be effective during forest decoupling for evergreen needle-leaved forest and woody savanna regions, but remain uncertain in other forest types due to undersampled LAI information colocated with snow cover. In an analogous fashion as for the atmospheric component, removal of the forest-related Tb information content from the original observations caused ΔTb to increase, which helps ameliorate some of the negative bias typically found in SWE retrievals in densely-forested areas [18,26]. Comparisons were made indirectly between snow depth and SWE retrieval algorithms as well as independent ground-based observations from the GSOD and the SNOTEL networks, respectively. When using the decoupled PMW Tb estimates (relative to using the original AMSR-E Tb observations), snow depth bias is reduced by 60% and SWE bias is reduced by 55%. However, computed RMSE and ubRMSE values suggest random errors in the snow depth retrievals (with or without application of the decoupling procedures) is significant and remains an issue for further study.

It is anticipated that regional SWE estimation could be eventually improved with the help of the proposed two-step decoupling procedure across thinly- to

heavily-vegetated regions within a Tb data assimilation framework. It is further believed that accurate SWE information could be used by water resources managers in the future towards making better decisions in their water management practice and water supply forecasting activities such as reservoir regulation, downstream flood prediction, agricultural water management, and climate variability studies.

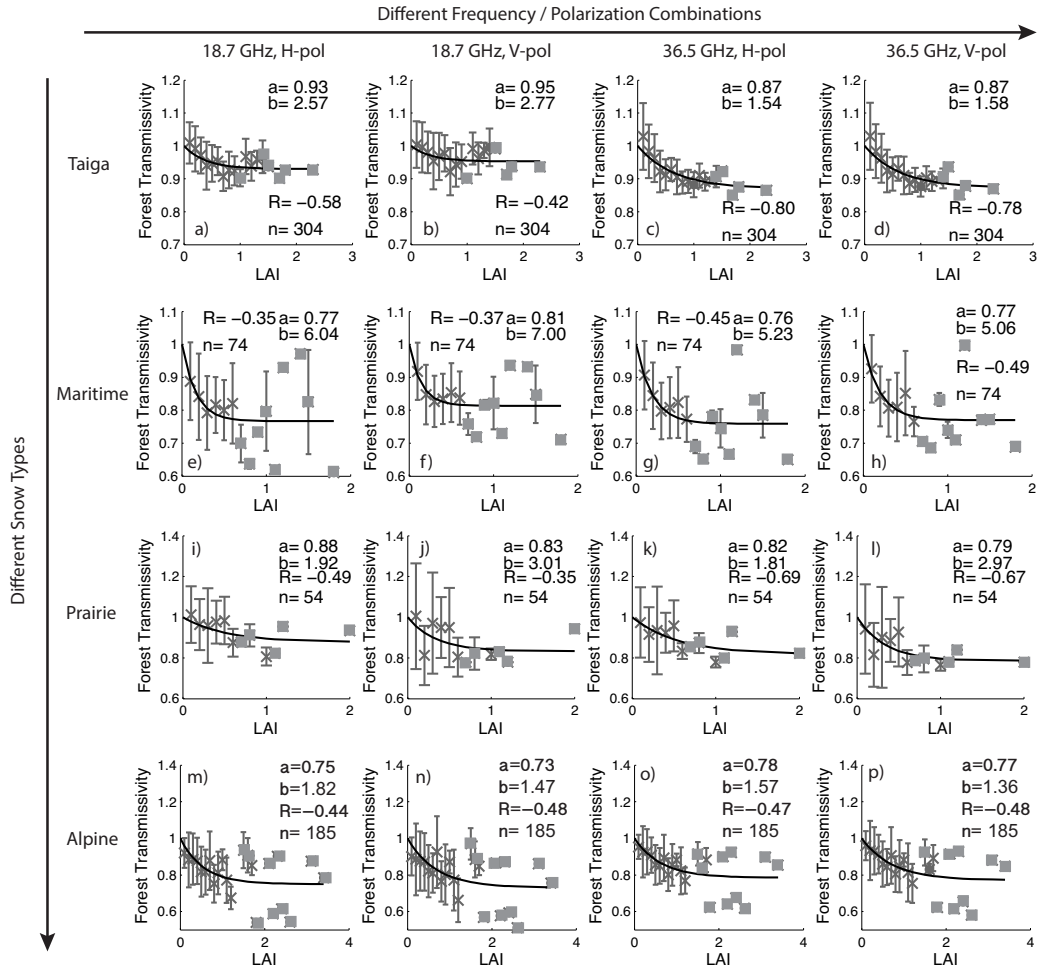

Figure 4.11: Same as Figure 4.5 but for evergreen needle-leaved forest. Figures 4.11a) through 4.11d) represent taiga snow regions on 06 Mar 2003. Figures 4.11e) through 4.11h) represent maritime snow regions on 01 Jan 2006. Figures 4.11i) through 4.11l) represent prairie snow conditions on 10 Feb 2003. Figures 4.11m) through 4.11p) represent alpine snow conditions on 17 Jan 2005.

Chapter 5: Integration of satellite-based decoupled passive microwave brightness temperatures and an ensemble-based land data assimilation framework in order to improve snow estimation in forested regions

5.1 Motivation and Objective

Chapter 3 demonstrated that the assimilation of original spectral difference of brightness temperature (Tb) observations (ΔTb) is advantageous at characterizing regional snow water equivalent (SWE) and snow depth information along with a well-trained support vector machine (SVM). However, relatively small improvements (sometimes degraded performance) of the data assimilation (DA) system was witnessed at places covered with significant amount of forest over snow-covered land in Alaska. It is therefore postulated in Chapter 3 that the non-SWE related components of the measured Tb observations should be removed prior to SVM training and predicting procedure. In addition, previous study [149] showed that modeling atmospheric and forest related emissions are helpful towards snow depth estimation from December 2002 to February 2003 in North America within a radiance assimilation framework while using a physically-based radiative transfer model as

the model operator. Therefore, this chapter is intended to address the question: "Can spatially-distributed SWE and snow depth estimates be enhanced through the integration of a SVM in conjunction with atmospheric-and-forest decoupled Tb observations into a land surface model? The research presented here will be published in IEEE International Geoscience and Remote Sensing Symposium.

5.2 Methodology

5.2.1 Land surface model and study area

The NASA Goddard Earth Observing System Model, Version 5 (GEOS-5) Catchment Land Surface Model (Catchment) [70] was used as the forward model. Meteorological fields from the Modern-Era Retrospective analysis for Research and Applications (MERRA) product were used to define the meteorological boundary conditions. Relevant snow states derived from Catchment include three-layer snow depth, SWE, snow density, snow temperature, and snow liquid water content. Previous studies showed that both SWE and snow depth estimates via Catchment were relatively unbiased (i.e., bias of snow depth $\approx$ -1 cm; bias of SWE $\approx$ -1.2 cm) and contain reasonable amount of random errors and uncertainty (i.e., root mean squared error (RMSE) of snow depth $\approx$ 20 cm; RMSE of SWE $\approx$ 9.5 cm) [7]. In addition, a comparison of daily-averaged, near-surface soil temperature (in the presence of snow cover) suggests Catchment output was unbiased relative to ground-based observations from the Snow Telemetry (SNOTEL) network located in the western continental United States and Alaska. The unbiasedness property of each Catchment-derived

estimate is critical in the machine-learning-based model formulation introduced in the Section 5.2.3, especially with regards to SWE since SWE is the focus of the ΔTb assimilation framework.

Catchment was run at a time increment of 450 seconds from 01 August 2002 to 30 June 2011 on the 25-km Equal Area Scalable Earth (EASE) grid in Quebec and Newfoundland, Canada, and several pixels (with colocated ground-based stations) in North America covered with evergreen needle-leaved forest cover and taiga snow cover (see Figure 5.7). The employment of the two elevation products is intended to minimize the effect of elevation discrepancy between the ground-based stations and the colocated grids (see Section 5.3.2.1 for details). In addition, the domain of Quebec and Newfoundland, Canada is selected because: 1) there is a variety of vegetated and non-vegetated land colocated with seasonal snow, and 2) the region receives the second largest maxima in snow accumulation (after the western cordillera) across North America [150]. Quantification of SWE is of vital importance to this region, and it is estimated that 1 mm of SWE in the headwaters in Quebec is equivalent to $1M hydro-electric power production [150].

The uncertainty of the input forcings to the Catchment forward model was modeled by perturbing precipitation, incoming solar (shortwave) radiation, and incoming longwave radiation within the ensemble-based assimilation system (see Section 5.2.3 for details) in order to adequately represent model errors. The perturbation parameters were the same as used in Chapter 3, which were shown consistent with other published recommendations [49, 101, 108, 151].

Table 5.1: Open-loop (OL) and data assimilation experiment (DA_O, DA_A, DA_{A+F}) configurations.

Case ID	Description
OL	Without assimilation
DA_O	Assimilating original (i.e., coupled) AMSR-E ΔTb observations
DA_A	Assimilating atmospherically-decoupled AMSR-E ΔTb observations
DA_{A+F}	Assimilating atmospheric-and-forest-decoupled AMSR-E ΔTb observations

5.2.2 Observations and experiments setup

Passive microwave (PMW) Tb observations at three different frequencies — 10.65, 18.7, and 36.5 GHz — at both horizontal and vertical polarization were used for assimilation. These Tb observations were acquired by the Advanced Microwave Scanning Radiometer (AMSR-E) and subsequently gridded to a 25-km EASE grid from 01 June 2002 to 01 July 2011. Only measurements from the nighttime (approximately 01:00 to 01:30 hour local time) overpass were used in order to minimize wet snow effects.

Similar to the joint-assimilation framework of spectral difference (ΔTb) combinations described in Chapter 3, a set of experiments were conducted to assess the model performance in both SWE and snow depth estimation (see Table 5.1). The OL experiment, and the DA_O experiment setup has been discussed in Chapter 3. In DA_A and DA_{A+F} experiments, four ΔTb combinations were used, which could

be expressed as:

$$\begin{aligned}
\Delta Tb'_{10H-36H} &= Tb_{10H} - Tb'_{36H} \\
\Delta Tb'_{10V-36V} &= Tb_{10V} - Tb'_{36V} \\
\Delta Tb'_{18H-36H} &= Tb'_{18H} - Tb'_{36H} \\
\Delta Tb'_{18V-36V} &= Tb'_{18V} - Tb'_{36V}
\end{aligned} \tag{5.1}$$

where Tb_{10H} is the AMSR-E based Tb observations of 10.65 GHz at horizontal polarization, Tb'_{36H} is the decoupled Tb (either atmospherically-decoupled or atmospheric-plus-forest decoupled) observations of 36.5 GHz at horizontal polarization, Tb_{10V} is the AMSR-E based Tb observations of 10.65 GHz at vertical polarization, Tb'_{36V} is the decoupled (either atmospherically-decoupled or atmospheric-plus-forest decoupled) Tb observations of 36.5 GHz at vertical polarization, Tb'_{18H} is the decoupled (either atmospherically-decoupled or atmospheric-plus-forest decoupled) Tb observations of 18.7 GHz at horizontal polarization, Tb'_{18V} is the decoupled (either atmospherically-decoupled or atmospheric-plus-forest decoupled) Tb observations of 18.7 GHz at vertical polarization.

5.2.3 The one-dimensional Ensemble Kalman filter

The measurement model used in this study is a SVM-based model. That is, the SVM-based model was employed to estimate original, and decoupled satellite-based PMW ΔTb observations at multiple frequency / polarization combinations given land surface and near-surface state variable information from Catchment. Four input states were ultimately selected during the SVM training procedure based on

the sensitivity analysis described in Chapter 2, namely, SWE, top-layer snow temperature, top-layer soil temperature and snow liquid water content. Each SVM for each 25-km EASE grid was trained for a 2-week (fortnight) period. A temporal overlap of 2 weeks was included at the beginning and at the end of each training period to address the strong seasonality in snow processes [60]. Different DA experiments have different training output. That is, in DA_O experiments, training outputs are original (i.e, coupled) ΔTb observations. In DA_A experiments, training outputs are atmospherically-decoupled ΔTb predictions. In DA_{A+F} experiments, training outputs are atmospheric-and-forest decoupled ΔTb predictions. That is, in DA_{A+F} experiments, forest transmissivity models as applied to pixels covered with either evergreen needle-leaved forest or woody savanna colocated with taiga snow cover type were employed to remove forest-related components on top of the atmospherically-decoupled observations.

An ensemble size of 32 was used here based on the convergence of both OL-derived and DA-derived SWE ensemble mean, and the ensemble spread. In both DA_A and DA_{A+F} experiments, the prior model state is updated using the observations available for the day of interest for a single computational unit at which point the linear update equation is applied as:

$$x_t^{i+} = x_t^{i-} + \mathbf{K}_t[(\mathbf{y}_t + \mathbf{v}^i) - \mathbf{\Phi}_t(x_t^{i-})] \tag{5.2}$$

where i represents a single replicate from the ensemble at time t, x_t^{i-} is the prior estimate of the state obtained from Catchment, $\mathbf{K}_t$ is the Kalman gain matrix, $\mathbf{y}_t$ is the decoupled ΔTb measurement vector, and $\mathbf{\Phi}_t(\cdot)$ is the predicted measurement

model (i.e., trained SVM) that non-linearly maps the model states into decoupled radiance measurement space. Random perturbations, $\mathbf{v}^i$, representing frequency / polarization-independent, and time-invariant measurement errors are added to the measurement vector [68]. The measurement error is approximated as a Gaussian-distributed variable with a mean of zero and a standard deviation of σ. $\sigma = 2$ K is selected for DA_O experiment across all four ΔTb channels based on the discussions in Chapter 3. $\sigma = 3$ K is selected for both DA_A and DA_{A+F} experiments across all four ΔTb channels in order to account for additional uncertainty introduced to the decoupled ΔTb observation due to the use of ancillary information related to total precipitable water, forest cover fraction, and/or LAI products.

The transfer of information from the radiance observations into the updated state vector is achieved through the Kalman gain (with the subscript t omitted for clarity), $\mathbf{K}$, which is effectively a weighted average between the uncertainty of the prior (model) state variables and the decoupled observations such that

$$\mathbf{K} = \mathbf{C}_{xy} \left(\mathbf{C}_{yy} + \mathbf{C}_{vv} \right)^{-1}, \tag{5.3}$$

where $\mathbf{C}_{xy}$ is the error cross-covariance between the prior states and the predicted measurements, $\mathbf{C}_{yy}$ is the error covariance of the predicted measurements, and $\mathbf{C}_{vv}$ is the measurement error covariance.

There are cases when no update within a DA framework (i.e., model-only results) would take place, for example in non-land grids (i.e., contain water bodies or land ice). Non-land grids are excluded in order to minimize the effects of PMW Tb emissions from water bodies or land ice. The masking procedure is common in many

satellite-based SWE retrieval product [16]. Further, land grids affected by relatively significant radio-frequency interference (RFI) at 10.65 GHz are also included from update [152]. When the occurrence of negative ΔTb computed between 6.9 GHz and 10.65 GHz (i.e., less than -10 K) is greater than 20% of the entire times series, the grid is excluded from having update.

5.2.4 Evaluation metrics and methods

Both OL and DA-derived results were compared against (1) available snow products, and (2) in-situ snow observations. The three available snow products are the European Space Agency (ESA) Global Snow Monitoring for Climate Research (GlobSnow) SWE version 2.0 product [10, 52], the Canadian Meteorological Centre (CMC) Daily Snow Depth product [104, 105], and the AMSR-E/Aqua L3 Global SWE version 2 product [106]. The ground-based snow observations are obtained from the U.S. National Climatic Data Center Global Summary of the Day (GSOD) product. It is also worth noting that CMC snow depth product is not used to compare against GSOD observations since GSOD observations were "assimilated" as part of the CMC reanalysis product, which tends to violate the independence between the estimates and observations used during evaluation. In addition, ground-based runoff observations (e.g., Global Runoff Data Base) are not available in the region of interest here.

Statistical metrics including bias, root mean squared error (RMSE), and normalized information contribution (NIC) (see Appendix B for details) were computed

to evaluate model-derived estimates against the closest ground-based, in-situ stations.

5.3 Results and discussions

5.3.1 Compare against state-of-the-art snow products

Figure 5.1 shows the SWE estimates obtained from GlobSnow, AMSR-E SWE products, OL experiments, and various DA experiments on four example days in the water year 2002. Similarly, Figure 5.2 shows the snow depth estimates obtained from CMC snow depth product, OL experiments and various DA experiments on the same days as shown in Figure 5.1. The four example dates of 19 Oct 2002, 16 Dec 2002, 13 March 2003, and 12 Apr 2003 highlight a typical snow pack accumulation and ablation process. It is found there is a significant pattern mismatch between different snow products, especially during early snow accumulation phase. This might be due to the highly variable snow conditions in Quebec, Canada complicated by dense forest cover and significant lake effects. In general, AMSR-E SWE products overestimate SWE for several pixels in northern Quebec on 16 Dec 2002, but underestimate SWE across the entire snow season. In places covered with relatively thin forest and small amount of lakes (i.e., between 50 °N to 55 °N and 55 °W to 60 °W), it is encouraging to see that all three DA experiments tend to yield estimates moving towards GlobSnow SWE estimates (relative to OL-derived SWE) on 16 Dec 2002. In addition, all three DA experiments tend to yield estimates moving towards CMC snow depth estimates (relative to OL-derived snow depth) on 13 Mar 2003. How-

ever, there are no ground-based GSOD stations within this area to further compare against.

5.3.2 Compare against ground-based snow observations

5.3.2.1 Effects of atmospheric decoupling

To minimize the effect of representativeness errors in model evaluation, pixels (16 out of 32) significantly affected by the elevation discrepancies were removed from comparison. The absolute relative elevation difference, ΔH, is computed as:

$$\Delta H = \frac{|H_{in-situ} - H_{grid}|}{H_{in-situ}} \tag{5.4}$$

where $|\cdot|$ denotes the absolute value of the expression, $H_{in-situ}$ is the elevation of the in-situ station, and H_{grid} is the elevation of the colocated grid obtained from either Catchment model or the aggregated Global Land One-km Base Elevation Project (GLOBE). For each grid, both elevation products were used in the ΔH computation. If the computed ΔH derived from any of the two products is greater than 150% , the pixel is determined to be affected by relatively significant elevation discrepancies, and hence, were removed from the model evaluation procedure. In addition, six pixels with GSOD stations having less-than-two-year of observations were removed from comparison. Eight pixels significantly affected by water bodies were removed from the goodness-of-fit statistics computation. Therefore, only two GSOD stations shown in Figure 5.7e) were available to compare against.

The time series of model-derived snow depth estimates, and GSOD observations for the grid #1, and grid #2 (see Figure 5.7e)) were shown in Figure 5.3a),

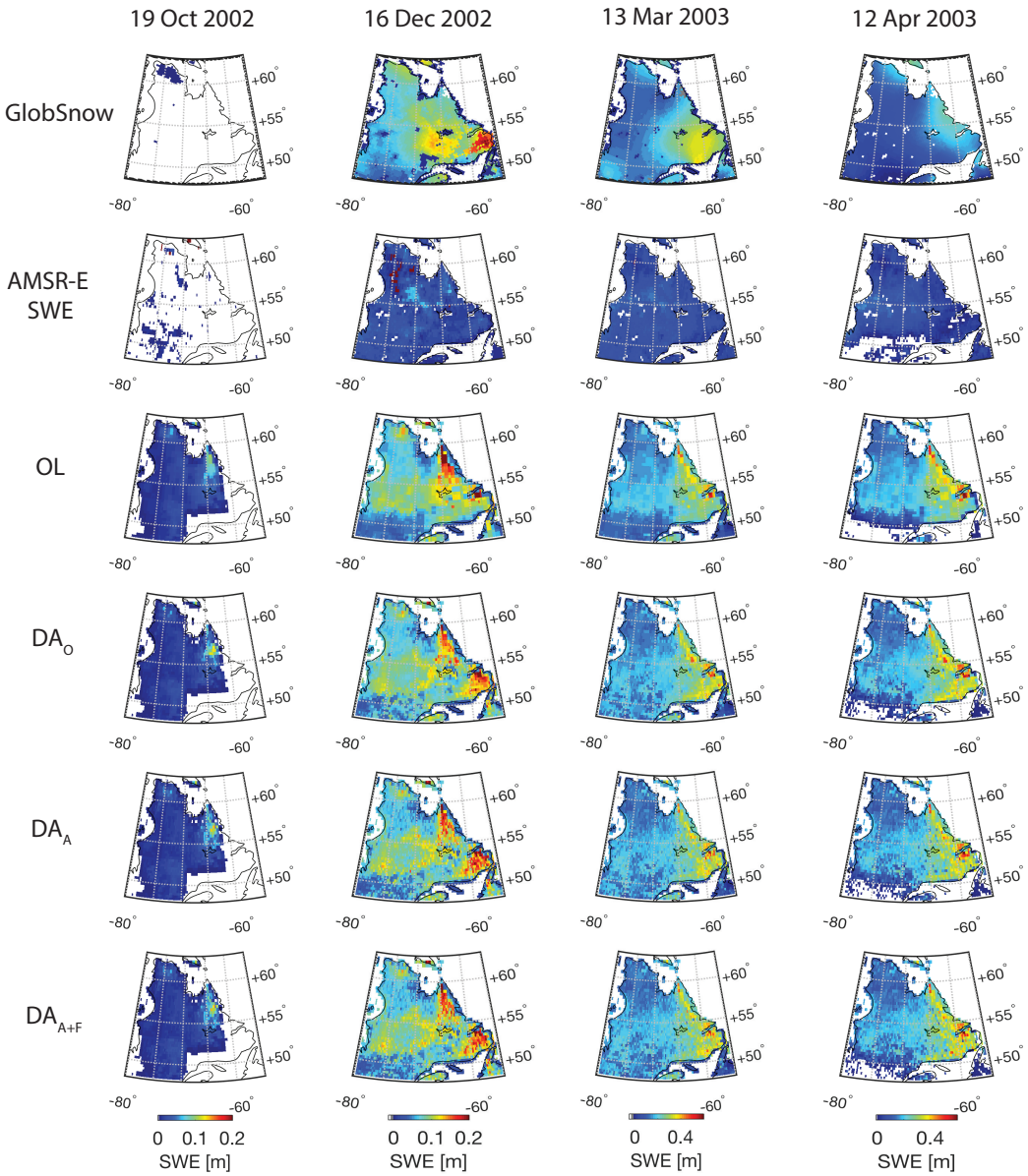

Figure 5.1: SWE estimates obtained from a) top row: ESA GlobSnow product, b) second row: AMSR-E SWE product, c) third row: OL experiments, d) fourth row: DA$_O$ experiments, e) fifth row: DA$_A$ experiments, and f) sixth row: DA$_{A+F}$ experiments. Each column represents SWE estimates obtained at 19 Oct 2002 (left column), 16 Dec 2002 (second column), 13 Mar 2003 (third column), and 12 Apr 2003 (fourth column), respectively.

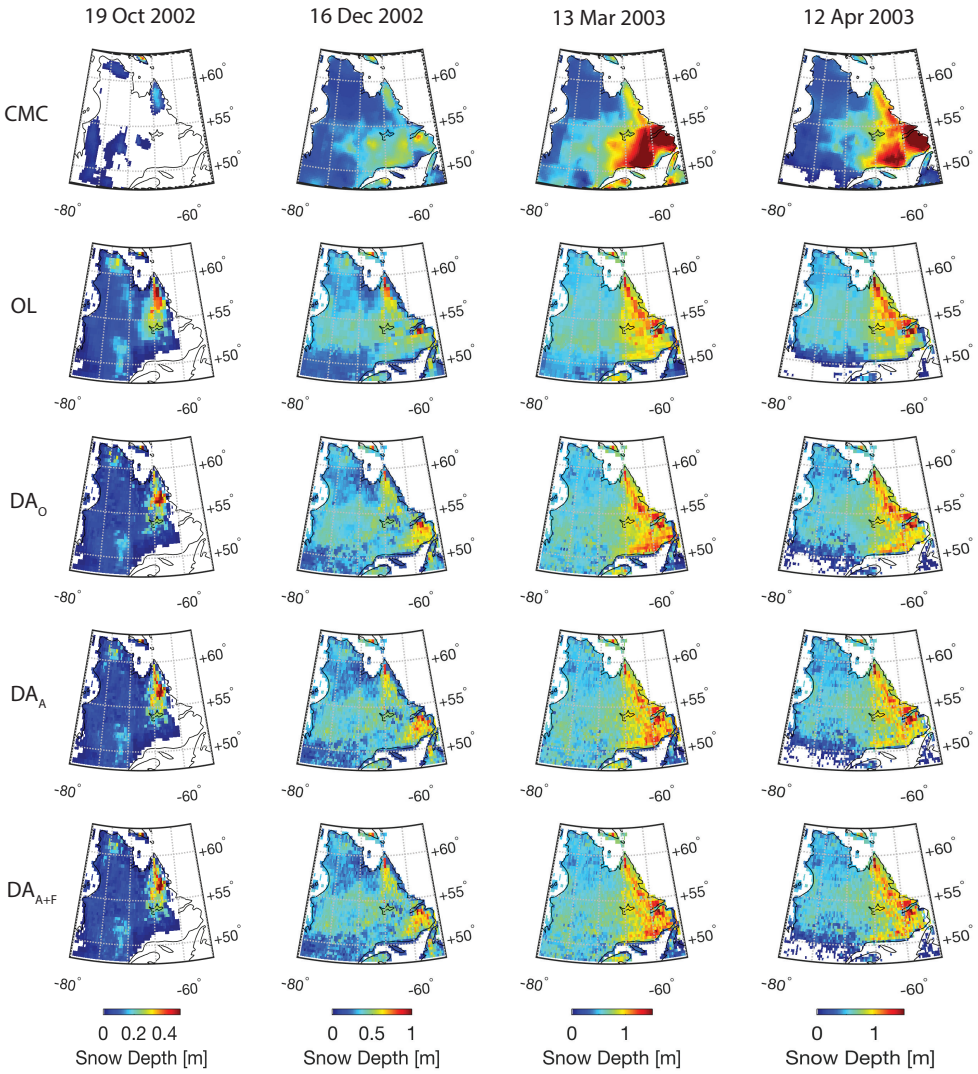

Figure 5.2: Snow depth estimates obtained from a) top row: CMC product, b) second row: OL experiments, c) third row: DA_O experiments, d) fourth row: DA_A experiments, and e) fifth row: DA_{A+F} experiments. Each column represents snow depth estimates obtained at 19 Oct 2002 (left column), 16 Dec 2002 (second column), 13 Mar 2003 (third column), and 12 Apr 2003 (fourth column), respectively.

and b), respectively. At grid #1, bias was reduced by ∼30% (from 0.23 m to 0.16 m), and the RMSE was reduced by ∼24% (0.26 m to 0.19 m) from OL to DA_O experiment. After including the atmospheric-decoupling procedure in the assimilated ΔTb, bias was reduced by ∼41%, and the RMSE was reduced by ∼36% from OL to DA_A experiment. At grid #2, bias was slightly degraded from OL to DA_O experiment. The computed RMSE remained unchanged from OL to DA_O experiment. The computed bias remained unchanged from OL to DA_A experiment. However, RMSE was reduced by ∼8% from OL to DA_A experiment. The relatively good performance of the DA_A experiment was also witnessed in the NIC computations as shown in Figure 5.5 for the two locations. Positive NICs computed from DA_A experiment suggests that including the atmospheric decoupling procedure prior to implementing DA might be advantageous at removing part of the non-snow related signals from the observations.

5.3.2.2 Effects of atmospheric-and-forest decoupling

In order to analyze the DA performance coupled with the forest transmissivity model as applied for evergreen needle-leaved forest colocated with taiga snow cover, eight grids (see Figure 5.7g)) having forest cover fraction greater than 85% in North America with colocated GSOD stations were selected in the comparison from 2002 to 2011. The use of ancillary forest cover fraction product here is to increase the possibility that ground-based stations could roughly represent the vegetation condition in the colocated EASE Grids, and hence, minimizing the representativeness

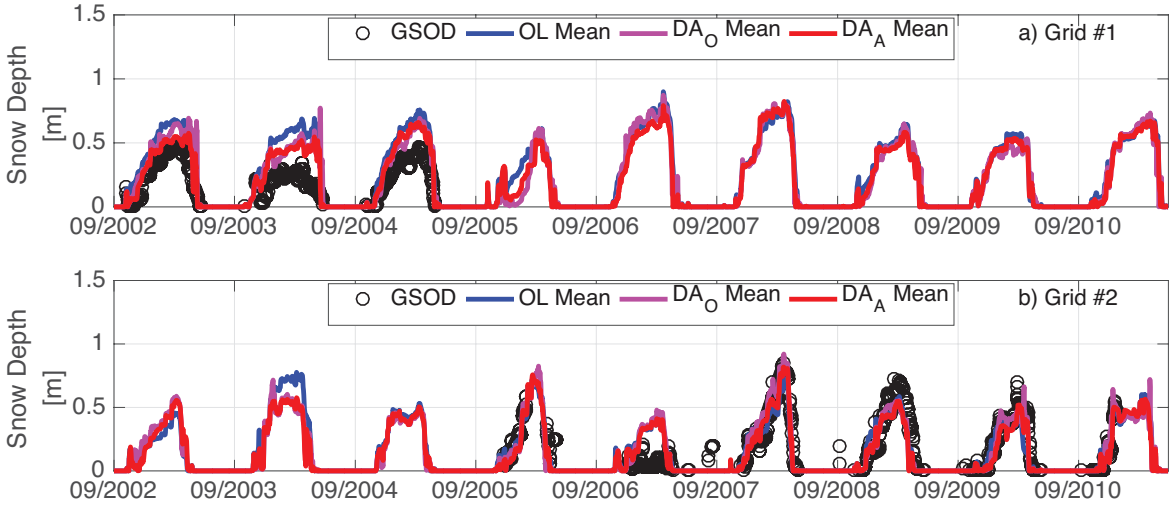

Figure 5.3: Times series of model-derived (including OL experiment, DA_O experiment, and DA_A experiment) snow depth estimates, and colocated ground-based GSOD observations in Quebec and Newfoundland, Canada from 2002 to 2011. Figure 5.3a) is for grid #1 in Figure 5.7e) at (53.69°N, 73.67°W), and Figure 5.3b) is for grid #2 in Figure 5.7e) at (48.71°N, 72.62°W).

errors arising from sub-grid scale variability with respect to vegetation conditions. Similar to Section 5.3.2.1, both GLOBE elevation product and Catchment elevation were employed to screen out pixels with relatively significant elevation discrepancies (i.e., $\Delta H > 150\%$) prior to the evaluation procedure.

The histograms of computed average bias and RMSE were shown in Figure 5.6. DA_O-derived snow depth estimates slightly degraded OL-derived estimates in both bias, and RMSE statistics computation. On the other hand, DA_{A+F}-derived estimates decreased the RMSE by ~5% relative to OL-derived estimates. The computed bias remained unchanged from OL to DA_{A+F} experiment. The relatively good performance of the DA_{A+F} experiment was also witnessed in the NIC computations

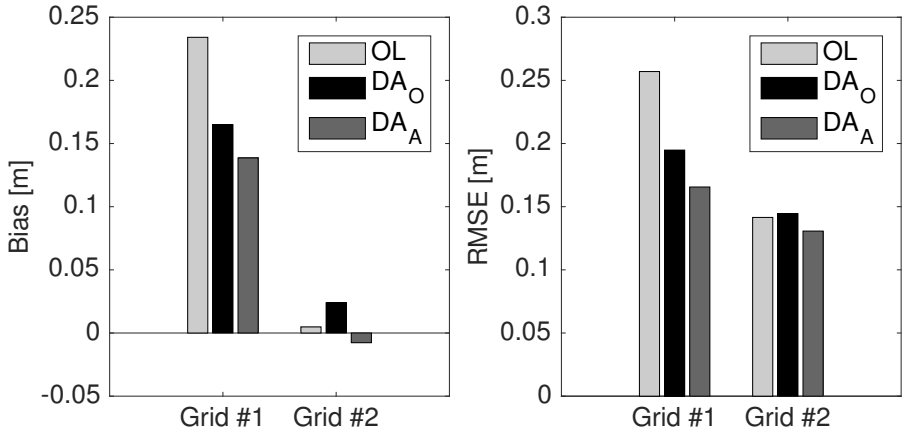

Figure 5.4: Histograms of computed bias and RMSE for model evaluation (including OL, DA_O, and DA_A experiments) at two locations in Quebec and Newfoundland, Canada. Grid #1 is at (53.69°N, 73.67°W), and grid #2 is at (48.71°N, 72.62°W).

as shown in Table 5.2. For both DA_O and DA_{A+F} experiments, student's t tests suggest rejecting the null hypothesis at the significance level of 5%. Therefore, positive NICs computed from the DA_{A+F} experiment suggest that including an atmospheric-and-forest decoupling procedure is helpful at decorrelating non-SWE related signals from the observations, and further adding information to the OL-derived estimates.

Table 5.2: Computed NICs obtained from both DA_O and DA_{A+F} during comparison against GSOD snow depth observations. The null hypothesis used in the student's t-test (one tail) is the computed mean NIC metric is not statistically different from zero at a significance level of 5%. In addition, $\sigma_{NIC_{RMSE}}$ is the standard deviation of the NIC_{RMSE}; similarly, $\sigma_{NIC_{NSE}}$ is the standard deviation of the NIC_{NSE}.

Experiment	Mean NIC_{RMSE} $\pm$ $\sigma_{NIC_{RMSE}}$	Mean NIC_{NSE} $\pm$ $\sigma_{NIC_{NSE}}$	Student's t-test (one tail)
DA_O	-0.11 $\pm$ 0.16	-0.25 $\pm$ 0.37	reject the null hypothesis
DA_{A+F}	0.06 $\pm$ 0.08	0.11 $\pm$ 0.14	reject the null hypothesis

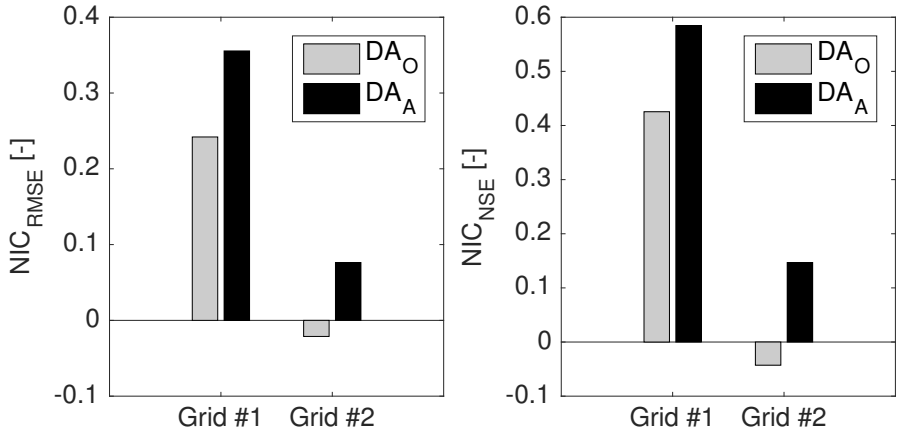

Figure 5.5: Histograms of computed NIC_{RMSE} and NIC_{NSE} for model evaluation (including DA_O, and DA_A experiments) at two locations in Quebec and Newfoundland, Canada. Grid #1 is at (53.69°N, 73.67°W), and grid #2 is at (48.71°N, 72.62°W).

5.4 Conclusions and future work

A SVM with four-input-state was constructed for the purpose of multifrequency, multipolarization AMSR-E ΔTb estimation within a radiance assimilation framework. In order to systematically address the challenge of estimating snow mass across forested regions, an atmospheric-and-forest decoupling procedure was used here prior to SVM training and prediction activity.

Model-derived results from various experiments (i.e., with and without assimilation) in Quebec and Newfoundland, Canada were presented to compare against closest in-situ GSOD snow depth observations from 2002 to 2011. Compared with OL-derived snow depth estimates at two grids in the domain, DA_A experiment reduced the RMSE by $\sim$36%, and $\sim$8%, respectively. In addition, model-derived SWE and snow depth estimates from various experiments were compared against

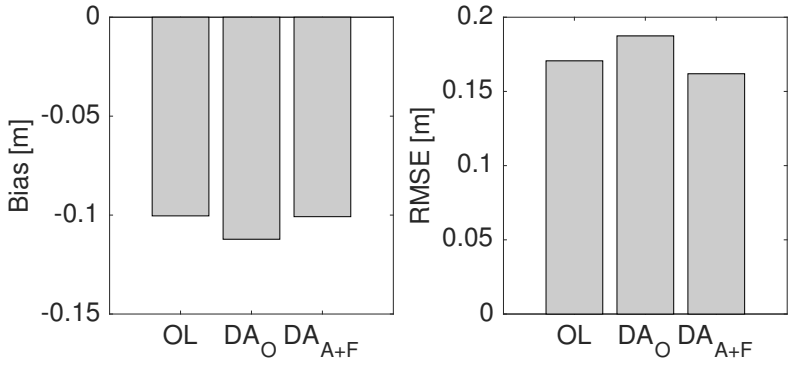

Figure 5.6: Histograms of average bias and RMSE for model evaluation in places covered with relatively dense evergreen needle-leaved forest colocated with taiga snow cover type across North America. The eight grids used in model evaluation are shown in Figure 5.7g).

available snow products. All DA experiments tend to yield estimates moving towards ESA GlobSnow SWE product (relative to OL-derived SWE) and CMC snow depth product (relative to OL-derived snow depth) in Quebec and Newfoundland, Canada. However, there is a significant pattern mismatch between different snow products and model-derived estimates, especially during early snow accumulation phase, which might be attributed to the highly variable snow conditions in the domain complicated by dense forest cover and significant lake effects.

In order to further analyze the model performance coupled with the forest transmissivity model as applied for regions covered with evergreen needle-leaved forest colocated with taiga snow cover, eight grids having forest cover fraction greater than 85% in North America with colocated GSOD stations were selected in the comparison. DA_{A+F}-derived estimates decreased the RMSE by $\sim$5% relative to OL-derived estimates. Further, positive NICs computed from DA_{A+F} experiment also

showed that including an atmospheric-and-forest decoupling procedure is helpful at decorrelating non-SWE related signals from the observations, and further adding information to the OL-derived estimates.

The positive NICs witnessed at both DA_A and DA_{A+F} experiments via assimilating either atmospherically-decoupled ΔTbs or atmospheric-and-forest-decoupled ΔTbs suggest that removing non-snow related radiance emissions prior to SVM training and prediction activities might be helpful at enhancing snow characterization. However, the lack of ground-based snow depth and SWE observations limits the study to draw a safe conclusion on the future application of the proposed DA system. Future work are required to demonstrate the proposed assimilation system's skill in estimating SWE and snow depth using a synthetic study (a.k.a., twin-experiment) across heavily vegetated regions.

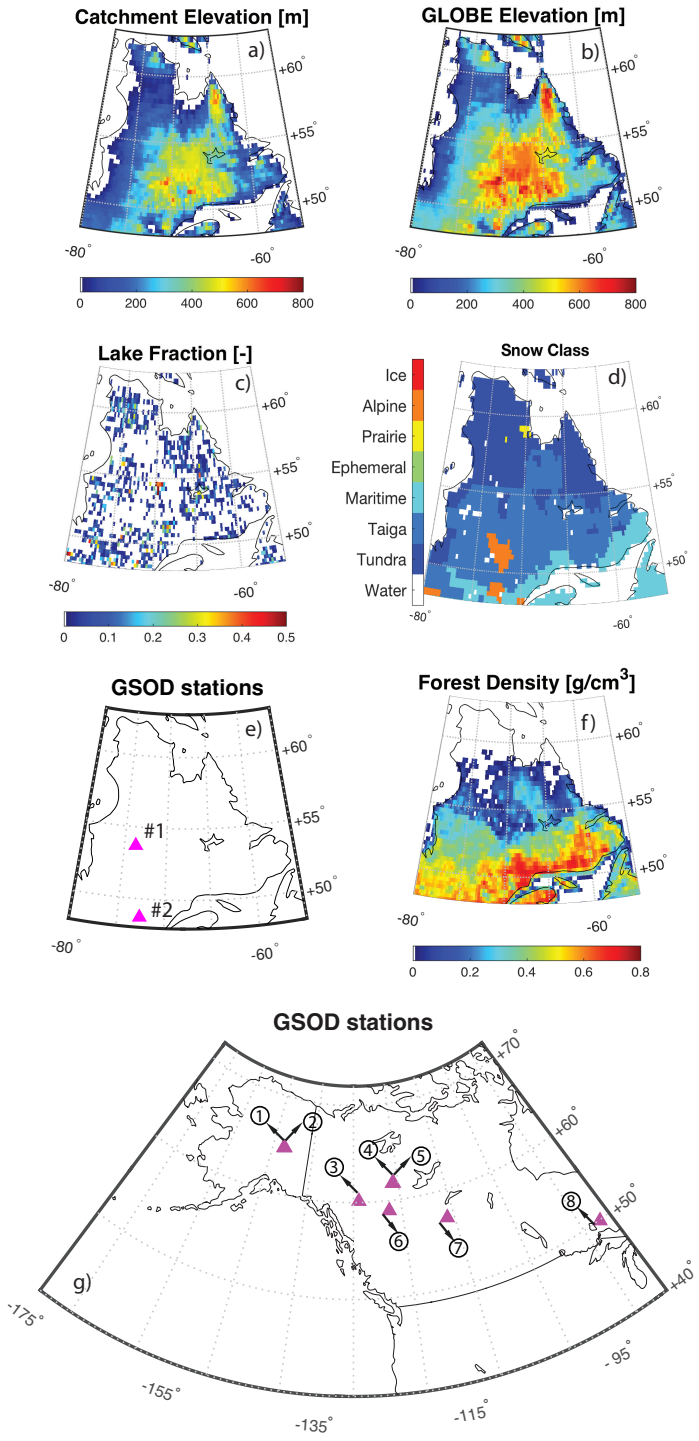

Figure 5.7: a) Catchment elevation, b) elevation map obtained from Global Land One-km Base Elevation Project (GLOBE) (aggregating onto the 25-km EASE-Grid), c) Catchment lake fraction distribution, d) snow cover type [74], e) two Global Summary Of the Day (GSOD) stations used in model evaluation in Quebec, Canada (see Section 5.3.2.1), f) forest density distribution from [75], and g) eight GSOD stations used in model evaluation at places covered with relatively dense evergreen needle-leaved forest colocated with taiga snow (see Section 5.3.2.2).

Chapter 6: Conclusions and future work

6.1 Conclusions and original contributions

The four chapters described above amount to a feasibility assessment of a machine-learning-algorithm based radiance assimilation framework for snowpack characterization. The science question addressed in this thesis is: Can the predictability of snow water equivalent (SWE) and snow depth at regional and continental scales be improved through the systematic integration of passive microwave (PMW) measurements collected by satellite-based instrumentation and a machine-learning based algorithm into a land surface model?

In Chapter 2, normalized sensitivity coefficients are computed to diagnose machine learning algorithm performance as a function of time and space. The results showed that when using the artificial neural network (ANN), approximately 20% of locations across North America are relatively sensitive to SWE. However, more than 65% of locations in the support vector machine (SVM) based Tb estimates are sensitive relative to perturbations in SWE at all frequency and polarization combinations. Further, the SVM-based results suggest the algorithm is sensitive in both shallow and deep SWE conditions, SWE with and without overlying forest canopy, and during both the snow accumulation and snow ablation seasons. Therefore, these

findings suggest that compared with the ANN, the SVM could potentially serve as a more efficient and effective measurement model operator within a radiance assimilation framework for the purpose of improving SWE estimates across regional- and continental-scales.

In Chapter 3, an advanced land surface model is merged with PMW brightness temperature (Tb) observations from the Advanced Microwave Scanning Radiometer - Earth Observing System (AMSR-E) using a well-trained SVM within a data assimilation framework. The one-dimensional Ensemble Kalman filter (EnKF) framework uses a SVM-based model as the observation operator. The impact of simultaneously assimilating multiple observations at different frequency and polarization combinations is explored. The performance of the radiance assimilation framework is then evaluated via comparisons to state-of-the-art SWE and snow depth products as well as available ground-based observations across Alaska for the years 2002 to 2011. In general, improvements in goodness-of-fit statistics on snow depth, and SWE estimates are achieved as a result of the assimilation procedure. The systematic errors and random errors in snow estimates were reduced by $\sim$40%, and $\sim$18% (on average) after implementing radiance assimilation. In addition, representativeness errors and overlying vegetation are identified as the two most important factors that negatively impact model performance. The representativeness error might be partially minimized by eliminating stations with significant elevation discrepancies whereas an atmospheric-forest-decoupling procedure could eventually be applied to minimize uncertainties associated with vegetation attenuation in an effort to enhance snow characterization over forested regions.

In Chapter 4, two significant sources of uncertainty prevalent in SWE retrievals derived from AMSR-E PMW Tb observations at 18.7 GHz and 36.5 GHz are addressed. Namely, atmospheric and overlying forest effects are decoupled from the original AMSR-E PMW Tb observations using relatively simple, first-order radiative transfer models. Comparisons against independent Tb measurements collected during airborne PMW Tb surveys highlight the effectiveness of the proposed AMSR-E atmospheric decoupling procedure. The atmospheric contribution to Tb ranges from 1 K to 3 K depending on the frequency and polarization measured as well as meteorologic conditions at the time of AMSR-E overpass. It is further shown that forest decoupling should be conducted as a function of both land cover type and snow cover class. The exponential decay relationship between the forest structure parameter, namely, MODIS-derived leaf area index (LAI) and forest transmissivity, is fitted across snow-covered terrain in North America. The fitted exponential function can be utilized during forest decoupling activities for evergreen needle-leaved forest and woody savanna regions, but remains uncertain in other forest types due to a sparsity of snow-covered areas. By removing forest-related Tb contributions from the original AMSR-E observations, the results suggest that Tb spectral difference between 18.7 GHz and 36.5 GHz, in general, increases across thinly-vegetated to heavily-vegetated regions, which might be beneficial when applied to the proposed one dimensional EnKF framework in the context of radiance assimilation.

In Chapter 5, an atmospheric-and-forest decoupling procedure was tested for use within the proposed assimilation system. Model-derived SWE and snow depth estimates from various data assimilation (DA) experiments were compared against

available snow products. It is shown that all DA experiments tend to yield estimates moving towards ESA GlobSnow SWE product (relative to OL-derived SWE), and CMC snow depth product (relative to OL-derived snow depth). In addition, model-derived results from various experiments (i.e., with and without assimilation, with and without atmospheric decoupling procedure) were presented to compare against in-situ snow depth observations in Quebec and Newfoundland, Canada, from 2002 to 2011. Compared with open-loop (OL) derived snow depth estimates at two grids, the DA_A experiment (with atmospheric decoupling procedure) reduced the random errors by ∼36%, and ∼8%, respectively. Further, model-derived results from various experiments (i.e., with and without assimilation, with and without atmospheric-and-forest decoupling procedure) were presented to compare against in-situ snow depth observations in North America at places covered with relatively dense evergreen needle-leaved forest cover colocated with taiga snow cover from 2002 to 2011. Compared with open-loop (OL) derived snow depth estimates at eight grids, the DA_{A+F} experiment (with atmospheric-and-forest decoupling procedure) reduced the random errors by ∼5% (on average). In general, the positive normalized information contribution (NIC) metrics witnessed at DA experiments via assimilating either atmospherically-decoupled ΔTbs or atmospheric-and-forest-decoupled ΔTbs suggest that removing non-snow related radiance emissions prior to SVM training and prediction activities is helpful at enhancing snow characterization.

In summary, this study supports the conclusion that a well-trained SVM can potentially be used as the observation model operator within a radiance assimilation framework to characterize snow mass across regional scales.

6.2 Future work

6.2.1 Minimization of representativeness errors during DA framework evaluation

The study used the absolute relative elevation difference of 150% to remove the station-grid comparison pairs having significantly different elevation conditions. Further investigations are required to test out the effect of using the absolute elevation difference of 500m to maintain station representativeness. In other words, a better scheme of minimizing representativeness errors during DA framework evaluation procedure is needed.

6.2.2 Robustness experiments of the DA framework at the code development level

A set of codes for point-scale and regional-scale SVM integration has been developed to read trained SVMs into the Fortran-based Catchment model in order to generate Tb output systematically (see Appendix E and F). Further investigations are required to promote coding efficiency in terms of predicting Tb across North America and further entire globe.

6.2.3 Robustness experiments of the DA framework on assimilating other sources of satellite-based Tb observations

It is anticipated that the proposed DA framework could be extended to include observations from other satellite-based sensors (e.g., the Special Sensor Microwave Imager (SSM/I) and the Advanced Microwave Scanning Radiometer 2 (AMSR2)). If the DA framework is robust enough, it would offer great potential to extend the SWE predictability back in time 1987 when SSM/I data collection first began; also, it would provide opportunity to continue assimilating PMW Tb observations obtained from AMSR2 en route to estimate snow-related states across the globe since AMSR-E stopped working in October 2011.

6.2.4 Robustness experiments of the DA framework on estimating other hydrologic states or fluxes

It is hypothesized that improvements in SWE magnitude and timing will result in improvements to other hydrologic state variables and fluxes generated through the hydrologic response. Further analysis could be extended to investigate the impact of soil moisture estimation based on the proposed DA system. It is anticipated that the terrestrial water storage estimates could also be improved as a result of implementing the DA system, which could be evaluated via comparing against the information derived from gravity recovery and climate experiment (GRACE) measurements.

Appendix A: ANN and SVM framework

A.1 ANN Framework

An ANN is a mathematical model inspired by biological neural networks. An ANN consists of a series of layers: (1) an input layer of neurons used for receiving information outside the network, (2) one or more hidden layer(s) acting as a bridge to connect the input layer with the output layer with input and output signals remaining within the network, and (3) an output layer to send the data out of the network. The ANN proposed for this study is a feed-forward perceptron network with one hidden layer of 10 hidden nodes [59] and supervised learning using back-propagation [153, 154]. A series of tests varying the number of neurons as part of one or more hidden layers were conducted, and hence the formulated ANN-based network is deemed sufficient in size without unnecessary complexity [59].

In a constructed ANN, each layer contains multiple processing units (i.e., neurons) connecting with those in the adjacent layers and an independent weight is attached to each link. The input to each neuron in the next layer is the sum of all its incoming connection weights multiplied by their connecting input neural activation value [30, 155]. In general, it is assumed that each processing unit provides an additive contribution to the connected output neuron, which may take on the form

as:

$$x_j = \sum_{i=1}^{N_i} w_{ji} I_i \tag{A.1}$$

where x_j is a single value (a.k.a., "net input" [156]) calculated by combining all the connected input units for the j^{th} propagated (output) unit; N_i is the total number of inputs; w_{ji} is the interconnection wight between the i^{th} input neuron and the j^{th} propagated neuron; and I_i is the i^{th} model input. An example application of interconnection weights between the input, hidden, and output layers is shown in [59].

Model input space may have different units as well as a wide range of magnitudes; hence, except for each neuron in the output layer, most neurons in the ANN are required to transform their net inputs using a scalar-to-scalar function prior to training, which is called the activation function [156]. The activation function, , employed in this study between the model input layer and hidden layer is the tangent (non-linear) sigmoid function, which can be expressed as:

$$f(x) = \frac{2}{1 + \exp(-2x)} - 1, \tag{A.2}$$

whereas the activation function used between the hidden layer and the output layer is a positive, linear transfer function. The transfer functions described here were selected based on a series of validation tests using different activation functions [59], and in general, outperformed the other activation functions tested during initial development.

During training, the mean squared error for a single output neuron can be

computed using the following equation:

$$MSE = \frac{1}{2}\sum_{i=1}^{p} \|\mathbf{\Lambda}_i - \mathbf{\Omega}_i\|^2 \tag{A.3}$$

where $\mathbf{\Lambda}_i$ is the i^{th} ANN-based estimates of Tb (K), $\mathbf{\Omega}_i$ is the i^{th} value of the AMSR-E training target Tb (K), p is the total number of evaluated time steps, and $\|\cdot\|$ represents the Euclidean norm operator between the estimated (ANN-derived) Tb and the measured (AMSR-E collected) Tb. The back-propagation learning cycle during each ANN training routine for each location is utilized in order to find the MSE minima such that a set of best weights (i.e., vector $\mathbf{w}$ in Equation A.1) will be found at the same time.

A.2 SVM Framework

Both training and testing datasets should be scaled before training the SVM, which is a crucial step in this ML technique [85]. In this study, there are a total of 11 geophysical variables and each of them is measured in a different scale with a different unit and has a different range of possible values. It is often beneficial to scale all features to a common range [157] such that attributes in greater numeric ranges will not dominate those in smaller ranges [85]. In order to define the scaling range (i.e., the upper limit, and the lower limit of the scaling interval), eight different sets of scaling intervals were tested. Ultimately, the SVM utilized in this paper defines the scaling interval as one with a lower bound of one and an upper bound of two.

Based on the principle of structured risk minimization, the decision function

of the SVM method can be written as:

$$\begin{aligned} f(\mathbf{x}) &= \sum_{i=1}^{p} w_i \Phi_i(x) + \delta \\ &= \mathbf{w}^T \Phi(\mathbf{x}) + \delta \end{aligned} \tag{A.4}$$

where p is the total number of evaluated time steps, $\mathbf{w}$ =[w_1, $\cdots$, w_p] represents a vector of weights, $\Phi(\mathbf{x})$ is a nonlinear function that maps the original model input space into a higher-dimension feature space, and δ is a bias coefficient. The goal of SVM learning is to determine a best set of parameters in order to minimize the error between the estimation, $f(\mathbf{x})$, and the training targets, $\mathbf{z}$, collected from the AMSR-E in this context. This SVM-related optimization (minimization) problem can then be solved by the introduction of Lagrangian multipliers, α_i and α_i^*, (where i = 1, 2, $\cdots$, m) in a dual form [67, 158], which is written as:

$$\begin{aligned} \min_{\alpha_i, \alpha_i^*} \quad & \tfrac{1}{2} \textstyle\sum_{i,j=1}^{m} (\alpha_i - \alpha_i^*)(\alpha_i - \alpha_i^*)[\Phi(\mathbf{x}_i)^T \Phi(\mathbf{x}_j)] \\ & + \epsilon \textstyle\sum_{i=1}^{m} (\alpha_i + \alpha_i^*) + \sum_{i=1}^{m} z_i(\alpha_i - \alpha_i^*) \\ \text{s.t.} \quad & \textstyle\sum_{i=1}^{m} (\alpha_i - \alpha_i^*) = 0, \\ & \alpha_i, \alpha_i^* \in [0, C], i = 1, 2, \cdots, m \end{aligned} \tag{A.5}$$

where ϵ ($\epsilon > 0$) is defined as an error tolerance parameter, m is the total number of training targets (in time) for a given location, and C (C ¿ 0) is a regularized constant (a.k.a., penalty parameter) that determines the trade-off between the training risk and the model uniformity [159]. The training points with nonzero Lagrange multipliers are defined as the so-called "support vectors", which comprise the decision space and determine the model function. The inner (dot) product in Equation A.5 between $\Phi(\mathbf{x}_i)$ and $\Phi(\mathbf{x}_j)$ is defined as the "kernel function", which satisfies Mercers

condition and can be expressed as:

$$K(\mathbf{x}_i, \mathbf{x}_j) = \Phi(\mathbf{x}_i)^T \Phi(\mathbf{x}_j). \tag{A.6}$$

The computation of $\Phi(\mathbf{x}_i)^T \Phi(\mathbf{x}_j)$ in the feature space is often too complex to perform directly, especially in high-dimensional and nonlinear problems. In order to avoid employing the mapping function $\Phi(\mathbf{x})$ directly in Equation A.5, it is necessary to further define the kernel function form as:

$$\begin{aligned} K(\mathbf{x}_i, \mathbf{x}_j) &= \Phi(\mathbf{x}_i)^T \Phi(\mathbf{x}_j) \\ &= \exp(-\gamma \|\mathbf{x}_i - \mathbf{x}_j\|^2). \end{aligned} \tag{A.7}$$

The kernel function in Equation A.7 is an example of a Gaussian radial basis function kernel, where $\|\cdot\|$ represents the Euclidean norm between $\Phi(\mathbf{x}_i)$ and $\Phi(\mathbf{x}_j)$, and γ ($\gamma > 0$) is an adjustable parameter to control the width of the Gaussian distribution. In other words, using the kernel in the model input space is equivalent to performing the mapping in feature space and then applying the dot product in that space. Therefore, the decision function in Equation A.4 can be rewritten as:

$$f(\mathbf{x}) = \sum_{i=1}^{n} (\alpha_i, \alpha_i^*) K(\mathbf{x}, \mathbf{x}_i) + \delta \tag{A.8}$$

where n is the number of support vectors. An example figure of the SVM architecture is shown in [60].

Appendix B: Goodness-of-fit statistics

Goodness-of-fit statistics used in this dissertation include bias, root mean squared error (RMSE), unbiased root mean squared error (ubRMSE), and correlation coefficient (R). The bias was computed as [160]:

$$\begin{aligned} bias &= \bar{y}_{est} - \bar{y}_{obs} \\ &= \frac{1}{n}\sum_{i=1}^{n} y_{est,i} - \frac{1}{n}\sum_{i=1}^{n} y_{obs,i} \end{aligned} \tag{B.1}$$

where y is the state variable, n is the sample size, y_{est} is the state variable estimation, $\bar{y}_{est}$ is the average estimate of state variables, y_{obs} is the state variable observations obtained from ground-based instrumentations, and $\bar{y}_{obs}$ is the average value of observations. Therefore, bias reflects the systematic error in estimates when compared against observations.

Similarly, the RMSE was computed as [160]:

$$RMSE = \sqrt{\frac{1}{n}\sum_{i=1}^{n}(y_{est,i} - y_{obs,i})^2}. \tag{B.2}$$

In general, the RMSE reflects both systematic and random errors in the deviation of state variable estimates from the observations. Following the same nomenclature

described above, ubRMSE was computed as [161]:

$$\begin{aligned} ubRMSE &= \sqrt{RMSE^2 - bias^2} \\ &= \sqrt{RMSE^2 - (\bar{y}_{est} - \bar{y}_{obs})^2} \\ &= \sqrt{\frac{1}{n}\sum_{i=1}^{n}(y_{est,i} - y_{obs,i})^2 - (\bar{y}_{est} - \bar{y}_{obs})^2}. \end{aligned} \tag{B.3}$$

In general, ubRMSE represents the RMSE of the anomalies in y_{est}.

Finally, the correlation coefficient, R, was computed as [160]:

$$R = \frac{\sum_{i=1}^{n}(x_i - \bar{x})(z_i - \bar{z})}{\sqrt{\sum_{i=1}^{n}(x_i - \bar{x})^2}\sqrt{\sum_{i=1}^{n}(z_i - \bar{z})^2}} \tag{B.4}$$

where x and z are state variables of interest, n is the sample size, $\bar{x}$ is the mean value of the set of variable x, and $\bar{z}$ is the mean value of the set of variable z. R varies from -1 to +1, which reflects the strength and direction of the relationship between x and z. A negative R represents a relationship between x and z such that an increase in x yields a decrease in z. In the Chapter 4, forest transmissivity decreased as LAI increased, which yielded a negative R over the entire temporal and spatial domain of investigation.

Besides bias, RMSE, ubRMSE, and R, the normalized information contribution (NIC) was computed to quantify the improvement or degradation due to DA for the comparison against open-loop (OL) derived estimates [40]. The NIC for the RMSE, NIC_{RMSE}, was expressed as [40]:

$$NIC_{RMSE} = \frac{RMSE_{OL} - RMSE_{DA}}{RMSE_{OL}} \tag{B.5}$$

where the $RMSE_{OL}$ is the OL-based RMSE, and $RMSE_{DA}$ is the data assimilation (DA) derived RMSE. Similarly, the NIC for the Nash-Sutcliffe model efficiency

coefficient (NSE), NIC_{NSE}, was computed as [40]:

$$NIC_{NSE} = \frac{NSE_{DA} - NSE_{OL}}{1 - NSE_{OL}} \tag{B.6}$$

where the NSE_{OL} is the OL-based NSE, and NSE_{DA} is the DA-derived NSE. The NSE in the Equation B.6 was computed as:

$$NSE = 1 - \frac{\sum_{j=1}^{N_t}(y_{obs,j} - y_{est,j})^2}{\sum_{j=1}^{N_t}(y_{obs,j} - \frac{1}{N_t}\sum_{j=1}^{N_t} y_{obs,j})^2}. \tag{B.7}$$

Appendix C: Innovation, normalized innovation and filter sub-optimality

For a given location, the innovation vector at time t, $\mathbf{d_t}$, could be written as:

$$\mathbf{d}_t = < (\mathbf{y}_t + \mathbf{v}) > - < \mathbf{\Phi}_t(x_t^-) > \tag{C.1}$$

where $< \cdot >$ represent the ensemble mean operator, $\mathbf{y_t}$ is the observation vector, $\mathbf{v}$ is the observation error vector, $\mathbf{\Phi}_t(x_t^-)$ is the predicted observations obtained from SVM as a function of the prior estimate of state x_t^-, and $\mathbf{d}_t$ is the innovation vector, which is a $[4 \times 1]$ vector in the context of spectral difference as a function of frequency and polarization. The covariance matrix, $cov(\mathbf{d}_t, \mathbf{d}_{t-k})$, of $\mathbf{d}_t$ and $\mathbf{d}_{t-k}$ are the $[4 \times 4]$ matrix, which could be further written as:

$$cov(\mathbf{d}_t, \mathbf{d}_{t-k}) = \mathbf{E}([\mathbf{d}_t - \mathbf{E}(\mathbf{d}_t)][\mathbf{d}_{t-k} - \mathbf{E}(\mathbf{d}_{t-k})]^T). \tag{C.2}$$

where $\mathbf{E}[\cdot]$ is the expected value operator, $[\cdot]^T$ is the vector transpose.

Assuming the EnKF is optimal with all assumptions satisfied in a typical EnKF, Equation C.2 should have the following features [114]:

$$\mathbf{E}[\mathbf{d}_t \mathbf{d}_{t-k}^T] = \begin{cases} \mathbf{0}, & \text{if } k \neq 0 \\ \mathbf{\Phi}_t \mathbf{P}_t^- \mathbf{\Phi}_t^T + \mathbf{R}_t, & \text{if } k = 0 \end{cases} \tag{C.3}$$

where $\mathbf{R}_t$ is the observation error covariance matrix, and $\mathbf{\Phi}_t \mathbf{P}_t^- \mathbf{\Phi}_t^T$ is the error covariance of the observation operator estimates. It is worthy noting again that

Kalman filter theory assumes linear (or linearized) observation model operator (i.e., Φ in the Equation C.1 and C.3), which does not hold in this study with SVM to be non-linear. Given all assumptions in a typical EnKF is satisfied, the innovation sequence should have the properties of zero-mean, and temporally-uncorrelated for each observation channel. In addition, the innovation covariance should equal to the sum of the observation operator estimate error covariance and observation error covariance.

Define the sum of the observation operator estimate error covariance and observation error covariance as $\mathbf{S}_t$, and the normalized innovation as

$$\mathbf{NI}_t = \frac{\mathbf{d_t}}{diag(\sqrt{\mathbf{S_t}})}, \tag{C.4}$$

where $diag(\cdot)$ represents only taking the diagonal elements of the matrix. Equation C.3 could now be written as:

$$\mathbf{E}[\mathbf{NI}_t\mathbf{NI}_{t-k}^T] = \begin{cases} \mathbf{0}, & \text{if } k \neq 0 \\ \mathbf{1}, & \text{if } k = 0 \end{cases} \tag{C.5}$$

Therefore, Equation C.5 indicates that an optimal filter should yield a NI sequence with zero-mean, unit variance, and zero autocorrelation for each observation channel.

Appendix D: Sensitivity analysis of decoupled Tb predictions to model parameters

Sensitivity analysis is an important tool for assessing the relative importance of causative factors in a model [61,160]. In this appendix, a sensitivity analysis was used to investigate the response of decoupled, multi-frequency, multi-polarization Tb (see Equation 4.7 for details) with respect to small perturbations in both model input and model parameters. In order to quantify the relative importance of each tested model input variable and model parameter, Normalized Sensitivity Coefficients (NSCs [unitless]; [71]) were computed as:

$$\begin{aligned} NSC_{i,j} &= (\frac{\partial M_j}{\partial p_i}) \cdot (\frac{p_i^0}{M_j^0}) \\ &\approx (\frac{M_j - M_j^0}{\Delta p_i}) \cdot (\frac{p_i^0}{M_j^0}) \end{aligned} \tag{D.1}$$

where M_j^0 is the nominal model output; M_j is the perturbed model output; p_i is the perturbed input; and p_i^0 is the nominal model input.

Model input variables in the NSC calculations include (1) TPW content obtained from MERRA, (2) MERRA-derived near-surface air temperature, (3) MODIS-derived LAI, (4) MODIS-derived forest cover fraction, and (5) Catchment-derived skin temperature. It is found that NSCs at 36H are generally larger than those at

18H, 18V and 36V. The greater sensitivity at 36H is consistent with the physical rationale shown in Figures 4.7 and 4.6 and discussed in Section 4.4.2.3. In addition, it is suggested that decoupled snow Tb results are more sensitive to small perturbations in air temperature and skin temperature, relative to TPW, LAI and forest cover fraction given the same magnitude of perturbation in the input.

Using NSCs at 36H as an example to further highlight sensitivities in the proposed decoupling procedure, it could be roughly estimated that a 5% increase in TPW, which corresponds to a $\sim$0.5 kg m^{-2} in TPW increase (on average) tends to decrease computed snow Tb by $\sim$0.05 K. Meanwhile, when the air temperature or the skin temperature increases by 1 K, snow Tb at 36H tends to decrease by $\sim$0.1 K. If LAI (with units of m^2 leaf m^{-2} ground) increases by 0.1, snow Tb will decrease by $\sim$0.4 K with respect to the mean. Further, if forest cover (unitless) increase by 10%, snow Tb at 36H tends to decrease by 0.8 K.

Previous studies found that the BNU LAI product has an approximated uncertainty of 0.66 [134], and MODIS forest cover fraction product has an uncertainty of $\sim$10% [75], which was obtained based on ground-based validation dataset from the United States and Brazil. In addition, the MERRA-derived temperature has an uncertainty of $\sim$2-3 K [162] when compared against satellite-based temperature retrievals. Even though LAI is not the most sensitive parameter in the model according to the computed NSC value, the relatively significant uncertainty in the LAI product itself is likely to introduce the largest component of error (relative to other model input parameters) in the computed snow Tb values. Therefore, as mentioned in the Section 4.3, the accuracy of the regional daily LAI mapping could adversely

impact the forest-related portion of the Tb decoupling procedure.

Similar to the NSC computation used in the model input variable sensitivity assessment, model parameter sensitivity was also analyzed. Model parameters tested are those shown in Equations 4.4, 4.5 and 4.14 that are ultimately applied in the two-step decoupling procedure. Similar to the findings mentioned above, NSCs at 36.5 GHz are generally larger than those at 18.7 GHz due to the shorter emission (snow) depth at higher frequencies, which agrees well with the fundamental physics. Further, among all six parameters, model output shows the strongest sensitivity to the perturbation in parameters as applied in Equation 4.14 during the LAI-forest transmissivity regression. As stated previously, the accuracy of the regression coefficient parameters largely depends on the accuracy of the forest transmissivity retrieval based on the first-order, physically-based radiative transfer model shown in Equation 4.8. It is worth noting that a successful application of Equation 4.8 relies on an accurate estimation of skin temperature, snow temperature, Tb observations in both clear-cut and forested pixels, and winter LAI values used to distinguish clear-cut from vegetated snow-covered land.

Appendix E: Scheme for distributing column-integrated SWE into the three-layer snow model

During EnKF update (see Section 3.2.3.1), column-integrated SWE is the state of variable. Therefore, it is necessary to re-distribute the column-integrated SWE (and other snow-related information) into three layers after assimilation update procedure but prior to launching Catchment forward model. Figure E.1 shows the scheme for distributing column-integrated SWE into three layers. It also shows how to adjust other snow-related states (i.e., snow depth (SD) and snow specific heat content (HTSN)) information based on the updated SWE information in each snow layer. It is important to note that current study did not use the subroutine `relayer2` because it is found to fail to re-distribute SWE at the case when the middle-layer of a snow pack does not have SWE but both bottom-layer and top-layer do. In addition, an appropriate definition of the maximum layer thickness profile (i.e., `DZMAX`) in the subroutine `relayer2` still requires further investigation.

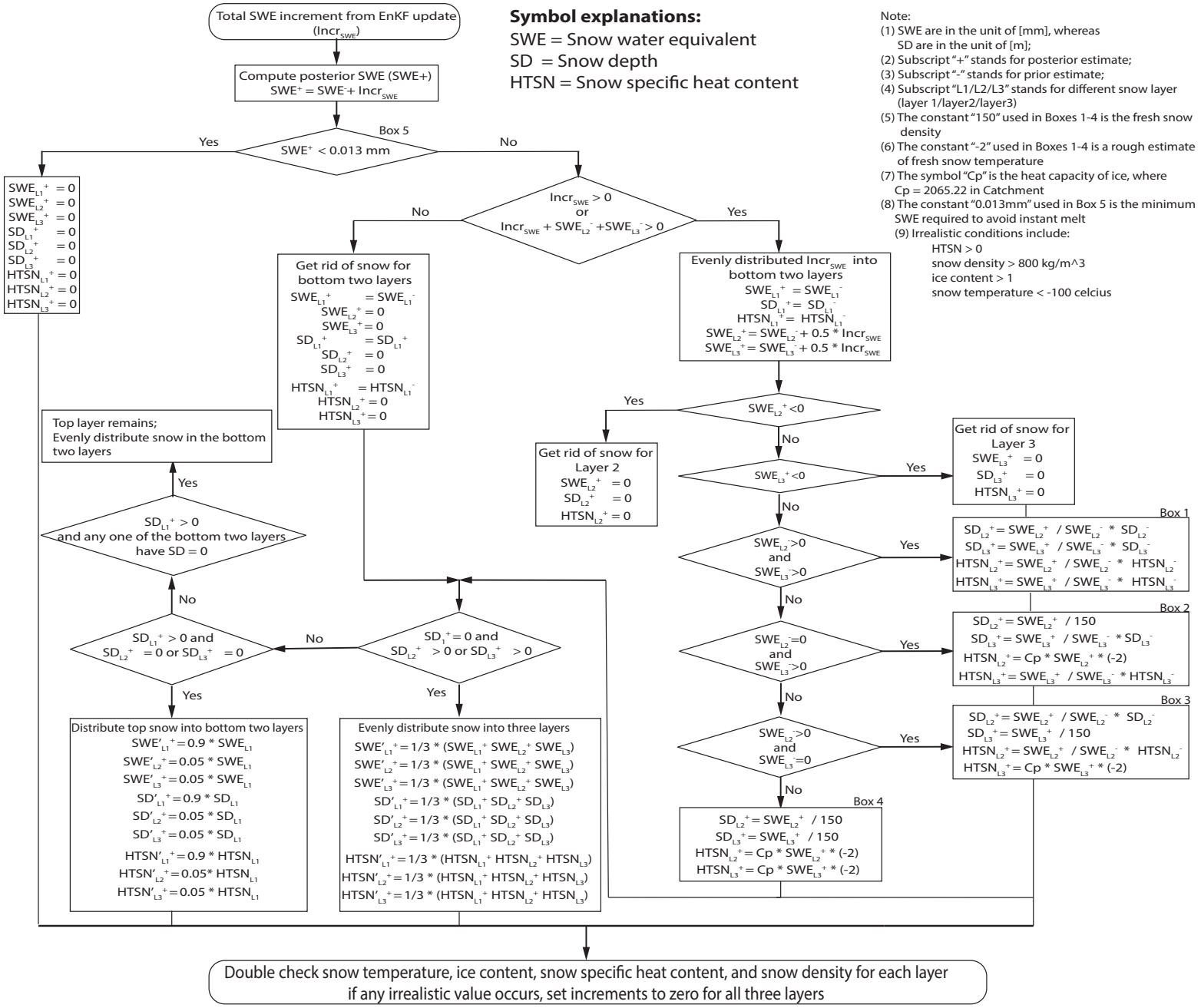

Figure E.1: Scheme for distributing column-integrated SWE into the three-layer snow model.

Appendix F: Summary of changes made for integrating SVM into NASA assimilation module

A series of changes were made in the original NASA land data assimilation system (LDAS) in order to integrate SVM-based Tb predictions. These changes include: (1) source code development, and (2) assimilation options update.

F.0.1 Source code development

Figure F.1 summarizes all changes made to the source code in the original LDAS. It is important to note that current SVM-LDAS system is not optimal. Since each pixel in the domain is associated with a unique fortnightly SVM parameter `.txt` file, SVM-LDAS needs to read these parameter files for each pixel. The practice of storing numerous `.txt` formatted files is not optimal. In addition, too many read-write executions has significantly restricted SVM-LDAS from running efficiently. However, a couple of attempts have been made in order to find a better way to accommodate SVM prediction routines in the LDAS, unfortunately, none of them works as expected so far. These attempts include: (1) store SVM parameters into `hdf` formatted files; (2) store SVM parameters into `netcdf` formatted files; (3) read SVM parameters of `.mat` formatted files directly

in the Fortran environment; and (4) initiate Matlab© Engine in the Fortran environment to read SVM parameters in `.mat` formatted files. Both `hdf` formatted files and `netcdf` formatted files are not good at dealing with sparse matrices (http://www.unidata.ucar.edu/software/netcdf/netcdf-4/newdocs/netcdf.html) whereas support vectors within each SVM are only available in sparse matrices. Therefore, future investigations are required to better accommodate SVM parameters and make them more reading friendly in the Fortran environment.

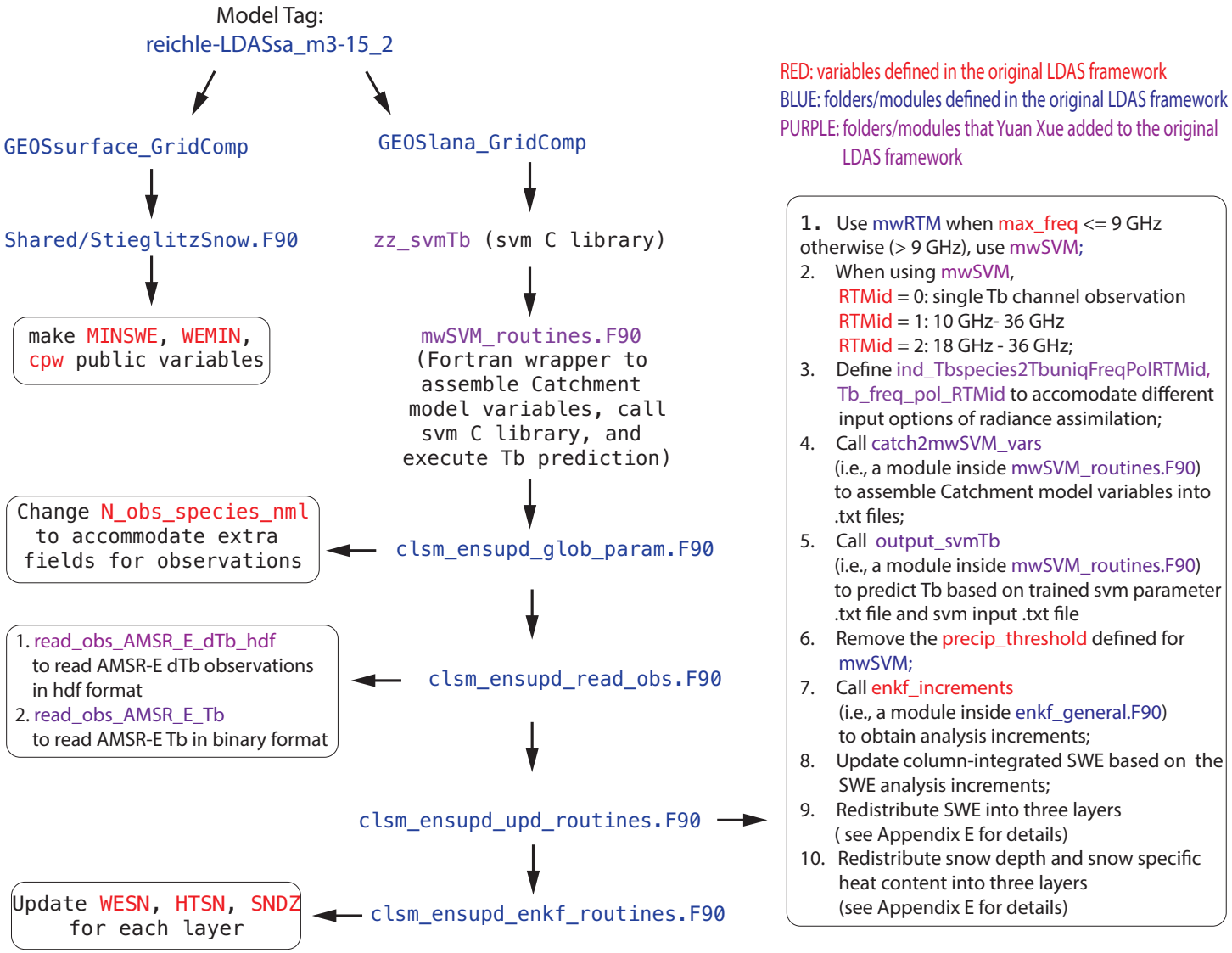

Figure F.1: Summary of key changes made to the original NASA LDAS in the source code.

F.0.2 Assimilation options update

Except for specifying perturbation settings in the `LDASsa_YX_inputs_ensprop.nml` namelist file and specifying domain latitude and longitude in the `LDASsa_YX_inputs_driver.nml` namelist file, two other files are required to be edited. A summary of changes made to these two namelist files were graphed in the Figure F.2.

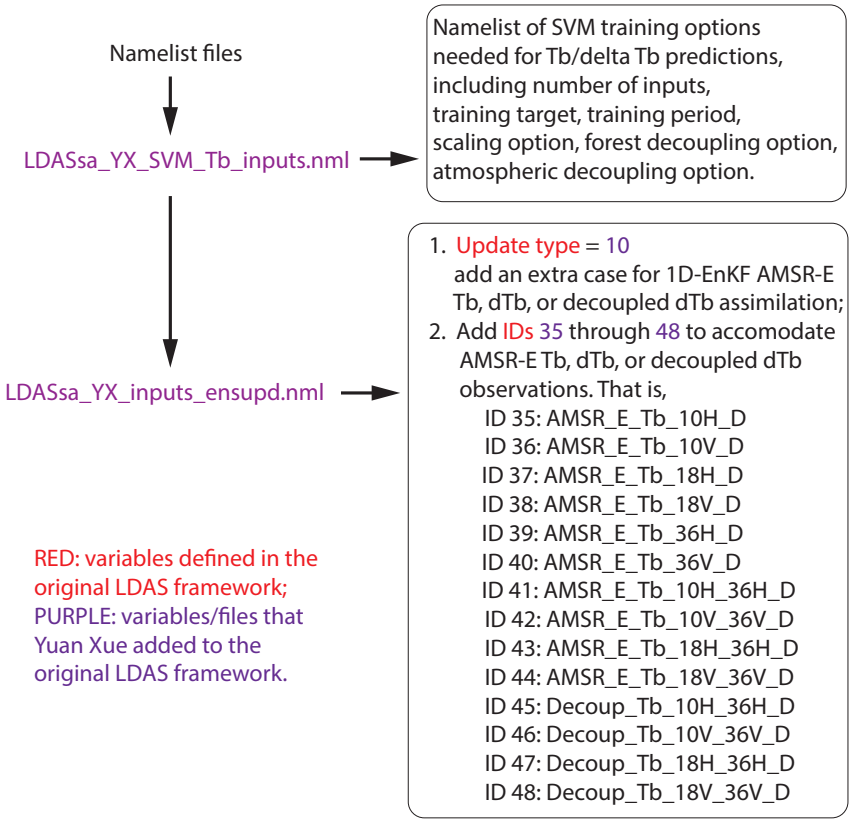

Figure F.2: Summary of key changes made to the original assimilation options in the namelist files.

Bibliography

[1] David a. Robinson, Kenneth F. Dewey, and Richard R. Heim. Global Snow Cover Monitoring: An Update, 1993.

[2] Glen E. Liston. Interrelationships among Snow Distribution, Snowmelt, and Snow Cover Depletion: Implications for Atmospheric, Hydrologic, and Ecologic Modeling, 1999.

[3] Richard Fernandes, Hongxu Zhao, Xuanji Wang, Jeff Key, Xin Qu, and Alex Hall. Controls on Northern Hemisphere snow albedo feedback quantified using satellite Earth observations. *Geophysical Research Letters*, 36(21):1–6, 2009.

[4] James L. Foster, Dorothy K. Hall, John B. Eylander, George a. Riggs, Son V. Nghiem, Marco Tedesco, Edward Kim, Paul M. Montesano, Richard E. J. Kelly, Kimberly a. Casey, and Bhaskar Choudhury. A blended global snow product using visible, passive microwave and scatterometer satellite data. *International Journal of Remote Sensing*, 32(5):1371–1395, March 2011.

[5] T P Barnett, J C Adam, and D P Lettenmaier. Potential impacts of a warming climate on water availability in snow-dominated regions. *Nature*, 438(7066):303–309, 2005.

[6] Jiarui Dong, Jeffrey P. Walker, Paul R. Houser, and Chaojiao Sun. Scanning multichannel microwave radiometer snow water equivalent assimilation. *Journal of Geophysical Research: Atmospheres*, 112(7):1–16, 2007.

[7] Rolf H. Reichle, Randal D. Koster, Gabriëlle J M De Lannoy, Barton a. Forman, Qing Liu, Sarith P P Mahanama, and Ally Toure. Assessment and enhancement of MERRA land surface hydrology estimates. *Journal of Climate*, 24(24):6322–6338, 2011.

[8] M. Lynch-Stieglitz. The development and validation of a simple snow model for the GISS GCM, 1994.

[9] Yungang Cao, Xiuchun Yang, and Xiaohua Zhu. Retrieval snow depth by artificial neural network methodology from integrated AMSR-E and in-situ data - A case study in Qinghai-tibet plateau. *Chinese Geographical Science*, 18(4):356–360, 2008.

[10] Matias Takala, Kari Luojus, Jouni Pulliainen, Chris Derksen, Juha Lemmetyinen, Juha Petri Kärnä, Jarkko Koskinen, and Bojan Bojkov. Estimating northern hemisphere snow water equivalent for climate research through assimilation of space-borne radiometer data and ground-based measurements. *Remote Sensing of Environment*, 115(12):3517–3529, 2011.

[11] Nando Foppa, Andreas Stoffel, and Roland Meister. Synergy of in situ and space borne observation for snow depth mapping in the Swiss Alps. *International Journal of Applied Earth Observation and Geoinformation*, 9(3):294–310, 2007.

[12] A.T.C. Chang, J.L. Foster, and D.K. Hall. Nimbus-7 SMMR derived global snow cover parameters. *Annals of Glaciology*, 9:39–44, 1987.

[13] AE Walker and BE Goodison. Discrimination of a wet snow cover using passive microwave satellite data. *Annals of Glaciology*, 17(1):307–311, 1993.

[14] R.E. Kelly, a.T. Chang, L. Tsang, and J.L. Foster. A prototype AMSR-E global snow area and snow depth algorithm. *IEEE Transactions on Geoscience and Remote Sensing*, 41(2):230–242, February 2003.

[15] A.T.C. Chang, J. L. Foster, and D. K. Hall. Effects of forest on the snow parameters derived from microwave measurements during the BOREAS winter field campaign. *Hydrological Processes*, 10(12):1565–1574, 1996.

[16] Richard Kelly. The AMSR-E snow depth algorithm: Description and initial results. *Journal of the Remote Sensing Society of Japan*, 29(1):307–317, 2009.

[17] G. Blöschl and M. Sivapalan. Scale issues in hydrological modelling: A review. *Hydrological Processes*, 9(3-4):251–290, April 1995.

[18] C. Derksen, A. Walker, and B. Goodison. Evaluation of passive microwave snow water equivalent retrievals across the boreal forest/tundra transition of western Canada. *Remote Sensing of Environment*, 96(3-4):315–327, 2005.

[19] R.L. Armstrong, A.T Chang, A. Rango, and E. Josberger. Snow depths and grain-size relationships with relevance for passive microwave studies. *Annals of Glaciology*, 17:171–176, 1993.

[20] L. Brucker, a. Royer, G. Picard, a. Langlois, and M. Fily. Hourly simulations of the microwave brightness temperature of seasonal snow in Quebec, Canada, using a coupled snow evolution–emission model. *Remote Sensing of Environment*, 115(8):1966–1977, August 2011.

[21] Dorothy K. Hall. Influence of depth hoar on microwave emission from snow in northern Alaska. *Cold Regions Science and Technology*, 13(3):225–231, 1987.

[22] D. K. Hall, A.T.C. Chang, and J. L. Foster. Detection of the depth-hoar layer in the snow-pack of the Arctic Coastal Plain of Alaska, USA, using satellite data. *Journal of Glaciology*, 32(110):87–94, 1986.

[23] James L. Foster, Chaojiao Sun, Jeffrey P. Walker, Richard Kelly, Alfred Chang, Jiarui Dong, and Hugh Powell. Quantifying the uncertainty in passive microwave snow water equivalent observations. *Remote Sensing of Environment*, 94(2):187–203, January 2005.

[24] Andrew Rees, Juha Lemmetyinen, Chris Derksen, Jouni Pulliainen, and Michael English. Observed and modelled effects of ice lens formation on passive microwave brightness temperatures over snow covered tundra. *Remote Sensing of Environment*, 114(1):116–126, 2010.

[25] C. Derksen, P. Toose, A. Rees, L. Wang, M. English, A. Walker, and M. Sturm. Development of a tundra-specific snow water equivalent retrieval algorithm for satellite passive microwave data. *Remote Sensing of Environment*, 114(8):1699–1709, 2010.

[26] Marco Tedesco and Parag S. Narvekar. Assessment of the NASA AMSR-E SWE product. *IEEE Journal of Selected Topics in Applied Earth Observations and Remote Sensing*, 3(1):141–159, 2010.

[27] Debbie Clifford. Global estimates of snow water equivalent from passive microwave instruments: history, challenges and future developments. *International Journal of Remote Sensing*, 31(14):3707–3726, August 2010.

[28] A T C Chang and L Tsang. A neural network approach to inversion of snow water equivalent from passive microwave measurements. *Nordic Hydrology*, 23(3):173–181, 1992.

[29] Daniel T Davis, Zhengxiao Chen, Leung Tsang, Jenq Neng Hawang, and Alfred T C Chang. Retrieval of snow parameters by iterative inversion of a neural network. *IEEE Transactions on Geoscience and Remote Sensing*, 31(4):842–857, 1993.

[30] M Tedesco, J Pulliainen, M Takala, M Hallikainen, and P Pampaloni. Artificial neural network-based techniques for the retrieval of SWE and snow depth from SSM / I data. *Remote Sensing of Environment*, 90:76–85, 2004.

[31] Dennis McLaughlin. An integrated approach to hydrologic data assimilation: Interpolation, smoothing, and filtering. *Advances in Water Resources*, 25(8-12):1275–1286, 2002.

[32] B. A. Forman and S. A. Margulis. Assimilation of multiresolution radiation products into a downwelling surface radiation model: 2. Posterior ensemble implementation. *J. Geophys. Res.*, 115(D22116):doi:10.1029/2010JD013950, 2010.

[33] Hsin-Cheng Huang and Noel Cressie. Spatio-temporal prediction of snow water equivalent using the Kalman filter. *Computational Statistics & Data Analysis*, 22(2):159–175, 1996.

[34] Andrew G. Slater and Martyn P. Clark. Snow Data Assimilation via an Ensemble Kalman Filter. *Journal of Hydrometeorology*, 7(3):478–493, 2006.

[35] Glen E. Liston and Christopher a. Hiemstra. A Simple Data Assimilation System for Complex Snow Distributions (SnowAssim). *Journal of Hydrometeorology*, 9(5):989–1004, 2008.

[36] Jan Magnusson, David Gustafsson, Fabia Husler, and Tobias Jonas. Assimilation of point SWE data into a distributed snow cover model comparing two contrasting methods. *Water Resources Research*, 50(10):7816–7835, 2014.

[37] Yuqiong Liu, Christa D. Peters-Lidard, Sujay Kumar, James L. Foster, Michael Shaw, Yudong Tian, and Gregory M. Fall. Assimilating satellite-

based snow depth and snow cover products for improving snow predictions in Alaska. *Advances in Water Resources*, 54:208–227, 2013.

[38] Yuqiong Liu, Christa D. Peters-Lidard, Sujay V. Kumar, Kristi R. Arsenault, and David M. Mocko. Blending satellite-based snow depth products with in situ observations for streamflow predictions in the Upper Colorado River Basin. *Water Resources Research*, 51(2):1182–1202, 2015.

[39] Sujay V. Kumar, Christa D. Peters-Lidard, Kristi R. Arsenault, Augusto Getirana, David Mocko, and Yuqiong Liu. Quantifying the Added Value of Snow Cover Area Observations in Passive Microwave Snow Depth Data Assimilation. *Journal of Hydrometeorology*, 16(4):1736–1741, 2015.

[40] Sujay V. Kumar, Christa D. Peters-Lidard, David Mocko, Rolf Reichle, Yuqiong Liu, Kristi R. Arsenault, Youlong Xia, Michael Ek, George Riggs, Ben Livneh, and M H Cosh. Assimilation of remotely sensed soil moisture and snow depth retrievals for drought estimation. *Journal of Hydrometeorology*, page 140603130821005, 2014.

[41] Konstantinos M. Andreadis and Dennis P. Lettenmaier. Assimilating remotely sensed snow observations into a macroscale hydrology model. *Advances in Water Resources*, 29(6):872–886, 2006.

[42] Gabriëlle J M De Lannoy, Rolf H. Reichle, Kristi R. Arsenault, Paul R. Houser, Sujay Kumar, Niko E C Verhoest, and Valentijn R N Pauwels. Multiscale assimilation of Advanced Microwave Scanning Radiometer-EOS snow

water equivalent and Moderate Resolution Imaging Spectroradiometer snow cover fraction observations in northern Colorado. *Water Resources Research*, 48(1):1–17, 2012.

[43] Hua Su, Zong Liang Yang, Guo Yue Niu, and Robert E. Dickinson. Enhancing the estimation of continental-scale snow water equivalent by assimilating MODIS snow cover with the ensemble Kalman filter. *Journal of Geophysical Research Atmospheres*, 113(8):1–12, 2008.

[44] Michael Durand, Noah P. Molotch, and Steven A. Margulis. Merging complementary remote sensing datasets in the context of snow water equivalent reconstruction. *Remote Sensing of Environment*, 112(3):1212–1225, 2008.

[45] Manuela Girotto, Steven A. Margulis, and Michael Durand. Probabilistic SWE reanalysis as a generalization of deterministic SWE reconstruction techniques. *Hydrological Processes*, 28(12):3875–3895, 2014.

[46] Steven A. Margulis, Gonzalo Cortés, Manuela Girotto, and Michael Durand. A Landsat-era Sierra Nevada (USA) Snow Reanalysis (1985-2015). *Journal of Hydrometeorology*, page 160211124352003, 2016.

[47] Yong Fei Zhang, Tim J. Hoar, Zong Liang Yang, Jeffrey L. Anderson, Ally M. Toure, and Matthew Rodell. Assimilation of MODIS snow cover through the Data Assimilation Research Testbed and the Community Land Model version 4. *Journal of Geophysical Research: Atmospheres*, 119(12):7091–7103, jun 2014.

[48] Jianhui Xu and Hong Shu. Assimilating MODIS-based albedo and snow cover fraction into the Common Land Model to improve snow depth simulation with direct insertion and deterministic ensemble Kalman filter methods. *Journal of Geophysical Research-Atmospheres*, 119(18):10684–10701, 2014.

[49] B. A. Forman, R. H. Reichle, and M. Rodell. Assimilation of terrestrial water storage from GRACE in a snow-dominated basin. *Water Resources Research*, 48(1):1–14, 2012.

[50] Yong-Fei Zhang and Zong-Liang Yang. Estimating uncertainties in the newly developed multi-source land snow data assimilation system. *Journal of Geophysical Research: Atmospheres*, 2016.

[51] J. R. Eyre, G. A. Kelly, A. P. McNally, E. Andersson, and A. Persson. Assimilation of TOVS radiance information through one-dimensional variational analysis. *Quarterly Journal of the Royal Meteorological Society*, 119(514):1427–1463, October 1993.

[52] Jouni Pulliainen. Mapping of snow water equivalent and snow depth in boreal and sub-arctic zones by assimilating space-borne microwave radiometer data and ground-based observations. *Remote Sensing of Environment*, 101(2):257–269, 2006.

[53] Michael Durand, Edward J. Kim, and Steven A. Margulis. Radiance assimilation shows promise for snowpack characterization. *Geophysical Research Letters*, 36(2):1–5, 2009.

[54] Yonghwan Kwon, Zong-Liang Yang, Long Zhao, Timothy J. Hoar, Ally M. Toure, and Matthew Rodell. Estimating Snow Water Storage in North America Using CLM4, DART, and Snow Radiance Data Assimilation. *Journal of Hydrometeorology*, 17(11):2853–2874, 2016.

[55] Michael Durand, Edward J. Kim, Steven A. Margulis, and Noah P. Molotch. A first-order characterization of errors from neglecting stratigraphy in forward and inverse passive microwave modeling of snow. *IEEE Geoscience and Remote Sensing Letters*, 8(4):730–734, 2011.

[56] C. Mätzler. Passive microwave signatures of landscapes in winter. *Meteorology and Atmospheric Physics*, 54(1-4):241–260, 1994.

[57] Michael Durand, Edward J. Kim, and Steven A. Margulis. Quantifying uncertainty in modeling snow microwave radiance for a mountain snowpack at the point-scale, including stratigraphic effects. *IEEE Transactions on Geoscience and Remote Sensing*, 46(6):1753–1767, 2008.

[58] J Kukkonen, T Olsson, D M Schultz, A Baklanov, T Klein, A I Miranda, A Monteiro, M Hirtl, and K Eben. and Physics A review of operational , regional-scale , chemical weather forecasting models in Europe. pages 1–87, 2012.

[59] Barton A. Forman, Rolf H. Reichle, and Chris Derksen. Estimating Passive Microwave Brightness Temperature over Snow- covered Land in North America Using the GEOS-5 Catchment Land Surface Model and an Artificial Neural

Network. *IEEE Transactions on Geoscience and Remote Sensing*, pages 1–2, 2013.

[60] Barton A Forman and Rolf H Reichle. Using a support vector machine and a land surface model to estimate large-scale passive microwave temperatures over snow-covered land in North America. *IEEE Journal of Selected Topics in Applied Earth Observations and Remote Sensing*, 2014.

[61] Yuan Xue and Barton A. Forman. Comparison of passive microwave brightness temperature prediction sensitivities over snow-covered land in North America using machine learning algorithms and the Advanced Microwave Scanning Radiometer. *Remote Sensing of Environment*, 170:153–165, 2015.

[62] B A Forman and Y Xue. Machine learning predictions of passive microwave brightness temperature over snow- covered land using the special sensor microwave imager (SSM/I). *Physical Geography*, 2016.

[63] A. L. Samuel. Some Studies in Machine Learning Using the Game of Checkers. *IBM Journal of Research and Development*, 3(3):210–229, 1959.

[64] Trevor Hastie, Robert Tibshirani, Jerome Friedman, and James Franklin. The elements of statistical learning: data mining, inference and prediction, 2005.

[65] Zhibin He, Xiaohu Wen, Hu Liu, and Jun Du. A comparative study of artificial neural network, adaptive neuro fuzzy inference system and support vector machine for forecasting river flow in the semiarid mountain region. *Journal of Hydrology*, 509:379–386, 2014.

[66] J A Suykens, J Vandewalle, and B De Moor. Optimal control by least squares support vector machines. *Neural networks : the official journal of the International Neural Network Society*, 14(1):23–35, 2001.

[67] Alex J. Smola and Bernhard Schölkopf. A tutorial on support vector regression, 2004.

[68] Gerrit Burgers, Peter Jan van Leeuwen, and Geir Evensen. Analysis Scheme in the Ensemble Kalman Filter. *Monthly Weather Review*, 126(6):1719–1724, 1998.

[69] Ivor W Tsang, James T Kwok, and Pak-Ming Cheung. Core vector machines: Fast svm training on very large data sets. *Journal of Machine Learning Research*, 6(Apr):363–392, 2005.

[70] R D Koster, M J Suarez, A Ducharne, M Stieglitz, and P Kumar. A catchment-based approach to modeling land surface processes in a general circulation model 1. Model structure. *Journal of Geophysical Research-Atmospheres*, 105(D20):24809–24822, 2000.

[71] Robert Willis and William W-G Yeh. Groundwater systems planning and management. 1987.

[72] Edward G. Josberger and Nelly M. Mognard. A passive microwave snow depth algorithm with a proxy for snow metamorphism. *Hydrological Processes*, 16(8):1557–1568, 2002.

[73] Alexandre Langlois, Alain Royer, Florent Dupont, Alexandre Roy, Kalifa Goita, and G Picard. Improved corrections of forest effects on passive microwave satellite remote sensing of snow over boreal and subarctic regions. *IEEE Transactions on Geoscience and Remote Sensing*, 49(10 PART 2):3824–3837, 2011.

[74] M. Sturm, J. Holmgren, and G. E. Liston. A seasonal snow cover classification system for local to global applications, 1995.

[75] M. C. Hansen, R. S. DeFries, J. R. G. Townshend, M. Carroll, C. Dimiceli, and R. A. Sohlberg. Global Percent Tree Cover at a Spatial Resolution of 500 Meters: First Results of the MODIS Vegetation Continuous Fields Algorithm, 2003.

[76] K Y Vinnikov, A Robock, S A Qiu, J K Entin, M Owe, B J Choudhury, S E Hollinger, and E G Njoku. Satellite remote sensing of soil moisture in Illinois, United States. *Journal of Geophysical Research-Atmospheres*, 104(D4):4145–4168, 1999.

[77] Lixin Zhang Lixin Zhang, Kaiguang Zhao Kaiguang Zhao, Ying Zhu Ying Zhu, and Bo Qin Bo Qin. Simulated radiation characteristics of frozen soil surface at typical microwave bands. *IGARSS 2004. 2004 IEEE International Geoscience and Remote Sensing Symposium*, 6, 2004.

[78] Jiarui Dong, Jeffrey P. Walker, and Paul R. Houser. Factors affecting remotely sensed snow water equivalent uncertainty. *Remote Sensing of Environment*,

97(1):68–82, July 2005.

[79] JL Foster, DK Hall, ATC Chang, and A Rango. An overview of passive microwave snow research and results. *Reviews of Geophysics*, 22(2):195–208, 1984.

[80] Shunlin Liang, Xiaowen Li, and Jindi Wang. *BOOK: ADVANCED REMOTE SENSING: Terrestrial Information Extraction and Applications*. Elsevier, 2012.

[81] J. I. López-Moreno, J. W Pomeroy, J. Revuelto, and S. M. Vicente-Serrano. Response of snow processes to climate change: spatial variability in a small basin in the Spanish Pyrenees. *Hydrological Processes*, 27(18):2637–2650, August 2013.

[82] Norman Grody. Relationship between snow parameters and microwave satellite measurements: Theory compared with advanced microwave sounding unit observations from 23 to 150 GHz. *Journal of Geophysical Research: Atmospheres*, 113(22), 2008.

[83] R. L. Armstrong and M. J. Brodzik. Recent northern hemisphere snow extent: A comparison of data derived from visible and microwave satellite sensors. *Geophysical Research Letters*, 28(19):3673–3676, October 2001.

[84] Richard P. Lippmann. An introduction to computing with neural nets. *ACM SIGARCH Computer Architecture News*, 16(1):7–25, March 1988.

[85] Chih-Wei Hsu, Chih-Chung Chang, and Chih-Jen Lin. A practical guide to support vector classification. *BJU international*, 101(1):1396–400, 2008.

[86] Agnès Ducharne, Randal D Koster, Max J Suarez, Marc Stieglitz, and Praveen Kumar. A catchment-based approach to modeling land surface processes in a general circulation model: 2. Parameter estimation and model demonstration. *J. Geophys. Res*, 105(24):823–824, 2000.

[87] Marc Stieglitz, Agnès Ducharne, Randy Koster, and Max Suarez. The Impact of Detailed Snow Physics on the Simulation of Snow Cover and Subsurface Thermodynamics at Continental Scales. *Journal of Hydrometeorology*, 2(3):228–242, 2001.

[88] Michele M. Rienecker, Max J. Suarez, Ronald Gelaro, Ricardo Todling, Julio Bacmeister, Emily Liu, Michael G. Bosilovich, Siegfried D. Schubert, Lawrence Takacs, Gi Kong Kim, Stephen Bloom, Junye Chen, Douglas Collins, Austin Conaty, Arlindo Da Silva, Wei Gu, Joanna Joiner, Randal D. Koster, Robert Lucchesi, Andrea Molod, Tommy Owens, Steven Pawson, Philip Pegion, Christopher R. Redder, Rolf Reichle, Franklin R. Robertson, Albert G. Ruddick, Meta Sienkiewicz, and Jack Woollen. MERRA: NASA's modern-era retrospective analysis for research and applications. *Journal of Climate*, 24(14):3624–3648, 2011.

[89] Christian Matzler. Microwave (1-100 GHz) dielectric model of leaves. *IEEE Transactions on Geoscience and Remote Sensing*, 32(4):947–949, 1994.

[90] Marco Tedesco and James R. Wang. Atmospheric correction of AMSR-E brightness temperatures for dry snow cover mapping. *IEEE Geoscience and Remote Sensing Letters*, 3(3):320–324, 2006.

[91] Yubao Qiu, Lingmei Jiang, Jiancheng Shi, and Kebiao Mao. Study of atmospheric effects on AMSR-E microwave brightness temperature over Tibetan Plateau. *International Geoscience and Remote Sensing Symposium (IGARSS)*, pages 1873–1876, 2007.

[92] Yuan Xue and Barton A Forman. Atmospheric and forest decoupling of passive microwave brightness temperature observations over snow-covered terrain in North America. *IEEE Journal of Selected Topics in Applied Earth Observations and Remote Sensing*, Accepted, 2016.

[93] M C Serreze, M P Clark, R L Armstrong, D a McGinnis, and R S Pulwarty. Characteristics of the western United States snowpack from snowpack telemetry(SNOTEL) data. *Water Resources Research*, 35(7):2145–2160, 1999.

[94] Rolf H. Reichle and Randal D. Koster. Assessing the Impact of Horizontal Error Correlations in Background Fields on Soil Moisture Estimation. *Journal of Hydrometeorology*, 4(6):1229–1242, 2003.

[95] Rolf H. Reichle, Sujay V. Kumar, Sarith P. P. Mahanama, Randal D. Koster, and Q. Liu. Assimilation of Satellite-Derived Skin Temperature Observations into Land Surface Models. *Journal of Hydrometeorology*, 11(5):1103–1122, October 2010.

[96] Barton A. Forman. Feasibility of passive microwave brightness temperature assimilation over snow covered land using machine learning. In *72nd Eastern Snow Conference*, 2015.

[97] Barton A. Forman. Sensing and feeling snow from space: A unified radiometric and gravimetric approach. In *73rd Eastern Snow Conference*, 2016.

[98] Peter Ashcroft and Frank J Wentz. AMSR level 2A algorithm. *Algorithm theoretical basis document, Remote Sensing Systems Tech. Rep. 121599B-1*, 2000.

[99] Geir Evensen. The Ensemble Kalman Filter: Theoretical formulation and practical implementation. *Ocean Dynamics*, 53(4):343–367, 2003.

[100] Rasmus Houborg, Matthew Rodell, Bailing Li, Rolf Reichle, and Benjamin F. Zaitchik. Drought indicators based on model-assimilated Gravity Recovery and Climate Experiment (GRACE) terrestrial water storage observations. *Water Resources Research*, 48(7), 2012.

[101] Manuela Girotto, Gabriëlle J. M. De Lannoy, Rolf H. Reichle, and Matthew Rodell. Assimilation of gridded terrestrial water storage observations from GRACE into a Land Surface Model. *Water Resources Research*, pages 1–58, 2016.

[102] Gabriëlle J M De Lannoy and Rolf H Reichle. Global Assimilation of Multi-angle and Multipolarization SMOS Brightness Temperature Observations into

the GEOS-5 Catchment Land Surface Model for Soil Moisture Estimation. *Journal of Hydrometeorology*, pages 669–691, 2016.

[103] Jouni T. Pulliainen and Jochen Grandeil. HUT snow emission model and its applicability to snow water equivalent retrieval. *IEEE Transactions on Geoscience and Remote Sensing*, 37(3 I):1378–1390, 1999.

[104] Bruce Brasnett. A global analysis of snow depth for numerical weather prediction. *Journal of Applied Meteorology*, 38(6):726–740, 1999.

[105] Ross D. Brown and Bruce Brasnett. updated annually. Canadian Meteorological Centre CMC Daily Snow Depth Analysis Data. Environment Canada, 2010. Boulder, Colorado USA: National Snow and Ice Data Center, 2015.

[106] Marco Tedesco, Richard Kelly, James Foster, and A.T.C. Chang. Amsr-e/aqua daily l3 global snow water equivalent ease-grids, version 2. boulder, colorado usa. NASA National Snow and Ice Data Center Distributed Active Archive Center., 2004.

[107] A.T.C. Chang, J. L. Foster, D. K. Hall, B. E. Goodison, a. E. Walker, J. R. Metcalfe, and A. Harby. Snow Parameters Derived from Microwave Measurements During the BOREAS Winter Field Campaign. *Hydrological Processes*, 10:1565–1574, 1997.

[108] Sujay V. Kumar, Rolf H. Reichle, Randal D. Koster, Wade T. Crow, and Christa D. Peters-Lidard. Role of Subsurface Physics in the Assimilation of

Surface Soil Moisture Observations. *Journal of Hydrometeorology*, 10(6):1534–1547, 2009.

[109] Steven Hancock, Robert Baxter, Jonathan Evans, and Brian Huntley. Evaluating global snow water equivalent products for testing land surface models. *Remote Sensing of Environment*, 128:107–117, 2013.

[110] Ross D. Brown, Bruce Brasnett, and David Robinson. Gridded North American monthly snow depth and snow water equivalent for GCM evaluation. *Atmosphere-Ocean*, 41(1):1–14, 2003.

[111] Lauri Kurvonen and Martti Hallikainen. Influence of land-cover category on brightness temperature of snow. *IEEE Transactions on Geoscience and Remote Sensing*, 35(2):367–377, 1997.

[112] J. R. Eyre. Observation bias correction schemes in data assimilation systems: A theoretical study of some of their properties. *Quarterly Journal of the Royal Meteorological Society*, (July):2284–2291, 2016.

[113] Gabriëlle J M De Lannoy, Rolf H Reichle, Paul R Houser, Kristi R Arsenault, Niko E C Verhoest, and Valentijn R N Pauwels. Satellite-Scale Snow Water Equivalent Assimilation into a High-Resolution Land Surface Model. *Journal of Hydrometeorology*, 11(2):352–369, 2009.

[114] Raman K. Mehra. On the Identification of Variances and Adaptive Kalman Filtering. *IEEE Transactions on Automatic Control*, AC-15(2):175–184, 1970.

[115] Rudolph Emil Kalman et al. A new approach to linear filtering and prediction problems. *Journal of basic Engineering*, 82(1):35–45, 1960.

[116] T. Wilheit, A. T C Chang, and A. S. Milman. Atmospheric corrections to passive microwave observations of the ocean. *Boundary-Layer Meteorology*, 18(1):65–77, 1980.

[117] Matthew H. Savoie, Richard L. Armstrong, Mary J. Brodzik, and James R. Wang. Atmospheric corrections for improved satellite passive microwave snow cover retrievals over the Tibet Plateau. *Remote Sensing of Environment*, 113(12):2661–2669, 2009.

[118] Jinjun Tong, Stephen J. Déry, Peter L Jackson, and Chris Derksen. Testing snow water equivalent retrieval algorithms for passive microwave remote sensing in an alpine watershed of western Canada. *Canadian Journal of Remote Sensing*, 36(SUPPL.), 2010.

[119] Chris Derksen. The contribution of AMSR-E 18.7 and 10.7 GHz measurements to improved boreal forest snow water equivalent retrievals. *Remote Sensing of Environment*, 112(5):2701–2710, 2008.

[120] K Goita, A E Walker, and B E Goodison. Algorithm development for the estimation of snow water equivalent in the boreal forest using passive microwave data. *International Journal of Remote Sensing*, 24(5):1097–1102, 2003.

[121] J R Janowicz, D M Gray, and J W Pomeroy. Spatial Variability of Fall Soil Moisture and Spring Snow Water Equivalent Within a Mountainous Sub-Arctic Watershed. *60th Eastern Snow Conference*, pages 127–139, 2003.

[122] Bhaskar J Choudhury and P Pampaloni. *Passive Microwave Remote Sensing of Land–Atmosphere Interactions*. VSP, 1995.

[123] Pratap Singh and Vijay P Singh. *Snow and glacier hydrology*, volume 792367677. Springer Science & Business Media, 2001.

[124] A. Langlois, A. Royer, and K. Goïta. Analysis of simulated and spaceborne passive microwave brightness temperatures using in situ measurements of snow and vegetation properties. *Canadian Journal of Remote Sensing*, 36(SUPPL.), 2010.

[125] Yann H. Kerr and Eni G. Njoku. Semiempirical model for interpreting microwave emission from semiarid land surfaces as seen from space. *IEEE Transactions on Geoscience and Remote Sensing*, 28(3):384–393, 1990.

[126] A E Walker and J I Macpherson. A Canadian Twin Otter Microwave Radiometer Installation for Airborne Remote Sensing of Snow , Ice and Soil Moisture. 00(C):2678–2680, 2002.

[127] C. Derksen, S. L. Smith, M. Sharp, L. Brown, S. Howell, L. Copland, D. R. Mueller, Y. Gauthier, C. G. Fletcher, A. Tivy, M. Bernier, J. Bourgeois, R. Brown, C. R. Burn, C. Duguay, P. Kushner, A. Langlois, A. G. Lewkowicz,

A. Royer, and A. Walker. Variability and change in the Canadian cryosphere. *Climatic Change*, 115(1):59–88, 2012.

[128] Radiometrics Corporation. *Applications of the PR Series Radiometers for Cryospheric and Soil Moisture Research*, 2015.

[129] CM DiMiceli, ML Carroll, RA Sohlberg, C Huang, MC Hansen, and JRG Townshend. Annual global automated modis vegetation continuous fields (mod44b) at 250 m spatial resolution for data years beginning day 65, 2000-2010, collection 5 percent tree cover. *USA: University of Maryland, College Park, MD*, 2011.

[130] Thomas Meissner and Frank Wentz. Intercalibration of amsr-e and windsat brightness temperature measurements over land scenes. In *International Geoscience and Remote Sensing Symposium (IGARSS)*, pages 3218–3219, 2010.

[131] Alexandre Roy, Alain Royer, Jean-Pierre Wigneron, Alexandre Langlois, Jean Bergeron, and Patrick Cliche. A simple parameterization for a boreal forest radiative transfer model at microwave frequencies. *Remote Sensing of Environment*, 124:371–383, September 2012.

[132] Alexandre Roy, Alain Royer, and Ronald J Hall. Relationship between forest microwave transmissivity and structural parameters for the canadian boreal forest. *IEEE Geoscience and Remote Sensing Letters*, 11(10):1802–1806, 2014.

[133] N. Kruopis, J. Praks, A. Nadir Arslan, H.M. Alasalmi, J.T. Koskinen, and M.T. Hallikainen. Passive microwave measurements of snow-covered forest

areas in EMAC'95. *IEEE Transactions on Geoscience and Remote Sensing*, 37(6):2699–2705, 1999.

[134] Hua Yuan, Yongjiu Dai, Zhiqiang Xiao, Duoying Ji, and Wei Shangguan. Reprocessing the MODIS Leaf Area Index products for land surface and climate modeling. *Remote Sensing of Environment*, 115(5):1171 – 1187, 2011.

[135] Peter N. Beets, Stephen Reutebuch, Mark O. Kimberley, Graeme R. Oliver, Stephen H. Pearce, and Robert J. McGaughey. Leaf Area Index, Biomass Carbon and Growth Rate of Radiata Pine Genetic Types and Relationships with LiDAR. *Forests*, 2(4):637–659, August 2011.

[136] Jinjun Tong and Isabella Velicogna. A comparison of amsr-e/aqua snow products with in situ observations and modis snow cover products in the mackenzie river basin, canada. *Remote Sensing*, 2(10):2313–2322, 2010.

[137] Jordan S. Borak and Michael F. Jasinski. Effective interpolation of incomplete satellite-derived leaf-area index time series for the continental United States. *Agricultural and Forest Meteorology*, 149(2):320–332, 2009.

[138] Hongliang Fang, Shunlin Liang, John R. Townshend, and Robert E. Dickinson. Spatially and temporally continuous LAI data sets based on an integrated filtering method: Examples from North America. *Remote Sensing of Environment*, 112(1):75–93, 2008.

[139] Leila Farhadi, Rolf H. Reichle, Gabriëlle J. M. De Lannoy, and John S. Kimball. Assimilation of FreezeThaw Observations into the NASA Catchment Land Surface Model. *Journal of Hydrometeorology*, 16(2):730–743, 2015.

[140] C Matzler and A Standley. Relief effects for passive microwave remote sensing. *International Journal of Remote Sensing*, 21(12):2403–2412, 2000.

[141] J. L. Foster, A. T C Chang, and D. K. Hall. Comparison of snow mass estimates from a prototype passive microwave snow algorithm, a revised algorithm and a snow depth climatology. *Remote Sensing of Environment*, 62(2):132–142, 1997.

[142] Helmut Rott and Josef Aschbacher. On the use of satellite microwave radiometers for large-scale hydrology. *IAHS-AISH publication*, (186):21–30, 1989.

[143] James R. Wang and Will Manning. Near concurrent MIR, SSM/T-2, and SSM/I observations over snow-covered surfaces. *Remote Sensing of Environment*, 84(3):457–470, 2003.

[144] M.A Friedl, D.K McIver, J.C.F Hodges, X.Y Zhang, D Muchoney, A.H Strahler, C.E Woodcock, S Gopal, A Schneider, A Cooper, A Baccini, F Gao, and C Schaaf. Global land cover mapping from MODIS: algorithms and early results. *Remote Sensing of Environment*, 83(1-2):287–302, 2002.

[145] Hongliang Fang, Wenjuan Li, and Ranga B. Myneni. The impact of potential land cover misclassification on MODIS leaf area index (LAI) estimation: A statistical perspective. *Remote Sensing*, 5(2):810–829, 2013.

[146] Hamlyn G Jones and Robin A Vaughan. *Remote sensing of vegetation: principles, techniques, and applications*. Oxford university press, 2010.

[147] Benjamin J. Vander Jagt, Michael T. Durand, Steven A. Margulis, Edward J. Kim, and Noah P. Molotch. On the characterization of vegetation transmissivity using LAI for application in passive microwave remote sensing of snowpack. *Remote Sensing of Environment*, 156:310–321, 2015.

[148] Qinghuan Li and Richard Kelly. *Exploring the use of MODIS vegetation transmissivity for correcting passive microwave observation of snow-covered terrain / landscape* . PhD thesis, 2014.

[149] Yonghwan Kwon, Zong-Liang Yang, Timothy J. Hoar, and Ally M. Toure. Improving the radiance assimilation performance in estimating snow water storage across snow and land-cover types in north america. *Journal of Hydrometeorology*, 18(3):651–668, 2017.

[150] Ross D Brown and Dominique Tapsoba. Improved Mapping of Snow Water Equivalent over Quebec. pages 3–7, 2007.

[151] Rolf H. Reichle. Data assimilation methods in the Earth sciences. *Advances in Water Resources*, 31(11):1411–1418, November 2008.

[152] Li Li, Eni G. Njoku, Eastwood Im, Paul S. Chang, and Karen St Germain. A Preliminary Survey of Radio-Frequency Interference Over the U.S. in Aqua AMSR-E Data, 2004.

[153] K Levenberg and K Levenberg. A Method for the Solution of Certain Problems in Least Squares. In *Quart. Appl. Math.*, volume 2, pages 164—-168, 1944.

[154] Donald W. Marquardt. An Algorithm for Least-Squares Estimation of Nonlinear Parameters, 1963.

[155] R Rojas. *Neural networks: a systematic introduction*. 1996.

[156] C M Bishop. *Neural Networks for Pattern Recognition*, volume 92. 1995.

[157] Jason Weston. Support Vector Machine Tutorial. August 2011.

[158] Chih-Chung Chang and Chih-Jen Lin. LIBSVM: A Library for Support Vector Machines. *ACM Transactions on Intelligent Systems and Technology*, 2:27:1—-27:27, 2011.

[159] Artemio Sotomayor-olmedo, Marco a Aceves-fernández, Efrén Gorrostieta-hurtado, Carlos Pedraza-ortega, Juan M Ramos-arreguín, and J Emilio Vargas-soto. Forecast Urban Air Pollution in Mexico City by Using Support Vector Machines : A Kernel Performance Approach. 2013(July):126–135, 2013.

[160] Bilal M Ayyub and Richard H McCuen. *Probability, statistics, and reliability for engineers and scientists*. CRC press, 2011.

[161] Dara Entekhabi, Rolf H. Reichle, Randal D. Koster, and Wade T. Crow. Performance Metrics for Soil Moisture Retrievals and Application Requirements. *Journal of Hydrometeorology*, 11(3):832–840, 2010.

[162] Yonghong Yi, John S. Kimball, Lucas A. Jones, Rolf H. Reichle, and Kyle C. Mcdonald. Evaluation of MERRA land surface estimates in preparation for the soil moisture active passive mission. *Journal of Climate*, 24(15):3797–3816, 2011.